A doctoral dissertation

Studies on changes in surface/bulk structure and photocatalytic activity of titania powders induced by braying

Guangyi Chen

Division of Environmental Material Science
Graduate School of Environmental Science
Hokkaido University

2021

Table of Contents

Chapter 1

General Introduction

1.1 Identification of materials

In the field of organics, identification of a material is defined by the Journal of Organic Chemistry, requesting to show, at least, elemental analysis data within 0.3% error and NMR pattern [1]. So, in the case of molecular or metal complex, identification is defined by molecular structure. In other words, identification is to be named reflecting its structure. Then, how about inorganic compound, like metal oxide?

For solid materials, characterization of their structures is not straightforward compared with that for molecules. Both bulk and surface structures should be characterized. IUPAC recommendation on inorganic compounds says "... in cases where detailed structural information is to be conveyed, fully systematic names can be difficult to construct." [2], which means they've given up identification for inorganic compounds. The one of the reasons for the difficulty are existence of surface in those solid materials. We have no systematic nomenclature method for solid surfaces except for single crystals exposing only one type of a facet. Moreover, solids are sometimes not crystalline, that is, amorphous part may be included.

1.2 Amorphous Metal Oxide

1.2.1 Application of Amorphous Metal Oxide

Owing to our continuously growing energy consumption, solar energy harvesting and solar fuels such as hydrogen from water as a form of sustainable energy are gaining enormous interests. Researchers turn to develop potential functional materials aiming to address the current energy crisis. One of the ideal candidates is the amorphous metal oxide which is ubiquitous and critical for modern and emerging semiconductor devices. For instance, a pinhole-free amorphous aluminum doped with zinc oxide was applied to protection layer, which could enhance the chemical stability of silver nanowire as bottom electrodes, of flexible perovskite solar cells (PVSCs). [3] Moreover, amorphous metal oxide semiconductors (MOS) for thin-film transistors (TFTs) applications is striking and promising as well. For example, amorphous In_2O_3 films were achieved by doping with an insulating polymer [poly(4-vinylphenol) (PVP)] affording high-performance, transparent, and ultra-flexible TFTs at processing temperatures as low as 225 °C. [4] However, when it comes to tremendously wide range utilization of amorphous or defective metal oxide

materials, TiO_2 will be unavoidably mentioned including photocatalysts for self-cleaning glass and water splitting [5,6], dye-sensitized solar cells (DSSCs) for solar energy utilization [7], Li-ion battery materials for energy storage [8-10] and resistive switching memories for low power and non-volatile data storage. [11,12] The key to the performance of these varied applications is the transport of electrons which may be introduced by optical excitation, electrical injection or doping. For example, a hydrogenated black titania possessing narrow bandgap (approximate 1.5 eV) was reported that not only is able to response for the full spectrum sunlight but photocatalytic performance is enhanced tremendously. [13] The structure and chemical composition of black TiO_2 is significantly changed comparing with the original white TiO_2, with some modifications like surface disordered shell, oxygen vacancy/self-doped Ti^{3+} or incorporation of H-doping. Theoretical study reported an enhancement in the efficiency of photocatalytic activity on defective surfaces compared to stoichiometric surfaces. This breaking-through discovery furtherly triggered defect engineering optimizing and development of titania or TiO_2-based composite materials, which aimed at manipulating the nature and the concentration of defects in different type of titania so as to tune their properties in a desired manner or to generate highly efficiency photocatalytic activity and function-orientated characteristics.

1.2.2 Preparation of Amorphous Metal Oxide

1.2.2.1 Mechanical Milling

It is believed that the active or high-performance materials, such as, amorphous or defect titania, are correlation with themselves framework which means what bulk/surface structure is could give or enhance their certain property. Generally, their preparation process or synthesized precursors could be important or crucial for material intrinsic property. There were several plausible methods to prepare or synthesize amorphous or defects metal oxide. Milling of crystal or stoichiometric metal oxide where preparation homogeneous material is not mainly purpose has been termed as mechanical milling. Usually, mechanical milling process where the long-range order crystal will be undermined to produce either distorted or amorphous phase material has been defined as mechanical disordering. [14] Moreover, a solids state process referring to mechanically activated annealing process (M2AP) where initially candidate samples initially experienced a short-time mechanical milling by ball milling then were calcined in relatively low temperature (below 800 °C), was benefited for preparation of refractory materials i.e., silicide [15] or take away contaminations from as-prepared products. It is worthy to mention that there are considerable different types of defects formation in those as-prepared samples, such as anti-site chemical disorder [16] or increased grain boundary during mechanical milling. [17] In addition, a recent investigation showed that ball milling nanosized anatase powders with 2% TiH_2 for 15 min could evidently enhance photocatalytic H_2 evolution activity of TiO_2 anatase nanoparticles but extending ball mill period could lead to considerable amorphization. [18]

1.2.2.2 Electrochemical Anodization

Electrochemical anodization is treated as quite prevail method to synthesize amorphous titania nanotube (NTs) arrays used as electrode. [19-23] The advantages of electrochemical anodization might be attributed to quite convenient application and control of the morphology of nanostructure while ensuring that the coating is directly on the relative material surface. [24] The formation of nanotube arrays follows three simultaneous processes: (a) the electrochemical oxidation of Ti metal to generate TiO_2, (b) the electric field assisted dissolution of Ti metal ions in the electrolyte, and (c) the chemical dissolution of TiO_2 owing to etching. [25] However, there are many factors—including type of adopted electrolytes or synthesis temperature—could influence nanotube morphology and oriented growth. Normally, as-anodized amorphous TiO_2 NTs need to anneal above 450 °C to crystallite before being utilized. However, a facile and environmentally friendly strategy rely on electrochemical anodization, as depicted as inset of **Figure 1-1**, to synthesize crystallized amorphous titania NTs subsequently immersing into 92 °C hot water simply it possesses high photocatalytic activity. [26] Moreover, fluoride-containing electrolytes are toxic and generally cause safety issues. Hence based on precondition without involving hazardous chemicals, a fluoride-free electrolyte was applied in the process of synthesizing NTs in which NTs was grown in a safer manner. [27] Generally speaking, electrochemical anodization is promising way of amorphous electrode materials synthesized.

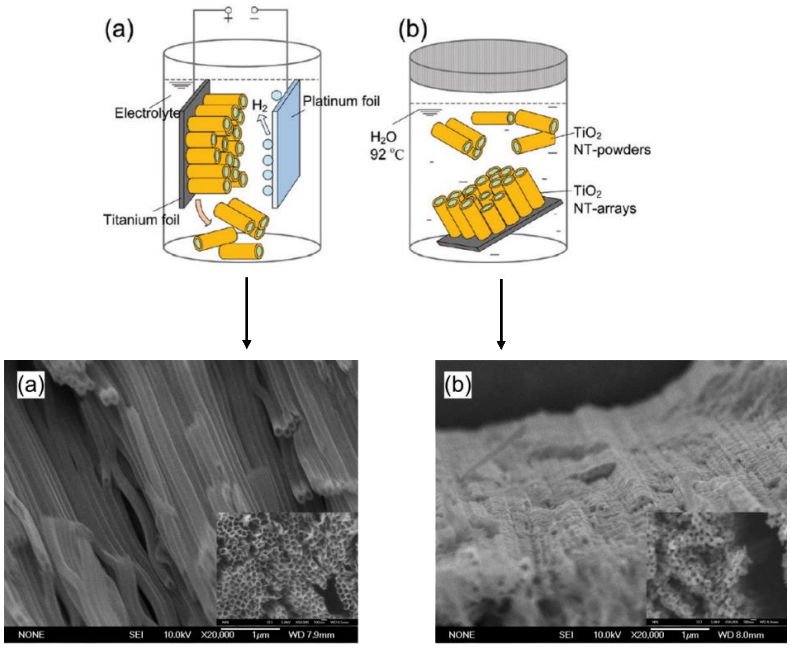

Figure 1-1 Schematic diagram of the anodization process of Ti sheet into NT-arrays or NT-powders and morphology of TiO_2 nanotube. [26]

1.2.2.3 Atomic Layer Deposition (ALD)

With oxide semiconductor thin-film transistors (TFTs) are becoming the mainstream backplane technology in the display industry because of their attractive advantages over silicon-based TFTs, including good device performance, optical transparency, low process temperature, and low-cost fabrication process. [28] Atomic layer deposition (ALD) could meet such an application to fabricate high-quality dielectric and luminescent films on large-area substrate. As special modification of chemical vapor deposition the growth of material layers by ALD consists of repeating the following characteristic four steps (one ALD cycle shown in **Figure 1-2**) : (1) A self-terminating reaction of the first reactant (Reactant A); (2) A purge or evacuation to remove the nonreacted reactants and the gaseous reaction by-products.; (3) A self-terminating reaction of the second reactant (Reactant B) —or another treatment to activate the surface again for the reaction of the first reactant; (4) A purge or evacuation. [28] The growth cycles are repeated as many times as required for desired film thickness. [29] With a benefited supplementary coming from development of ALD technology, amorphous TiO_2 film and TiO_2-based derives become thriving and prosperous especially in the field of photocatalysis and electrochemistry. Recently, such a method was used to deposit nearly amorphous TiO_2 films on the surface of graphene (reduced graphene oxide) sheets which precoated with Al_2O_3 layer. [30] This amorphous titania ALD film on graphene as an anode in Li-ion batteries exhibited stable capacity and excellent cycling stability due to nanoscale TiO_2 coatings minimized the effect of the low diffusion coefficient of lithium ions in bulk TiO_2. [31] In addition, ALD method also could be applied to produce 2D TiO_2 materials, such as nanosheets. It is reported that through adjusting ALD cycles to obtain different thickness layer amorphous 2D titania nanosheets featured as superficial Ti^{3+} defects and effectively increased the degradation rates of methyl orange solution [32].

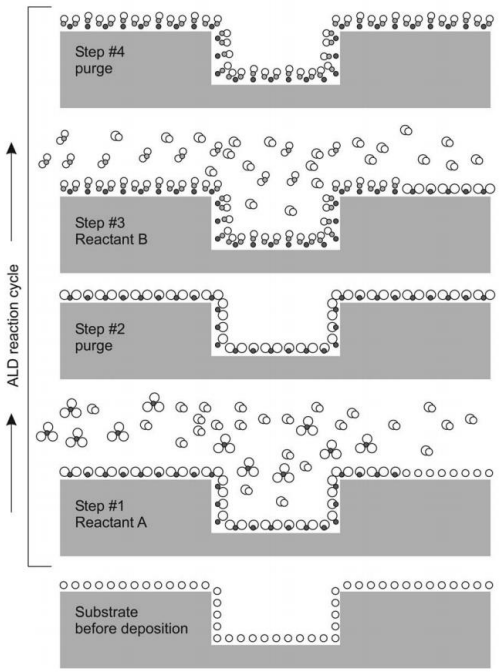

Figure 1-2 Schematic illustration of one ALD reaction cycle. [28]

1.2.2.4 Other Methods

At last but not least, thanks to domino effect brought by black titania different kinds of titania material predominantly containing point defect were manipulated and exhibited their extraordinary utilization. Generally according to precursor variation, different kinds of defect TiO_2 are able to be synthesized by reduction approach relying on reductant, such as H_2, Al [33], Mg [34, 35] and so forth, while using white and crystal titania as precursor. For instance, researchers found that high-active defective titania were able to form by hydrogenated commercial P25 and the samples color changed from white to dark with hydrogenation time prolonging. [36] That dark color samples for 20-day hydrogenation possess narrowest band gap, ca.1.82 eV, and highest hydrogen evolution rate, 3.94 mmol g^{-1} h^{-1} in visible light irradiation. [36] Furthermore, annealing TiO_2 in inert gas atmosphere, N_2 or Ar_2, at high temperature also could produce defect titania as reported by some literatures. [37, 38] Moreover, if applying low-valance-state Ti species as precursor—such as TiO [39], TiH_2, $TiCl_3$ [40], etc.—and leaning upon oxidants, the defect-rich titania could be obtain as well. For example, TiH_2 used as precursor reacted with 30% H_2O_2 aqueous solution then annealed in argon under 630 °C, which created visible-region active black titania with masses of Ti^{3+} centers. [41] In addition, using amorphous titania as precursor also were able to synthesize defective titania samples that an amorphous sol treated with 0.3 wt.% H_2O_2 has higher degradation rate for methylene blue (MB) in both visible light and UV irradiation than counterpart P25. [42] And it is reported that a porous amorphous titania mixed together with imidazole and hydrochloric acid and calcined at 450 °C in air for 6 hours, leading to as-prepared defective sample not only was very stable but also exhibited superior water splitting performance, 115 μmol h^{-1} g^{-1} of H_2 evolution rate [43].

1.3 *Functionality of Defects in Titania and Titania-based Materials*

Defects which exist widely in titania or titania-based material have great impact on the properties of titania, including its light absorption, charge transport and surface adsorption which in turn plays a significant role in the photocatalytic activity of titania. On one hand, defects in titania materials can limit the transport (mobility and diffusion lengths) of charge carriers, while on the other hand they are important for tuning the carrier concentrations and Fermi level for realizing p-type (hole conducting) and n-type (electron conducting) materials. [44] There are two kind of common defects, oxygen vacancy (O_v) and titanium interstitial (Ti_{int}) in reduced titania, which have been investigated and studied tremendously. Moreover, no matter for O_v or T_{int} are accompanied by the appearance of Ti^{3+} species which play an important role in the optical and chemical activity of titania material. [45]

1.3.1 Oxygen Vacancy

Normally, oxygen vacancy was formed by removing one of neutral oxygen atoms from the lattice, leading to excess electrons filling into the empty state of the Ti ions then forming Ti^{3+} species. [46] For example, although Cu_2O is promising candidate for hydrogen evolution in visible region, characteristic as susceptible oxidation tends to hinder its application. However, its titania composited material—Cu_2O adjoined with octahedral oxygen-vacancy defect TiO_2 heterostructure—are able to both stabilize Cu_2O and boost up its photocatalytic activity of solar water splitting. [47] Based on DOS calculation results, the conduction band edge is composed by Ti 3d states and several new band-gap states formed in this material which could attribute to oxygen vacancy appearing. These band-gap states could trap electrons in titania then spontaneously inject electrons into Cu 3d orbitals due to interfacial charge transfer, leading to prominent photocatalytic performance of Cu_2O/TiO_2 hetero-material. Moreover, oxygen vacancy (O_v) can behave as active site in the photocatalytic reduction of CO_2. It is mentioned in research of Ji et al. that the reason why the fast-hydrogenation pathway preferentially occurred in defect surface (contained oxygen vacancy) is due to tremendously decreasing the hydrogenation barrier of CH_2O to CH_3O at the O_v than of the perfect surface for CO_2 photoreduction. [48]

1.3.2 Interstitial Ti

In addition to O vacancies, Ti interstitials also be considered as defect sites that may influence and even dictate the surface chemistry of titania. They formed in reduced titania surface or bulk which were treated by both ions sputtering and high temperature annealing. [49] About the origin of gap states is under debate, unlike oxygen vacancy were treated as origin of gap states in long time, Ti interstitial takes a long time to persuade researchers to believe it takes a responsibility for gap-state appearing as well. Initially, Henderson considered that Ti_{int} could diffuse on the rutile $TiO_2(110)$ surface under UHV conditions. [50] Afterwards, through applying STM technology and photoelectron spectroscopy measurement in conjunct with DFT calculations, Wendt et al. finally concluded that the gap

state originates mainly from Ti interstitials defects in the near-surface region of as-treated TiO_2(110) sample where bridging oxygen vacancy were replaced by bridging OH groups in reaction with O_2. [51,52] Meanwhile, it is reported that interstitial Ti atoms are participated in the reconstruction of TiO_2(110) under annealing in air atmosphere. [53] Moreover, based on theoretical analysis of DTF calculation Morita et al. pointed that with the exception that partial excess electrons still remained in Ti_{int} most excess electrons introduced by Ti_{int} behave in a similar manner to those introduced by V_O, which suggests that Ti_{int} also contributes to the surface chemical reactions of TiO_2(110). [54] In fact, titanium interstitial either diffusion into bulk or diffusion towards surface in reduced TiO_2 crystal in thermal treatment at different atmosphere. [51] In other words, this kind of defect not only will exist in bulk but in the surface.

1.3.3 Grain Boundary

Except for above mentioned two kinds of defect, another one is grain boundary defects who is interface transition area between grains with same structure but different orientation where atomic arrangement from a kind of orientation gradually change into another one. The local structure or property of grain boundary, nevertheless, is complicated. Grain boundary defect is not merely involved point defects category but also contain two dimensional defects, stacking or mismatching and so on. [55] As reported by Bryan et al., they found TM^{n+} colloid which is TiO_2 doped with Co^{2+} and Cr^{3+}, respectively, from paramagnetic colloid transforms into ferromagnetic film after dealing with spin-coated in air atmosphere. [56] Subsequent results and analysis reveal that this kind of triggering ferromagnetism in crystalline film ascribe to the creation of grain boundary defects which assumed as oxygen vacancy at fusion interfaces. [56] Meanwhile the ferromagnetism of TM^{n+} film was destroyed by post-annealing in air. Furthermore, the DTF calculation pointed that the deep traps in grain boundary of rutile TiO_2 which control the electron mobility are associated with high electrostatic potential since grain boundary possesses strong affinity for electrons in other words electrons will be trapped and their mobility will be hindered as well. [57]

1.4 Characterization for Amorphous/Defective Titania Materials

The presence of amorphous oxides that characterization is difficult owing to underdeveloped probing technique, is usually considered to have no influence on the final sample properties. This simplification, it is acceptable when the amount of non-crystalline components is low, are not able to applicable if their amount becomes important, as is the case when preparing very small nanoparticles of crystalline oxide. [46] Moreover, defect or amorphous titania is gradually applied in different field, such as photocatalysis. Therefore, characterizing defect or amorphous titania is becoming more and more important.

1.4.1 X-ray Diffraction Spectroscopy Analysis

X-ray diffraction spectroscopy is often used to analyze solid materials properties, such as phase structure. Solid materials could be consisted by crystal and amorphous. The crystal part has a long-range order of arrangement of atoms, ions, or molecules and the amorphous part has only a short-range order. [58] Identification of crystal phase is achieved by comparing the XRD patterns obtained from unknown samples with the known standard reference. But XRD pattern cannot give any information on whether an amorphous part is included or not. [58] However, with Rietveld method putting forward, quantitative analyses amorphous phase could be realized due to an internal standard method based on Rietveld-XRD whole-pattern fitting analysis. For example, in previous study of our lab nickel(II) oxide were selected as internal standard and finally the crystal composition of P25 titania were obtained as well in which anatase-rutile-amorphous ratio is determined to be 78:14:8. [59] The limit of conventional X-ray powder diffraction for the detection of supported nanoparticles is usually 2–2.5 nm, at which size low signal to noise ratios make detection difficult in particular particles of low weight loading and small particle size. [60] The crystallite size and lattice strain of candidate material also could be estimated by XRD diffraction analysis. Normally Scherrer formula is prevalent application but only considered the effect of crystallite size on the XRD peak broadening, moreover it seems not offering information about microstructures of the lattice, such as the intrinsic strain which might derive from point defect, grain boundary, triple junction and stacking faults. [61] One of method is Halder-Wagner method [62] exhibited by

$$\left(\frac{\beta_{tot}\cos\theta}{\sin\theta}\right)^2 = \frac{K\lambda}{D_{HW}} \cdot \frac{\beta_{tot}\cos\theta}{sin^2\theta} + 16\varepsilon_{HW}^2 \quad \textbf{(1-1)}$$

Where D_{HW} and ε_{HW} are Halder-Wagner crystallite size and strain, respectively. Here, when a plot of $\left(\frac{\beta_{tot}\cos\theta}{\sin\theta}\right)^2$ is made against $\frac{\beta_{tot}\cos\theta}{sin^2\theta}$ then a straight line graph of slope $\frac{K\lambda}{D_{HW}}$ and intercept $16\varepsilon_{HW}^2$ is obtained. Here, the slopes yield the Halder-Wagner crystallite size, D_{HW}, while the intercept gives the Halder-Wagner strain, ε_{WH}.

1.4.2 TEM and HRTEM Analysis

The transmission electron microscope (TEM) is used for identification and characterization of the finely grained crystal and amorphous inorganic materials. This technique conducts investigations at very high magnification scale which is up to hundreds of thousand times and limits of resolution about 0.1~0.3 nm. [63] Therefore, nanostructure refers to size, orientation and organization of crystal or amorphous titania could be characterized and identification.

The high-resolution transmission electron microscopy (HR-TEM) is an effective approach for directly observing crystal lattice in an atomic-scale with simple sampling preparation for nanoparticles. [64] Tian et al. found that annealing amorphous ultrafine nanoparticles (UNP) in argon atmosphere for 2 hours at ca.970 K leading to those particles possess core-shell structure according to their HRTEM picture. [65]

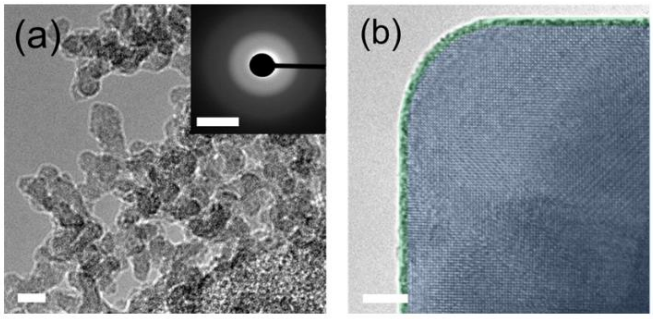

Figure 1-3 (a) HRTEM image of UNP aggregates are amorphous. (b) HRTEM image of a crystalline particle with crystal core (blue) and a disordered shell (green line). [65]

1.4.3 STM and AFM Analysis

The scanning tunneling microscope (STM) yields surface topographies on an atomic scale directly in real space. [66] A conducting sample and a sharp metal tip, which acts as a local probe, were brought within a distance of a few angstroms, resulting in a significant overlap of the electronic wavefunctions. With an applied bias voltage (typically between 1 mV and 4 V), a tunneling current (typically between 0.1 nA and 10 nA) can flow from the occupied electronic states near the Fermi level of one electrode into the unoccupied states of the other electrode. By using a piezoelectric drive system for the tip and a feedback loop, a map of the surface topography can be obtained. [67, 68] With supported by STM technique Wendt et al. found oxygen vacancy is not the only defect state which could induce gap state and claimed titanium interstitial defect also could. [51] However, as reported by some researchers, the tip of STM can provide electric fields and/or currents, which are high enough to induce lateral or vertical motion of the defects. [69, 70] For instance, oxygen vacancies vertical motion on anatase TiO_2(101) surface were able to trigger by STM tip with high-bias condition. As it shown in **Figure 1-4(a)**, the STM image of a clean anatase (101) surface was taken with standard (low-bias) conditions. Brighter regions correspond to positions of subsurface donors, likely extrinsic dopants. Subsequently with bias increased by +5.2 V horizontal streaks appeared indicating samples surface structure changed a lot then the same area is imaged again in **Figure 1-4(c)** with normal imaging conditions but several new features could be observed in this area; some are marked by arrows. These new appearing light spots are oxygen vacancy defects. After repeating above manipulation 32 times which means increasing tip bias first then deceasing it later to scan samples surface, there are so many light spots showing in **Figure 1-4(d)** [71].

Another surface scanning probe microscope is the atomic force microscopy (AFM), which equip with a fine probe to prove over a surface rather than use electrons or a beam of light [72]. AFM has developed into a powerful characterization tool for exploring surface properties at the atomic scale and even could study surface atom/molecular reactions. The mechanism of the AFM is based on the detection of forces acting between a sharp probe and the surface of the sample [73]. The probe is known as the AFM tip or the AFM sensor,

which is attached to a very flexible cantilever [74]. For instance, as it exhibited in below **Figure 1-5**, relying on AFM measurement researchers observed that neutral O_2 molecules can diffuse across the surface at temperature above ca. 25K and are attracted to the $(O_2)^-$ in anatase TiO_2 (101). According to chemical forces different measured by AFM they can distinguish charged $(O_2)^-$ and neutral O_2 [75].

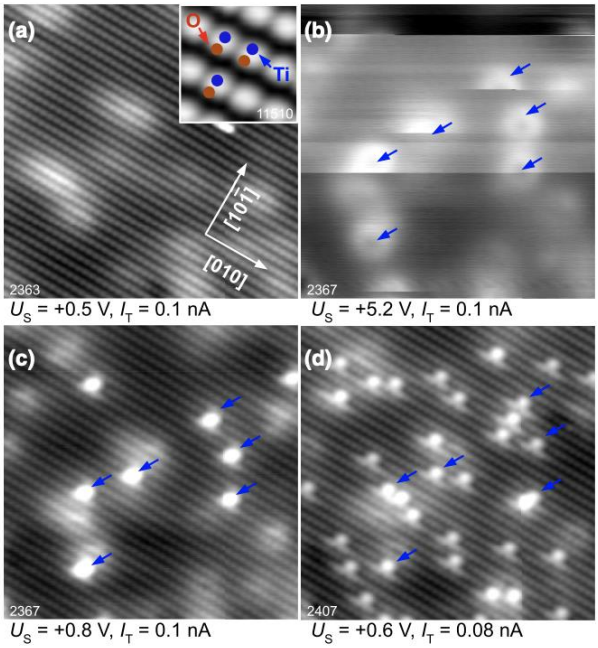

Figure 1-4 STM image of anatase-(101) surface[69].

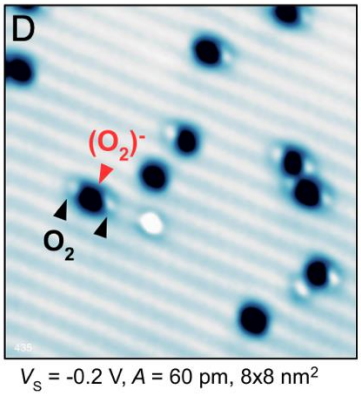

Figure 1-5 AFM image of neutral O_2 diffused toward the $(O_2)^-$[73].

1.4.4 XPS and EPR

The X-ray photoelectron spectroscopy (XPS) is a prevalent tool to check surface of candidate sample with approximately 10 nm probing depth under sample surface [76]. As reported in majority literatures [77-79], bare TiO_2 specimen exhibits two characteristic XPS peaks in around 458 eV and 464 eV which are assigned to Ti^{4+} $2p_{3/2}$ and $2p_{1/2}$, respectively.

Amorphous or defect titania might contain Ti^{3+} species hence either additional peaks will appear in lower binding energy side or the original peak will shift toward low-energy side [80].

Electron paramagnetic resonance (EPR) is a technique for studying unpaired electrons in materials. It deals with the interaction between electromagnetic radiation and magnetic moments which arise from electrons rather than nuclei. Each electron possesses an intrinsic magnetic-dipole moment that arises from its spin and in most systems, electrons occur in pairs such that the net moment is zero [81]. Hence only species that contain one or more unpaired electron possess the net spin moment necessary for suitable interaction with an electromagnetic field. For example, bare titania is silent for EPR. However, defect titania, such as black titania, possess unpairs electrons which could be trapped at Ti $3d^1$ state (Ti^{3+} center) or at the oxygen vacancy (F^+ center), and produce EPR response (characteristic g-value) [82]. Normally, bulk Ti^{3+} center gives a g-value around 1.94 [83] and F^+ center gives a g-value of ca. 2.001~2.005[84] and the surface Ti^{3+} center tend to adsorb atmospheric O_2 to produce O_2^-, which shows EPR signals at g-value approaching 2.02[85].

1.5 Reserved Double-Beam Photoacoustic Spectroscopy (RDB-PAS)

1.5.1 Principle of PAS

Photoacoustic effect was discovered by Bell, who is inventor of the telephone; a sound wave is generated from a sample when intermittent sunlight is irradiated on optically absorbing materials in 1880 [86]. Since then, the photoacoustic theory was revealed and the applications of photoacoustic sensing techniques increase gradually. As a technique for trace-gas detection, photoacoustic spectroscopy (PAS) was applied prevalently due to its high sensitivity. The basic theory of this technique is that a certain wavelength modulated light is absorbed by the gas sample, the electrons in this sample is excited and relaxed to the ground state through emission of photons or heat (non-radiative process), leading to localized heating in the gas sample that results in local pressure periodic change. When sound wave in the same frequency is produced, the PAS signal could be collected by a microphone. [87] Photoacoustic (PA) detection is more sensitive than conventional optical methods, and even small absorption such as small number of defects can be detected. [88]

Since oxygen anions of metal oxides are easily detached. leaving electrons in an oxygen defect, almost all the metal oxides are classified as n-type semiconductors which have electron-filled donor levels below CBB. [89] Meanwhile, about the origin of observed electronic states is under discussion, but it might be correlated with formation of Ti^{3+} center, which is electron-filled electron trap (ET). In other words, low-coordinated Ti cations at surfaces introduce unoccupied Ti 3d states that can trap electrons, reducing charge mobility. Self-trapping process occurs in surfaces-defects or interfaces, and even might be within the bulk material due to the charge carriers tend to localize on these sites. That might affect electron mobility throughout TiO_2, which greatly influences its performance as an electron transport material for energy applications. [90] Shallow ETs are located close to the

conduction band edge and electrons in this ETs could excite to conduction band by room temperature, while deeper ETs in the band gap promote carrier recombination. [91-92]

Recently developed a novel technique, reversed double-beam photoacoustic spectroscopy (RDB-PAS) [93-95], enabling acquisition of patterns of energy-resolved distribution of electron traps (ERDT)/conduction-band bottom (CBB) for semiconducting metal oxides and carbonitrides (C_3N_4) [96], which have ETs as electron-accepting vacant electronic states.

1.5.2 RDB-PAS measurement

Figure 1-6 exhibits the principle of RDB-PAS measurement briefly. In this apparatus, two light beams are combined and introduced to the measurement cell. One is wavelength-scanned continuous monochromatic light to excite electron from valance band (VB) directly to corresponding ETs (simultaneously creating positive holes in VB are captured by an electron donor such as methanol provided in a cell) and the other is a modulated wavelength-fixed light beam to detect trapped electrons in ET forming certain oscillate frequency leading to sound wave signal which could be collected by microphone.

Figure 1-7 illustrates the procedures for measurement [94]. **Figure 1-7**(a) shows a typical raw data of RDB-PA signal for a commercial titania sample, ST-F4, mainly composed of anatase. By scanning excitation pump light wavelength, photoacoustic signal, that corresponds to accumulation of electrons in ETs, is increased gradually. Differentiation from lower energy side gives energy-resolved distribution as a function of energy from VB top (VBT) in relative scale and the density is calibrated using reported total density of titania samples measured by photochemical analysis (**Figure 1-7**(b)). Using the same apparatus, photoacoustic spectrum, corresponding to a diffuse reflectance spectrum, is measured to estimate conduction-band bottom (CBB) energy in reference to VBT.

Figure 1-8 is an ERDT/CBB pattern of ST-F4. The dot line shows the CBB position obtained by ordinal PAS measurement. The number in parentheses shows the total density of ETs (D_{ET}).

Figure 1-9 shows reported ERDT/CBB patterns of commercial titania samples, anatase, A, rutile, R, brookite, B and their mixtures. It shows clearly different patterns with each other. At a glance, without knowing the detailed analysis, it seems that the patterns reflect the bulk crystalline structure, but the pattern shape is not governed by the crystalline structure, as mentioned below.

Figure 1-10 shows a plot of total density of ETs as a function of specific surface area [94]. This indicates that electron traps measured by RDB-PAS are predominantly located on the surface and they are not randomly located surface sites such as point defects, but as a part of surface reconstruction structure. Thus, ERDT patters reflect macroscopic surface structure and total density reflects the surface size like specific surface area.

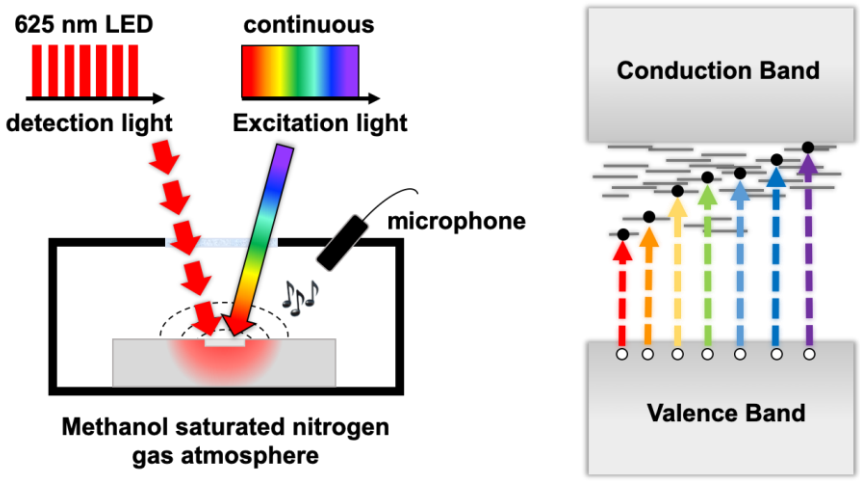

Figure 1-6 Principle of RDB-PAS measurement.

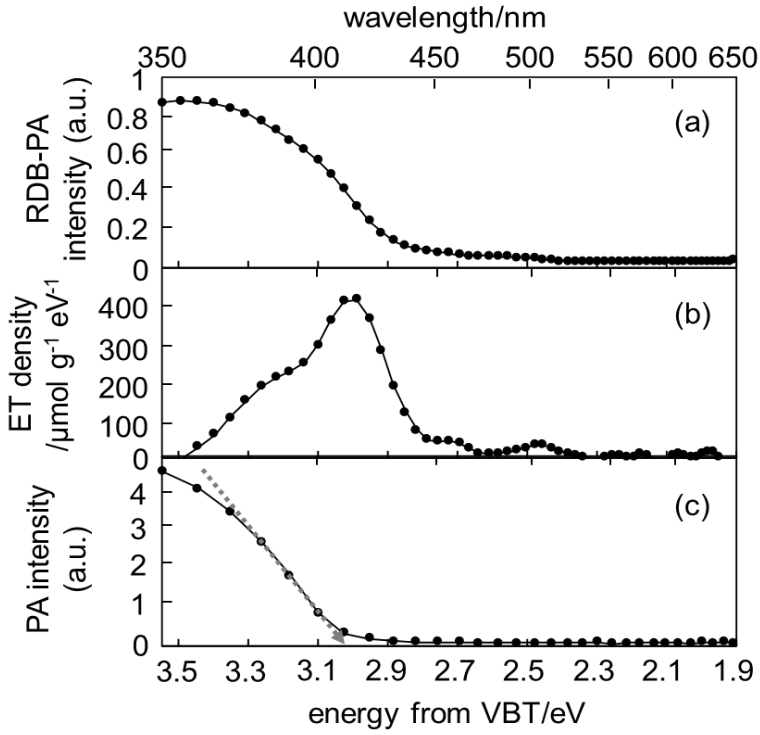

Figure 1-7 (a) RDB-PA spectra, (b) differentiated RDB-PA spectra (ERDT pattern) and (c) PA spectra of commercial titania (ST-F4).

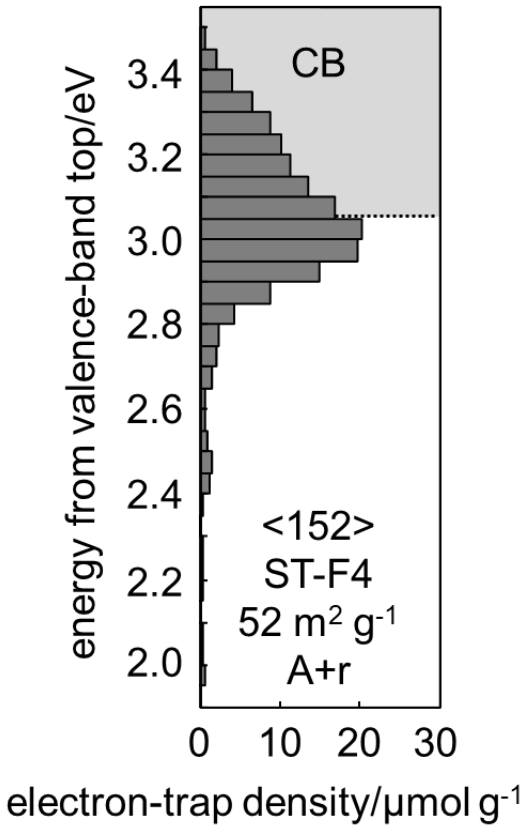

Figure 1-8 ERDT/CBB pattern for ST-F4.

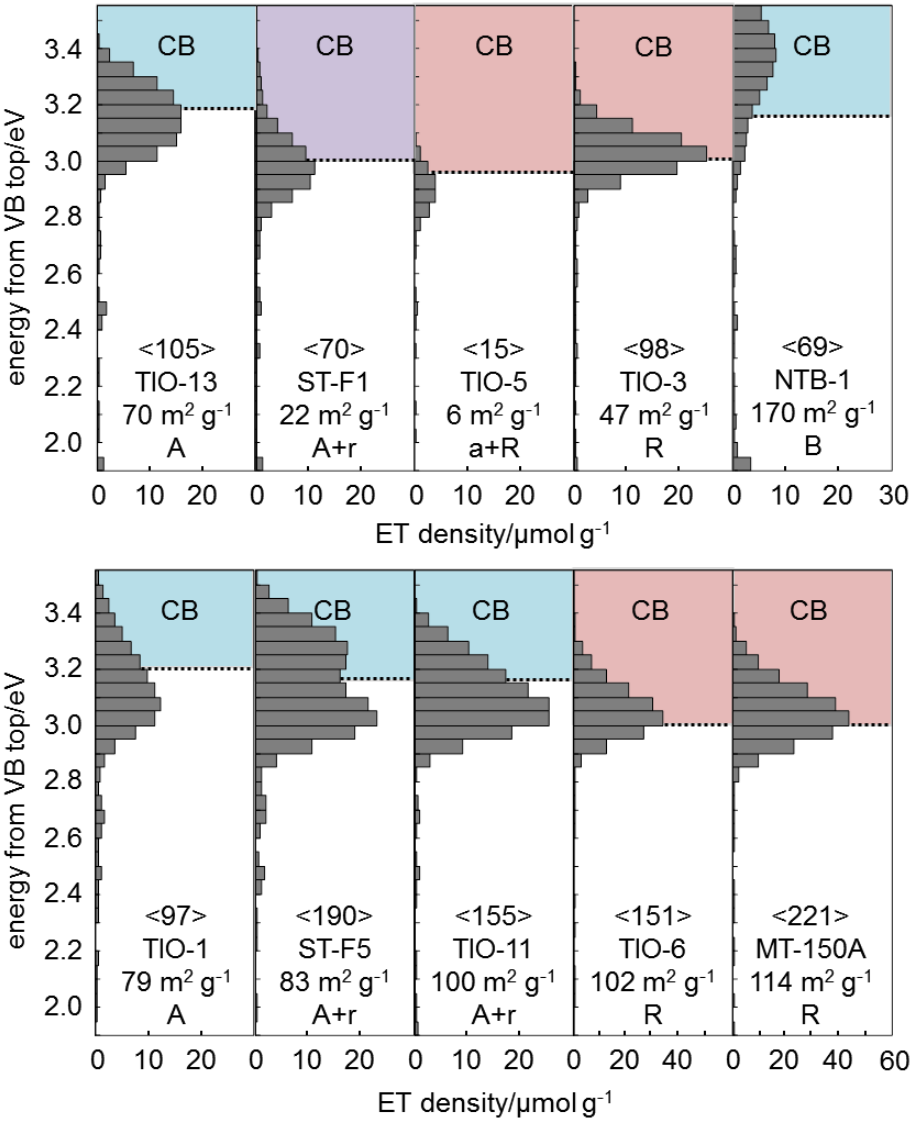

Figure 1-9 Representative ERDT/CBB patterns of commercial titania.

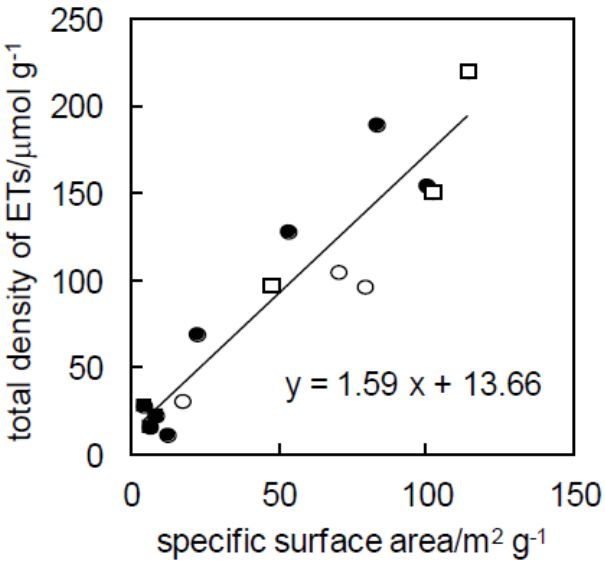

Figure 1-10 Relation with specific surface area and total ET density.

1.5.3 Degree of Coincidence of ERDT/CBB Patterns of Candidate Pairs Samples

In order to compare a given sample pairs, three kinds of parameters were adopted to evaluate similarity of ERDT/CBB patterns quantitatively. They are ζ_S, ζ_D and ζ_C which represents similarity of ERDT pattern shape, the total density of ETs and CBB position, respectively, and those formulas are

$$\zeta = \zeta_s \times {\zeta_D}^{\frac{1}{2}} \times {\zeta_C}^2 \qquad \textbf{(1-2)}$$

$$\zeta_S = 1 - \frac{\int |f(1) - \alpha f(2)|\, dE}{\int f(1)\, dE}\ ; \qquad \textbf{(1-3)}$$

$$\zeta_D = D(1)/D(2); \qquad \textbf{(1-4)}$$

$$\zeta_C = E_{CBB}(1)/E_{CBB}(2), \qquad \textbf{(1-5)},$$

where equation **(1-2)** shows degree of coincidence, which is comprehensive comparison including surface structure, bulk size and bulk structure; equation (**1-3**) reflects similarity in the distribution of ETs which represents surface structure of given samples; equation (**1-4**) and (**1-5**) compare the similarity in total density of ETs and CBB position, respectively. Through above formula, similarity of a pair of samples could be compared quantitatively with each other.

1.5.4 Interparticle Charge-Transfer Excitation

Very recently, interparticle spatial overlapping of orbitals to result in interparticle charge transfer excitation (ICTE) at an anatase-rutile interface was found during the course of RDB-PAS measurement of anatase-rutile mixture sample. [97] The energy of ERDT patterns are shown in reference to, in convenience, valence-band top. Therefore, the ERDT pattern of the mixture of anatase (ST-21) and rutile (ST-G1) samples should be reproduced by a simple summation of two ERDT pattern as SIM(0) as shown in **Figure**

1-11. However, the real patterns of mixture sample (mix-L and mix-H; different "mixing degree") are completely different from SIM(0). Actually, the ERDT pattern of SIM(0) showed higher similarity (ζ_s) with mix-0, that is loaded two samples separately. The ERDT pattern of mix-H showed higher ζ_s with simulated ERDT pattern of summation of ST-G1 pattern with 0.19-eV downward shifted ST-21 pattern. Sole possible interpretation of the shift is higher density of state (h-DOS) of valence band in rutile is located ca. 0.2 eV higher than that of anatase and charge-transfer excitation from valence band of rutile to ETs of anatase, i.e., interparticle charge-transfer excitation (ICTE), as shown in **Figure 1-12**.

As described above, energy of ETs is shown in reference to VBT position. However, this is employed just for convenience, because no other reference energy is available in RDB-PAS measurement. In practice, DOS at VBT is zero and thereby electrons are excited to ETs from higher DOS part (h-DOS) in VB as an assumption. At present the energy difference from VBT and energy range cannot be determined experimentally. Here, it is assumed that rutile h-DOS is 0.2-eV higher than that of anatase. When ERDT patterns are measured separately, the energy in ERDT patterns is shown in reference to each h-DOS energy. However, when these two kinds of titania particles are contacted electronically, it is expected that ETs in both particles are electron-filled by excitation from h-DOS of rutile, because wavelength of excitation is scanned from lower-energy side. As a result, the anatase peak position in ERDT pattern of the mixture is 0.2 eV-downward shifted. Thus, ERDT pattern of two or more mixture sample reflects relative band position of metal-oxides and mixture homogeneity of mixture samples.

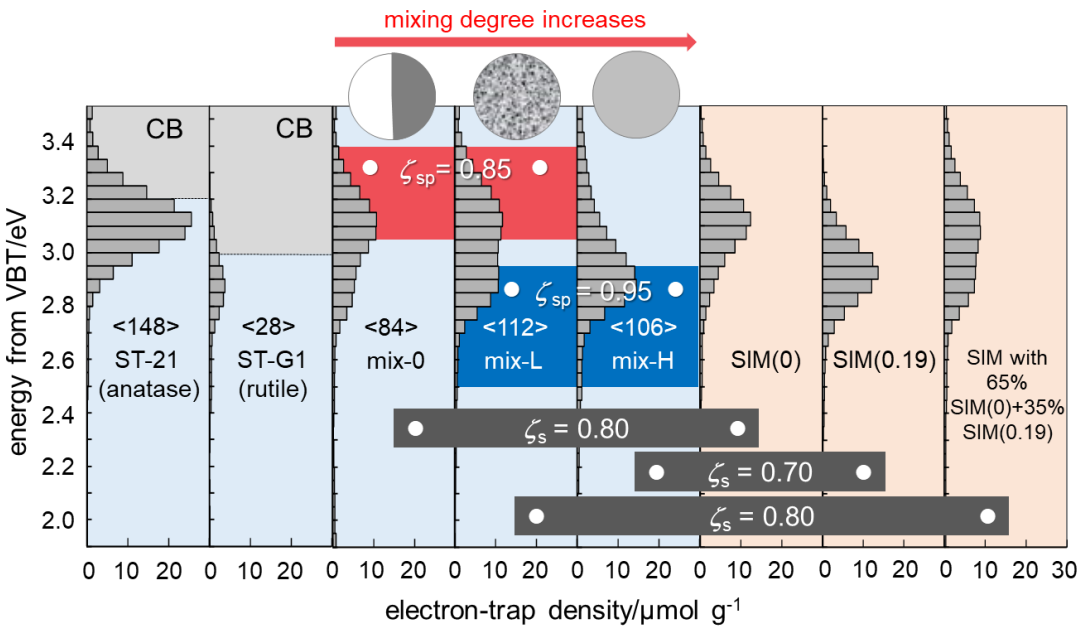

Figure 1-11 ERDT patterns of ST-21, ST-G1 and their 50/50 mixtures prepared by different mixing procedures, simulation patterns with energy shift of 0 eV and 0.19 eV, and summation pattern with SIM(0) and SIM(0.19) to reproduce the ERDT pattern of mix-L. The blue and orange colors in the background are experimental and simulation patterns, respectively.

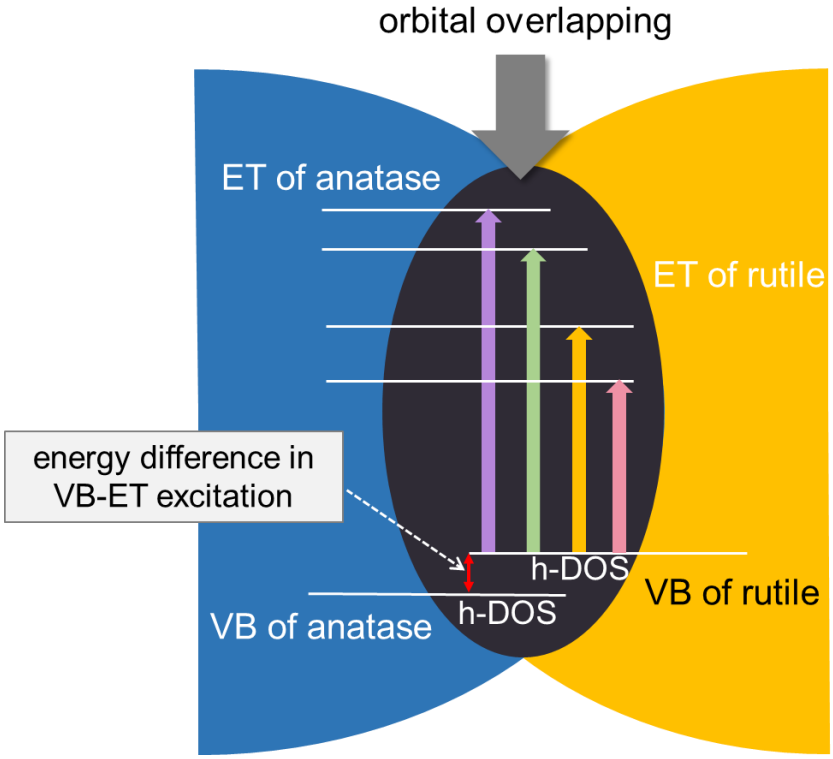

Figure 1-12 Schematic image of interparticle charge-transfer excitation.

1.6 *Purpose of This Study*

For solid materials, characterization of their structures is not straightforward compared with that for molecules. Since both bulk and surface structures should be characterized. Moreover, solids are sometimes not crystalline, that is, amorphous part may be included. The intrinsic but almost unrecognized problem is that only bulk crystalline structure is describable, that is, to be named. For example, anatase or rutile for titania samples. Surface structures are indescribable since we have no systematic nomenclature method for solid surfaces except for single crystals exposing only one type of a facet. Amorphous structures are entirely indescribable; therefore, they are practically called amorphous. In this sense, all the real solid samples are, at least partly, indescribable structures. In the long history of material science studies, we have discussed without description of surface and amorphous structures even if those structures are included in them. However, this doesn't mean intrinsically undetectable which means impossible to describe, but, in practice for solid surfaces, there are no methods for macroscopic surface analyses.

Categorizing solid material analytical methods with the scales of surface–bulk and macroscopic–microscopic, a large part of them are categorized to surface /microscopic ones. For example, scanning and transmission electron microscopies (SEM and TEM) and probe microscopies (STM and AFM) analyze solid surfaces microscopically and the results cannot be applied to whole surface or there is no guarantee for that the observed images are representative of a sample. Photoemission spectroscopies such as XPS can be a macroscopic surface analysis, but the available information is elemental composition (and valency) of the surface layers, not limited to an outermost layer, i.e., not structural information in a strict sense. Specific surface area evaluation based on the gas adsorption measurement is a macroscopic surface analysis, though what is measured is not structure, but the size of the surface. Meanwhile, the other part of analytical methods is categorized to bulk /macroscopic ones. For example, Raman spectroscopy and IR can be provided particular molecular information about vibrations, rotations, or other low-frequency transitions in molecules. [98] Solid-state NMR (SSNMR) is often applied for the characterization of organic compound, because it allows access to detailed information on molecular structure, dynamics, and domain morphology in small molecule. [99] Except for these analyses, such as measurements of electrochemical impedance (ECI) [100], zeta potential (ZP) [101] and temperature-programmed desorption (TPD) [102], which are applicable only for limited kinds of samples. Thus, there have been reported no macroscopic surface analysis techniques which provides the data reflecting the surface structure. Therefore, it seems that martial surface structure is limited to, e.g., particles exposing specific crystalline facets, and it can be said that almost all the amorphous or disordered solids are poorly characterized and discussed without information of true surface structure.

Recently, a novel technique developed by our lab could be benefit for filling up this gap about amorphous-solids macroscopic analysis. Reversed double-beam photoacoustic spectroscopy (RDB-PAS), enabling acquisition of patterns of energy-resolved distribution

of electron traps (ERDT)/conduction-band bottom (CBB) for semiconducting metal oxides [93-95] and amorphous material (such as, carbonitrides (C_3N_4) [96]), which have electron traps (ETs) as electron-accepting vacant electronic states. This suggests that ERDT/CBB pattern analysis is a powerful tool also for actual disordered or amorphous samples. It is noticed that the content of amorphous can be determined by the Rietveld analysis method but it is unclear that the difference in the amorphous structure among amorphous material. Even though amorphous TiO_2 nanoparticles have been obtained in practice, the understanding of amorphous structure and properties is still limited. The effects of amorphous content on the photocatalytic properties of titania have been observed, which means the properties of TiO_2 nanoparticles can be changed by varying the amorphous content in the samples. Moreover, there have been published a lot of papers on structure-sensitive photocatalytic activity. Hence in this study, I attempt to characterize and clarify the change in the structure of those amorphous samples produced through mechanical braying of three types of titania and their influence on photocatalytic activity.

1.7 References

[1] Website of Journal of Organic Chemistry. https://pubs.acs.org/journal/joceah.

[2] Connelly, N. G., Damhus, T., Hartshorn, R. M., Hutton, A. T., Nomenclature of Inorganic Chemistry, IUPAC Recommendations 2005, *RSC Adv.* **2005**, pp. 236.

[3] Lee, E.; Ahn, J.; Kwon, H.-C.; Ma, S.; Kim, K.; Yun, S.; Moon, J. All-Solution-Processed Silver Nanowire Window Electrode-Based Flexible Perovskite Solar Cells Enabled with Amorphous Metal Oxide Protection. *Adv. Energy Mater.* **2018**, *8* (9), 1702182.

[4] Yu, X.; Zeng, L.; Zhou, N.; Guo, P.; Shi, F.; Buchholz, D. B.; Ma, Q.; Yu, J.; Dravid, V. P.; Chang, R. P. H.; Bedzyk, M.; Marks, T. J.; Facchetti, A. Ultra-Flexible, "Invisible" Thin-Film Transistors Enabled by Amorphous Metal Oxide/Polymer Channel Layer Blends. *Adv. Mater.* **2015**, *27* (14), 2390–2399.

[5] Cedillo-González, E. I. Self-Cleaning Glass Prepared from a Commercial TiO_2 Nano-Dispersion and Its Photocatalytic Performance under Common Anthropogenic and Atmospheric Factors. *Build Environ.* **2014**, *71*, 7–14.

[6] Wang, G.; Wang, H.; Ling, Y.; Tang, Y.; Yang, X.; Fitzmorris, R. C.; Wang, C.; Zhang, J. Z.; Li, Y. Hydrogen-Treated TiO_2 Nanowire Arrays for Photoelectrochemical Water Splitting. *Nano Lett.* **2011**, *11* (7), 3026–3033.

[7] Pan, S.; Liu, X.; Guo, M.; Yu, S. fung; Huang, H.; Fan, H.; Li, G. Engineering the Intermediate Band States in Amorphous Ti^{3+} -Doped TiO_2 for Hybrid Dye-Sensitized Solar Cell Applications. *J. Mater. Chem. A* **2015**, *3* (21), 11437–11443.

[8] Wang, D.; Choi, D.; Li, J.; Yang, Z.; Nie, Z.; Kou, R.; Hu, D.; Wang, C.; Saraf, L. V.; Zhang, J.; Aksay, I. A.; Liu, J. Self-Assembled TiO_2–Graphene Hybrid Nanostructures for Enhanced Li-Ion Insertion. *ACS Nano* **2009**, *3* (4), 907–914.

[9] Zhou, T.; Zheng, Y.; Gao, H.; Min, S.; Li, S.; Liu, H. K.; Guo, Z. Surface Engineering and Design Strategy for Surface-Amorphized TiO_2@Graphene Hybrids for High Power Li-Ion Battery Electrodes. *Adv. Sci.* **2015**, *2* (9), 1500027.

[10] Han, J.; Hirata, A.; Du, J.; Ito, Y.; Fujita, T.; Kohara, S.; Ina, T.; Chen, M. Intercalation Pseudocapacitance of Amorphous Titanium Dioxide@nanoporous Graphene for High-Rate and Large-Capacity Energy Storage. *Nano Energy* **2018**, *49*, 354–362.

[11] Xue, D.; Song, H.; Zhong, X.; Wang, J.; Zhao, N.; Guo, H.; Cong, P. Flexible

Resistive Switching Device Based on the TiO_2 Nanorod Arrays for Non-Volatile Memory Application. *J. Alloys Compd.* **2020**, *822*, 153552.

[12] Farooq, T. Synthesis of Titanium Dioxide TiO_2 Thin Film to Achieve Resistive Switching Property for the Application of Nonvolatile Memory. *Mater. Today*, in press.

[13] Chen, X.; Liu, L.; Yu, P. Y.; Mao, S. S. Increasing Solar Absorption for Photocatalysis with Black Hydrogenated Titanium Dioxide Nanocrystals. *Science* **2011**, *331* (6018), 746–750.

[14] Suryanarayana, C. Mechanical Alloying and Milling. *Prog. Mater. Sci.* **2001**, 184.

[15] Gaffet, E.; Malhouroux-Gaffet, N. Nanocrystalline $MoSi_2$ Phase Formation Induced by Mechanically Activated Annealing. *J. Alloys Compd.* **1994**, *205* (1–2), 27–34.

[16] Düvel, A.; Morgan, L. M.; Cibin, G.; Pickup, D. M.; Chadwick, A. V.; Heitjans, P.; Sayle, D. C. Tuning Anti-Site Defect Density in Perovskite-$BaLiF_3$ via Ball-Milling/Heating-Cycling. *J. Phys. Chem. Lett.* **2018**, *9* (17), 5121–5124..

[17] Lao, Y. W.; Kuo, S. T.; Tuan, W. H. Influence of Ball Milling on the Sintering Behaviour of ZnO Powder. *Ceram. Int.* **2009**, *35* (3), 1317–1320.

[18] Zhou, X.; Liu, N.; Schmidt, J.; Kahnt, A.; Osvet, A.; Romeis, S.; Zolnhofer, E. M.; Marthala, V. R. R.; Guldi, D. M.; Peukert, W.; Hartmann, M.; Meyer, K.; Schmuki, P. Noble-Metal-Free Photocatalytic Hydrogen Evolution Activity: The Impact of Ball Milling Anatase Nanopowders with TiH_2. *Adv. Mater.* **2017**, *29* (5), 1604747.

[19] Wang, J.; Lin, Z. Anodic Formation of Ordered TiO_2 Nanotube Arrays: Effects of Electrolyte Temperature and Anodization Potential. *J. Phys. Chem. C* **2009**, *113* (10), 4026–4030.

[20] Wang, J.; Lin, Z. Freestanding TiO_2 Nanotube Arrays with Ultrahigh Aspect Ratio via Electrochemical Anodization. *Chem. Mater.* **2008**, *20* (4), 1257–1261.

[21] Gong, J.; Lai, Y.; Lin, C. Electrochemically Multi-Anodized TiO_2 Nanotube Arrays for Enhancing Hydrogen Generation by Photoelectrocatalytic Water Splitting. *Electrochim. Acta* **2010**, *55* (16), 4776–4782.

[22] Yin, H.; Liu, H.; Shen, W. Z. The Large Diameter and Fast Growth of Self-Organized TiO_2 Nanotube Arrays Achieved via Electrochemical Anodization. *Nanotechnology*. **2010**, *21* (3), 035601.

[23] Sulka, G. D.; Kapusta-Kołodziej, J.; Brzózka, A.; Jaskuła, M. Fabrication of Nanoporous TiO_2 by Electrochemical Anodization. *Electrochim. Acta* **2010**, *55* (14), 4359–4367.

[24] Sreekantan, S.; Saharudin, K. A.; Wei, L. C. Formation of TiO_2 Nanotubes via Anodization and Potential Applications for Photocatalysts, Biomedical Materials, and Photoelectrochemical Cell. *IOP Conf. Ser.: Mater. Sci. Eng.* **2011**, *21*, 012002.

[25] Sun, S.; Song, P.; Cui, J.; Liang, S. Amorphous TiO_2 Nanostructures: Synthesis, Fundamental Properties and Photocatalytic Applications. *Catal. Sci. Technol.* **2019**, *9* (16), 4198–4215.

[26] Liao, Y.; Que, W.; Zhong, P.; Zhang, J.; He, Y. A Facile Method to Crystallize Amorphous Anodized TiO_2 Nanotubes at Low Temperature. *ACS Appl. Mater. Interfaces* **2011**, *3* (7), 2800–2804.

[27] Nguyen, Q. A.; Bhargava, Y. V.; Devine, T. M. Titania Nanotube Formation in Chloride and Bromide Containing Electrolytes. *Electrochem. Commun.* **2008**, *10* (3), 471–475.

[28] Sheng, J.; Lee, H. -J.; Oh, S.; Park, J. -S. Flexible and High-Performance Amorphous Indium Zinc Oxide Thin-Film Transistor Using Low-Temperature Atomic Layer Deposition. *ACS Appl. Mater. Interfaces* **2016**, *8* (49), 33821–33828.

[29] Puurunen, R. L. Surface Chemistry of Atomic Layer Deposition: A Case Study for the Trimethylaluminum/Water Process. *J. Appl. Phys.* **2005**, *97* (12), 121301.

[30] Leskelä, M.; Ritala, M. Atomic Layer Deposition Chemistry: Recent Developments and Future Challenges. *Angew. Chem. Int. Ed.* **2003**, *42* (45), 5548–5554.

[31] Ban, C.; Xie, M.; Sun, X.; Travis, J. J.; Wang, G.; Sun, H.; Dillon, A. C.; Lian, J.; George, S. M. Atomic Layer Deposition of Amorphous TiO_2 on Graphene as an Anode for Li-ion Batteries. *Nanotechnology.* **2013**, 24 (42), 424002.

[32] Edy, R.; Zhao, Y.; Huang, G. S.; Shi, J. J.; Zhang, J.; Solovev, A. A.; Mei, Y. TiO_2 Nanosheets Synthesized by Atomic Layer Deposition for Photocatalysis. *Prog. Nat. Sci.* **2016**, *26* (5), 493–497.

[33] Wang, Z.; Yang, C.; Lin, T.; Yin, H.; Chen, P.; Wan, D.; Xu, F.; Huang, F.; Lin, J.; Xie, X.; Jiang, M. Visible-Light Photocatalytic, Solar Thermal and Photoelectrochemical Properties of Aluminium-Reduced Black Titania. *Energy Environ. Sci.* **2013**, *6* (10), 3007.

[34] Sinhamahapatra, A.; Jeon, J.-P.; Yu, J.-S. A New Approach to Prepare Highly Active and Stable Black Titania for Visible Light-Assisted Hydrogen Production. *Energy Environ. Sci.* **2015**, *8* (12), 3539–3544.

[35] Wang, X.; Ma, B.; Xue, J.; Wu, J.; Chang, J.; Wu, C. Defective Black Nano-Titania Thermogels for Cutaneous Tumor-Induced Therapy and Healing. *Nano Lett.* **2019**, *19* (3), 2138–2147.

[36] Liu, L.; Chen, X. Titanium Dioxide Nanomaterials:Self-Structural Modifications. *Chem. Rev.* **2014**, *114* (19), 9890–9918.

[37] Myung, S.-T.; Kikuchi, M.; Yoon, C. S.; Yashiro, H.; Kim, S.-J.; Sun, Y.-K.; Scrosati, B. Black Anatase Titania Enabling Ultra High Cycling Rates for Rechargeable Lithium Batteries. *Energy Environ. Sci.* **2013**, *6* (9), 2609.

[38] Salari, M.; Konstantinov, K.; Liu, H. K. Enhancement of the Capacitance in TiO2 Nanotubes through Controlled Introduction of Oxygen Vacancies. *J. Mater. Chem.* **2011**, *21* (13), 5128.

[39] Pei, Z.; Ding, L.; Lin, H.; Weng, S.; Zheng, Z.; Hou, Y.; Liu, P. Facile Synthesis of Defect-Mediated TiO_{2-x} with Enhanced Visible Light Photocatalytic Activity. *J. Mater. Chem. A* **2013**, *1* (35), 10099.

[40] Zhu, Q.; Peng, Y.; Lin, L.; Fan, C.-M.; Gao, G.-Q.; Wang, R.-X.; Xu, A.-W. Stable Blue TiO_2-x Nanoparticles for Efficient Visible Light Photocatalysts. *J. Mater. Chem. A* **2014**, *2*, 4429–4437.

[41] Grabstanowicz, L. R.; Gao, S.; Li, T.; Rickard, R. M.; Rajh, T.; Liu, D.-J.; Xu, T. Facile Oxidative Conversion of TiH_2 to High-Concentration Ti^{3+}-Self-Doped Rutile TiO_2 with Visible-Light Photoactivity. *Inorg. Chem.* **2013**, *52* (7), 3884–3890.

[42] Zou, J.; Gao, J.; Xie, F. An Amorphous TiO_2 Sol Sensitized with H_2O_2 with the Enhancement of Photocatalytic Activity. *J. Alloys Compd.* **2010**, *497* (1–2), 420–427.

[43] Zou, X.; Liu, J.; Su, J.; Zuo, F.; Chen, J.; Feng, P. Facile Synthesis of Thermal- and Photostable Titania with Paramagnetic Oxygen Vacancies for Visible-Light Photocatalysis. *Chem. Eur. J.* **2013**, *19* (8), 2866–2873.

[44] Park, J.-S.; Walsh, A. Embrace Your Defects. *Nat Energy* **2019**, *4* (2), 95–96.

[45] Na-Phattalung, S.; Smith, M. F.; Kim, K.; Du, M.-H.; Wei, S.-H.; Zhang, S. B.; Limpijumnong, S. First-Principles Study of Native Defects in Anatase TiO_2. *Phys. Rev. B*

2006, *73* (12), 125205.

[46] Sanz, J.; Soria, J.; Sobrados, I.; Yurdakal, S.; Augugliaro, V. Influence of Amorphous TiO_{2-x} on Titania Nanoparticle Growth and Anatase-to-Rutile Transformation. *J. Phys. Chem. C* **2012**, *116* (8), 5110–5115.

[47] Wei, T.; Zhu, Y.-N.; An, X.; Liu, L.-M.; Cao, X.; Liu, H.; Qu, J. Defect Modulation of Z-Scheme TiO_2 /Cu_2O Photocatalysts for Durable Water Splitting. *ACS Catal.* **2019**, *9* (9), 8346–8354.

[48] Ji, Y.; Luo, Y. New Mechanism for Photocatalytic Reduction of CO_2 on the Anatase TiO_2(101) Surface: The Essential Role of Oxygen Vacancy. *J. Am. Chem. Soc.* **2016**, *138*(49), 15896–1590.

[49] Dohnálek, Z.; Lyubinetsky, I.; Rousseau, R. Thermally-Driven Processes on Rutile TiO_2(110)-(1×1): A Direct View at the Atomic Scale. *Prog. Surf. Sci.* **2010**, *85* (5–8), 161–205.

[50] Henderson, M. A. A Surface Perspective on Self-Diffusion in Rutile TiO_2. *Surface Science* **1999**, *419*(2–3), 174-187.

[51] Wendt, S.; Sprunger, P. T.; Lira, E.; Madsen, G. K. H.; Li, Z.; Hansen, J. Ø.; Matthiesen, J.; Blekinge-Rasmussen, A.; Lægsgaard, E.; Hammer, B.; Besenbacher, F., The Role of Interstitial Sites in the Ti3d Defect State in the Band Gap of Titania, *Scinece* **2008**, 320 (5884), 1755-1759.

[52] Wendt, S.; Bechstein, R.; Porsgaard, S.; Lira, E.; Hansen, J. Ø.; Huo, P.; Li, Z.; Hammer, B.; Besenbacher, F. Comment on "Oxygen Vacancy Origin of the Surface Band-Gap State of TiO_2 (110)". *Phys. Rev. Lett.* **2010**, *104* (25), 259703.

[53] Shibata, N.; Goto, A. Direct Imaging of Reconstructed Atoms on TiO_2 (110) Surfaces. **2008**, *322*(5901), 570-573.

[54] Morita, K.; Shibuya, T.; Yasuoka, K. Stability of Excess Electrons Introduced by Ti Interstitial in Rutile TiO_2 (110) Surface. *J. Phys. Chem. C* **2017**, *121* (3), 1602–1607.

[55] Nowotny, J.; Bak, T.; Burg, T.; Nowotny, M. K.; Sheppard, L. R. Effect of Grain Boundaries on Semiconducting Properties of TiO_2 at Elevated Temperatures. *J. Phys. Chem. C* **2007**, *111*(27), 9769–9778.

[56] Bryan, J. D.; Heald, S. M.; Chambers, S. A.; Gamelin, D. R. Strong Room-Temperature Ferromagnetism in Co^{2+}-Doped TiO_2 Made from Colloidal Nanocrystals. *J.*

Am. Chem. Soc. **2004**, *126* (37), 11640–11647.

[57] Wallace, S. K.; McKenna, K. P. Grain Boundary Controlled Electron Mobility in Polycrystalline Titanium Dioxide. *Adv. Mater. Interfaces* **2014**, *1* (5), 1400078.

[58] Ohtani, B. Preparing Articles on Photocatalysis–Beyond the Illusions, Misconceptions, and Speculation. *Chem. Lett.* **2008**, 37(3), 216-229.

[59] Ohtani, B.; Prieto-Mahaney, O. O.; Li, D.; Abe, R. What Is Degussa (Evonik) P25? Crystalline Composition Analysis, Reconstruction from Isolated Pure Particles and Photocatalytic Activity Test. *J. Photochem. Photobiol. A* **2010**, *216* (2–3), 179–182.

[60] O'Connell, K.; Regalbuto, J. R. High Sensitivity Silicon Slit Detectors for 1 Nm Powder XRD Size Detection Limit. *Catal Lett* **2015**, *145* (3), 777–783.

[61] Nath, D.; Singh, F.; Das, R. X-Ray Diffraction Analysis by Williamson-Hall, Halder-Wagner and Size-Strain Plot Methods of CdSe Nanoparticles- a Comparative Study. *Mater. Chem. Phys.* **2020**, *239*, 122021.

[62] Kibasomba, P. M.; Dhlamini, S.; Maaza, M.; Liu, C.-P.; Rashad, M. M.; Rayan, D. A.; Mwakikunga, B. W. Strain and Grain Size of TiO2 Nanoparticles from TEM, Raman Spectroscopy and XRD: The Revisiting of the Williamson-Hall Plot Method. *Results Phys.* **2018**, *9*, 628–635.

[63] Sun, C.; Müller, E.; Meffert, M.; Gerthsen, D., On the progress of scanning transmission electron microscopy (STEM) imaging in a scanning electron microscope. *Microsc. Microanal.* **2018**, *24*(2), 99-106.

[64] Zhang, J.; Zhang, Y.; Lei, Y.; Pan, C. Photocatalytic and Degradation Mechanisms of Anatase TiO_2: A HRTEM Study. *Catal. Sci. Technol.* **2011**, *1* (2), 273.

[65] Tian, M.; ; Mahjouri-Samani, M.; Eres, G.; Sachan, R.; Yoon, M.; Chisholm, M. F.; Wang, K.; Puretzky, A. A.; Rouleau, C. M.; Geohegan, D. B.; Duscher, G., Structure and formation mechanism of black TiO_2 nanoparticles. *ACS nano.* **2015**, *9*(10), 10482-10488.

[66] Binnig, G.; Rohrer, H., Scanning tunneling microscopy. *IBM J Res Dev* **2000**, *44*(1),279-293.

[67] Wintterlin, J.; Wiechers, J.; Brune, H.; Gritsch, T. *Phys. Rev. Lett.* **1989**, *62*(1), 59-62.

[68] Güntherodt, H.-J.; Wiesendanger, R., Scanning Tunneling Microscopy I; *Surface*

Sciences **1994**, 20.

[69] Setvín, M.; Aschauer, U.; Scheiber, P.; Li, Y.-F.; Hou, W.; Schmid, M.; Selloni, A.; Diebold, U. Reaction of O_2 with Subsurface Oxygen Vacancies on TiO_2 Anatase (101). *Science* **2013**, *341* (6149), 988–991.

[70] Yim, C. M.; Watkins, M. B.; Wolf, M. J.; Pang, C. L.; Hermansson, K.; Thornton, G. Engineering Polarons at a Metal Oxide Surface. *Phys. Rev. Lett.* **2016**, *117* (11), 116402.

[71] Setvin, M.; Schmid, M.; Diebold, U. Aggregation and Electronically Induced Migration of Oxygen Vacancies in TiO_2 Anatase. *Phys. Rev. B* **2015**, *91*, 195403.

[72] Federici Canova F, Foster AS. The role of the tip in non-contact atomic force microscopy dissipation images of ionic surfaces. *Nanotechnology* **2011**, 22(4), 045702.

[73] Diebold, U. The Surface Science of Titanium Dioxide. *Surf. Sci. Rep.* **2003**, *48* (5–8), 53–229.

[74] Johnson, D.; Hilal, N. Characterisation and Quantification of Membrane Surface Properties Using Atomic Force Microscopy: A Comprehensive Review. *Desalination* **2015**, *356*, 149–164.

[75] Setvin, M.; Hulva, J.; Parkinson, G. S.; Schmid, M.; Diebold, U. Electron Transfer between Anatase TiO_2 and an O_2 Molecule Directly Observed by Atomic Force Microscopy. *Proc. Natl. Acad. Sci. U.S.A.* **2017**, *114* (13), 2556–2562.

[76] Sham, T. K.; Lazarus, M. S., *Chem. Phys. Lett.* **1997**, 68(2–3),426–432.

[77] Marcì, G.; Augugliaro, V.; López-Muñoz, M. J.; Martín, C.; Palmisano, L.; Rives, V.; Schiavello, M.; Tilley, R. J. D.; Venezia, A. M., *J. Phys. Chem. B* **2001**, *105*, 1026-1032.

[78] Wang, Y.; Cao, X.; Hu, Q.; Liang, X.; Tian, T.; Lin, J.; Yue, M.; Ding, Y., FeO_x Derived from an Iron-Containing Polyoxometalate Boosting the Photocatalytic Water Oxidation Activity of Ti^{3+}-Doped TiO_2. *ACS Appl. Mater. Interfaces.* **2019**, *11*(26), 23135-23143.

[79] Zhou, X.; Zolnhofer, E. M.; Nguyen, N.T.; Liu, N.; Meyer, K.; Schmuki, P., Stable Co-Catalyst-Free Photocatalytic H_2 Evolution From Oxidized Titanium Nitride Nanopowders. *Angew Chem. Int. Ed. Engl.* **2015**, 2, *54*(45),13385-13389.

[80] Zeng, L.; Song, W.; Li, M.; Zeng, D.; Xie, C. Catalytic Oxidation of Formaldehyde

on Surface of $HTiO_2$/$HCTiO_2$ without Light Illumination at Room Temperature. *Appl. Catal. B* **2014**, *147*, 490–498.

[81] Desrosiers, M.; Schauer, D. A. Electron Paramagnetic Resonance (EPR) *Biodosimetry*. **2001**, *184*(1-2), 219-228.

[82] Xu, J. Molten Salt Assisted Synthesis of Black Titania Hexagonal Nanosheets with Tuneable Phase Composition and Morphology. *RSC Advances* **2015**, *5*, 85928–85932.

[83] Su, T.; Yang, Y.; Na, Y.; Fan, R.; Li, L.; Wei, L.; Yang, B.; Cao, W. An Insight into the Role of Oxygen Vacancy in Hydrogenated TiO_2 Nanocrystals in the Performance of Dye-Sensitized Solar Cells. *ACS Appl. Mater. Interfaces* **2015**, *7* (6), 3754–3763.

[84] Chong, S. V.; Kadowaki, K.; Xia, J.; Idriss, H. Interesting Magnetic Behavior from Reduced Titanium Dioxide Nanobelts. *Appl. Phys. Lett.* **2008**, *92* (23), 232502.

[85] Yang, C.; Wang, Z.; Lin, T.; Yin, H.; Lü, X.; Wan, D.; Xu, T.; Zheng, C.; Lin, J.; Huang, F.; Xie, X.; Jiang, M. Core-Shell Nanostructured "Black" Rutile Titania as Excellent Catalyst for Hydrogen Production Enhanced by Sulfur Doping. *J. Am. Chem. Soc.* **2013**, *135* (47), 17831–17838.

[86] Tam, A. C. Applications of Photoacoustic Sensing Techniques. *Rev. Mod. Phys.* **1986**, *58* (2), 381–431.

[87] Patimisco, P.; Scamarcio, G.; Tittel, F.-K.; Spagnolo, V. Quartz-Enhanced Photoacoustic Spectroscopy: A Review. *Sensors* **2014**, *14*, 6165-6206.

[88] Murakami, N.; Mahaney, O. O. P.; Abe, R.; Torimoto, T.; Ohtani, B. Double-Beam Photoacoustic Spectroscopic Studies on Transient Absorption of Titanium(IV) Oxide Photocatalyst Powders. *J. Phys. Chem. C* **2007**, *111*, 11972−11935.

[89] Ohtani, B., Titania Photocatalysis beyond Recombination: A Critical Review. *Catalysts* **2013**, *3* (4), 942–953.

[90] Carey, J. J.; McKenna, K. P. Screening Doping Strategies To Mitigate Electron Trapping at Anatase TiO_2 Surfaces. *J. Phys. Chem. C* **2019**, *123*, 22358−22367.

[91] Wang, Q.; Zhang, Z.; Zakeeruddin,S. M.; Graẗzel, M. Enhancement of the Performance of Dye-Sensitized Solar Cell by Formation of Shallow Transport Levels Under Visible Light Illumination. *J. Phys. Chem. C* **2008**, *112*, 7084−7092.

[92] Weidmann, J.; Dittrich, T.; Konstantinova, E.; Lauermann, I.; Uhlendorf, I.; Koch, F.

Influence of Oxygen and Water Related Surface Defects on the Dye Sensitized TiO_2 Solar Cell. *Sol. Energy Mater. Sol. Cells* **1999**, *56*, 153−165.

[93] Nitta, A.; Takase, M.; Takashima, M.; Murakami, N.; Ohtani, B., A Fingerprint of Metal-Oxide Powders: Energy-Resolved Distribution of Electron Traps., *Chem. Commun.* **2016**, *52*, 12096-12099.

[94] Nitta, A.; Takashima, M.; Takase, M.; Ohtani, B. Identification and Characterization of Titania Photocatalyst Powders Using Their Energy-Resolved Distribution of Electron Traps as a Fingerprint. *Catal. Today* **2019**, *321–322*, 2–8.

[95] Nitta, A.; Takashima, M.; Murakami, N.; Takase, M.; Ohtani, B., Reversed Double-Beam Photoacoustic Spectroscopy of Metal-Oxide Powders for Estimation of Their Energy-Resolved Distribution of Electron Traps and Electronic-Band Structure. *Electrochim. Acta* **2018**, *264*, 83-90.

[96] Chuaicham, C.; Karthikeyan, S.; Pawar, R.; Xiong, Y.; Ohtani, B.; Kim, Y.; Song, J. T.; Ishihara, T. Energy-Resolved Distribution of Electron Traps for O/S-Doped Carbon Nitrides by Reversed Double-Beam Photoacoustic Spectroscopy and the Photocatalytic Reduction of Cr(VI). *Chem. Commun*. **2020**, *56*, 3793-3796.

[97] Shen, Y.; Nitta, A.; Takashima, M.; Ohtani, B., Do particles interact electronically? ―Proof of Interparticle Charge-Transfer Excitation between Adjoined Anatase and Rutile Particles, *Chem. Lett.*, **2021**, *50*, 80-83.

[98] Nitsche, D., Hess, C., Structure of Isolated Vanadia and Titania: A Deep UV Raman, UV–Vis, and IR Spectroscopic Study, *J. Phys. Chem. C* **2016**, *120*(2), 1025–1037.

[99] Bak, M.; Rasmussen, J. T.; Nielsen, N. C., SIMPSON: A general simulation program for solid-state NMR spectroscopy. *J. Magn. Reson.* **2000**, *147*, 296–330.

[100] Ahmadi, M.; Guinel, M. J., Synthesis, Characterization and Understanding of The Mechanisms of Electroplating of Nanocrystalline–amorphous Nickel–tungsten Alloys Using *in situ* Electrochemical Impedance Spectroscopy. *J. Alloys Compd.* **2013**, *574*, 196−205.

[101] Bhattacharjee, S., DLS and Zeta Potential−What they are and What they are not? *J. Control Release* **2016**, *235*, 337−351.

[102] Samokhvalov, A.; Duin, E. C.; Nair, S.; Bowman, M.; Davis, Z.; Tatarchuk, B. J., Study of the Surface Chemical Reactions of Thiophene with Ag/Titania by the Complementary Temperature-Programmed Electron Spin Resonance, Temperature-

Programmed Desorption, and X-ray Photoelectron Spectroscopy: Adsorption, Desorption, and Sorbent Regeneration Mechanisms. *J. Phys. Chem. C* **2010**, *114*, 4075–4085

Chapter 2

Experimental

2.1 Materials

In this study, commercial titania samples of rutile (Showa Denko, ST-G1), anatase (MERCK) and brookite (Kojundo Chemical Laboratory, TIO19PB) were used as starting materials. In addition, amorphous titania (Wako Pure Chemical Industries, amorphous) and single-crystalline anatase (Ishihara Sangyo, ST-21) were introduced as references. The physical properties of those titania are summarized in **Table 2-1**. It should be noted that ST-G1 is composed of rutile only, i.e., no anatase inclusion, however, in Merck, small amount of rutile is included and in brookite, small amount of anatase is included. Therefore, ST-21 was used to avoid confusion when I performed control experiments in chapters 4 and 5.

Table 2-1 Physical properties of titania used in this study.

crystalline	code	SSA [1]/m^2 g^{-1}	crystalline composition (%) [2]			
			anatase	rutile	brookite	non-crystal
rutile	ST-G1	11	-	86	-	14
anatase	Merck	12	92	2	-	6
brookite	HPC	43	5	-	77	18
amorphous	AMO	>200				100
anatase	ST-21	67	87	-	-	13

[1] Specific surface area measured by nitrogen adsorption.

[2] Crystalline composition were calculated from Rietveld analysis with nickel(II) oxide as described in section 2.4.4.

2.2 Braying and post-calcination

To apply changes in structure, mechanical milling was common method since many papers have already reported the amorphization of titania samples by ball milling [1-2]. However, it has been also observed that ball milling using zirconia beads induces heavy contamination of less detectable zirconia up to 10wt% [3-4], and this idea about contamination by ball milling process is common sense. To avoid this kind of contamination from the materials used for milling, in my study, braying was employed with mortar and pestle as a less contaminant method, and for the longer braying, automatic mortar was introduced as shown in **Figure 2-1**.

As a general procedure for braying, 5 g of sample was placed in automatic agate mortar

(Nitto Kagaku ANM-1000) to be brayed up to 10 d. The mortar turned anticlockwise at ca. 25 rpm and the pestle turned eccentrically at ca. 100 rpm. The contact pressure between the pestle and mortar is ca. 7 N. Powder pressed and adhered on the mortar inside-wall was scraped off by a silicone-rubber scraper. For the braying longer than 1 d, powder was manually mixed every 24 h. It should be noted that those brayed samples with different braying time were prepared independently, not successive processes. For example, the 2-day brayed sample was not prepared by additional one-day braying to the one-day brayed sample. In other words, when I prepared 2-day brayed sample, I placed 5 g sample in mortar and brayed for 2 day continuously. Then, when I prepared 3-day brayed sample, I placed another 5 g sample in mortar and brayed. Thus, it should be noted that the structures might not be changed smoothly with the time brayed.

After braying for a given time, a part of brayed sample was post-calcined in air by laboratory-made rotary electric furnace as shown in **Figure 2-2**. The sample (typically 3 g) was placed in a quartz tube with four dimples inside to work as baffles, and the tube was heated in an electric furnace under rotation speed of ca. 70 rpm to make homogeneous heating of the sample. The temperature was raised from room temperature to 773 K at a rate of 0.5 K min^{-1}, kept constant at 773 K for 3 h and then allowed to be cooled down.

Those treated brayed samples were coded as, e.g., "b5" for a 5-d brayed sample. For post-calcined, those samples were coded by adding "c" after the code of the original brayed sample, such like, "b5c".

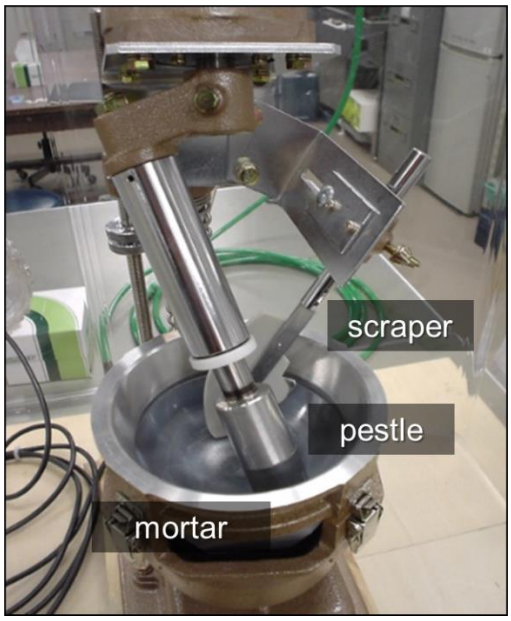

Figure 2-1 Automatic agate mortar.

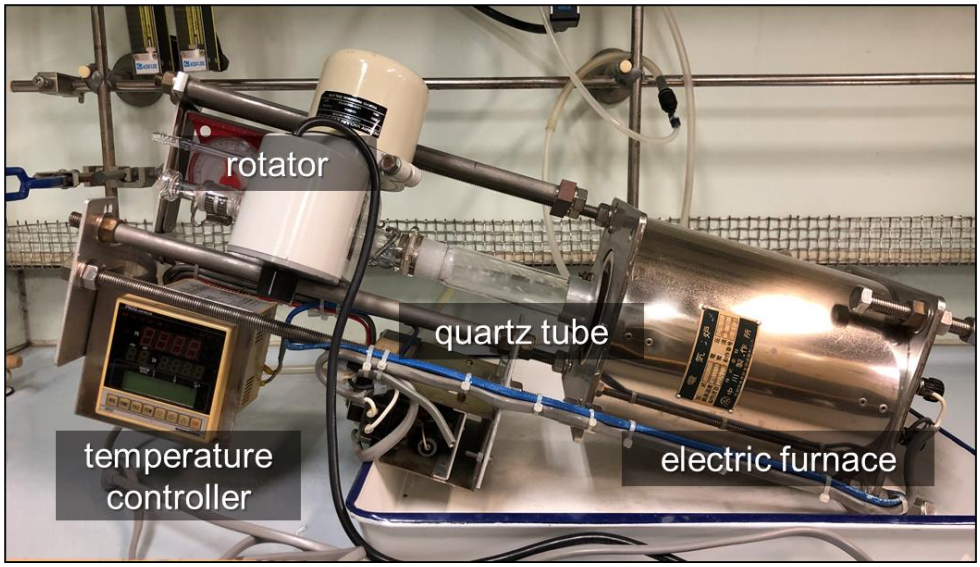

Figure 2-2 Laboratory-made rotary electric furnace with a quartz tube.

2.3 Photocatalytic Activity Test

Three kinds of photocatalytic reactions were employed to evaluate photocatalytic activities of the samples.

One is dehydrogenation of methanol with in-situ platinum photodeposition (H_2 system); a 50-mg portion of the sample powder was suspended in aqueous solution containing 5 ml of 50-vol % methanol and a certain amount of chloroplatinic acid (H_2PtCl_6, Wako Pure Chemical Industries) which corresponds to 2 wt.% platinum. Air was purged off by passing argon through the suspensions for at least 15 min, the sample tubes were sealed tightly with a rubber septum, and they were irradiated by a 400-W high-pressure mercury arc (Eiko-sha 400) at 298 K under vigorous magnetic stirring (1000 rpm).

The other is oxidative decomposition of acetic acid (CO_2 system); a sample powder (50 mg) and 5 ml of aqueous solution of acetic acid (5vol%) were put into a borosilicate-glass tube (transparent at > 290 nm). The suspension was irradiated by the same irradiation equipment and conditions as mentioned in H_2 system.

The last one is oxygen evolution from water with in-situ silver photodeposition (O_2 system); a sample powder (50 mg) was suspended in 5 mL of deaerated aqueous silver nitrate (0.05 mol L^{-1}) and irradiated using the same photoirradiation setup as H_2 and CO_2 system.

All the reactions were monitored by analyzing the liberation of H_2, CO_2 and O_2, respectively, by using gas chromatography (a Shimadzu GC-8A gas chromatograph equipped with a TCD and columns of molecular sieve 5A for H_2 and O_2 and Porapak Q for CO_2). Photocatalytic activities were calculated as the rates of product liberation.

2.4 Conventional analytical methods

2.4.1 Scanning electron microscopy

Morphology of the samples was analyzed by a field-emission scanning electron microscope (JEOL JSM-7400F) operated in the mode of low secondary-electron image (LEI) with measurement current of 10.0 mA, electron-acceleration voltage of 2.0–10.0 kV and working distance of 6 mm. The powder sample was placed on a piece of carbon tape attached on a brass sample holder, then the sample holder was dried overnight at <5 kPa.

2.4.2 Specific surface area measurement

Specific surface area (SSA) of the samples was calculated by the Brunauer–Emmett–Teller (BET) equation through nitrogen adsorption at 77 K with Yuasa Ionics Autosorb 6AG. Before the measurement, the samples were kept at 473 K for 2 h to remove adsorbing materials such as water.

2.4.3 Diffuse-reflectance spectroscopy

Diffuse reflectance spectra (DRS) of the samples were measured in the range of 200 nm to 800 nm by using ultraviolet and visible spectrophotometer (Jasco V-670) equipped with an integrating sphere attachment (PIN-757). As a reference, barium sulfate (Wako Pure Chemical Industries, $BaSO_4$) was used for baseline to calibrate the spectra as absorption (%) (= 100 – %reflectance).

2.4.4 X-ray diffractometry

Crystalline composition and crystallinity of the samples were evaluated by X-ray diffractometry with Rigaku SmartLab X-ray diffractometer. The X-ray diffraction (XRD) patterns were recorded with Cu K_α radiation (λ= 1.5418 Å), acceleration voltage of 40 kV, current of 30 mA, scanning rate of 1.0° min^{-1}, step of 0.02° and 2θ range of 3–80°. The obtained diffractograms were analyzed by using PDXL software including a RIETAN-FP Rietveld analysis package.

The crystallite size and lattice strain were calculated by using the Halder–Wagner method [5] installed in the PDXL as below

$$\left(\frac{\beta_{tot}\cos\theta}{\sin\theta}\right)^2 = \frac{K\lambda}{D_{HW}} \times \frac{\beta_{tot}\cos\theta}{\sin^2\theta} + 16\varepsilon_{HW}^2,$$

where D_{HW} and ε_{HW} are Halder-Wagner crystallite size and strain, respectively. The reason why I employed Halder–Wagner method taking lattice strain into consideration instead of Scherrer equation, which is more common when we estimate crystallite size, was because peak broadening was observed after long-time braying due to lattice strain and smaller crystallite size.

To determine the crystalline content (the ratio of crystalline to non-crystalline (NC) composition), nickel(II) oxide (Wako Pure Chemical Industries, NiO, 99.9%) was mixed as an internal standard with a sample in the weight ratio of 20:80. The crystallinity of NiO was determined as 96.6% for crystal and 3.4% for amorphous by using lanthanum hexaboride (National Institute of Standard and Technology SPM660b, LaB_6) as a reference assuming 100% crystallinity. [6] Rietveld analysis was applied to the obtained XRD pattern and calculate the crystalline content with following equation,

$$\frac{80\%(1-3.4\%)}{20\%(1-x\%)} = \frac{\text{Ratio of NiO among total crystal content}}{\text{Ratio of } TiO_2 \text{ among total crystal content}},$$

where x represents NC amount of titania.

2.5 RDB-PAS measurement

In this study, laboratory-made RDB-PAS instruments (code name BK1 (used for brayed and post-calcined samples) and SP1 (used for simulations in the section e.g., 3.4.2 and control experiments with mixture samples in the section e.g., 3.4.3)) were used. It is composed of a grating monochromator with a xenon lamp (Bunkokeiki M10-RP/BXL-150 for BK1 and Spectral Products CM110/Eagle Engineering R300-3J for SP1) equipped with a Excelitas Technologies Cermax 300-W xenon lamp (PE300B-10UV)), a 625-nm LED (Luxeon LXHL-ND98) intensity-modulated at 35 Hz by a digital function generator (NF Corporation DF-1906), a UV quartz combiner light guide (Moritex MXS5-1000S-UV3), a digital lock-in amplifier (NF Corporation LI5630) and a photoacoustic (PA) cell equipped with a quartz window, gas-tight bulbs, a MEMS (micro-electro-mechanical system) microphone module (SparkFun MEMS Microphone Breakout, INMP401 (ADMP401)) and a stainless-steel sample holder.

Typical RDB-PAS measurement procedures are as follows. A sample powder (ca. 50–100 mg) was loaded on a stainless sample holder and placed in a PA cell. The cell was transferred to a cubic acrylic box. Methanol-saturated nitrogen was introduced in the cell for at least 30 min to remove oxygen, then the cell was sealed tightly. Two light beams were introduced to the cell through a quartz window. One is continuous monochromatic light wavelength-scanned from longer wavelength to shorter wavelength (typically 600–300 nm) with 5-nm step. The other is an intensity-modulated (35 Hz) 625-nm LED. PA signal was amplified with a lock-in amplifier and recorded as RDB-PA spectrum showing the accumulation of electrons in ETs as shown in **Figure 2-3**(a). The spectrum was differentiated from lower energy-side to obtain an ERDT pattern followed by calibration with experimentally determined conversion coefficient to absolute density of ETs (**Figure 2-3**(b)). The energy of ETs is shown in reference to valence-band top (VBT) energy for convenience and thus-obtained ERDT pattern was replotted as a bar graph with a pitch of 0.05 eV as shown in e.g., **Figure 3-9**.

Conduction-band bottom (CBB) energy was estimated by (single beam) PAS using the

same setups. The sample in a PA cell was irradiated by modulated (80 or 35 Hz) monochromatic light wavelength-scanned from longer wavelength to shorter wavelength to obtain PA spectrum, which was then calibrated with a spectrum of carbon black (**Figure 2-3**(c)). To determine the absorption-edge wavelength, bandgap energy in the unit of eV was calculated and plotted as CBB in reference to VBT as shown in e.g., **Figure 3-9**.

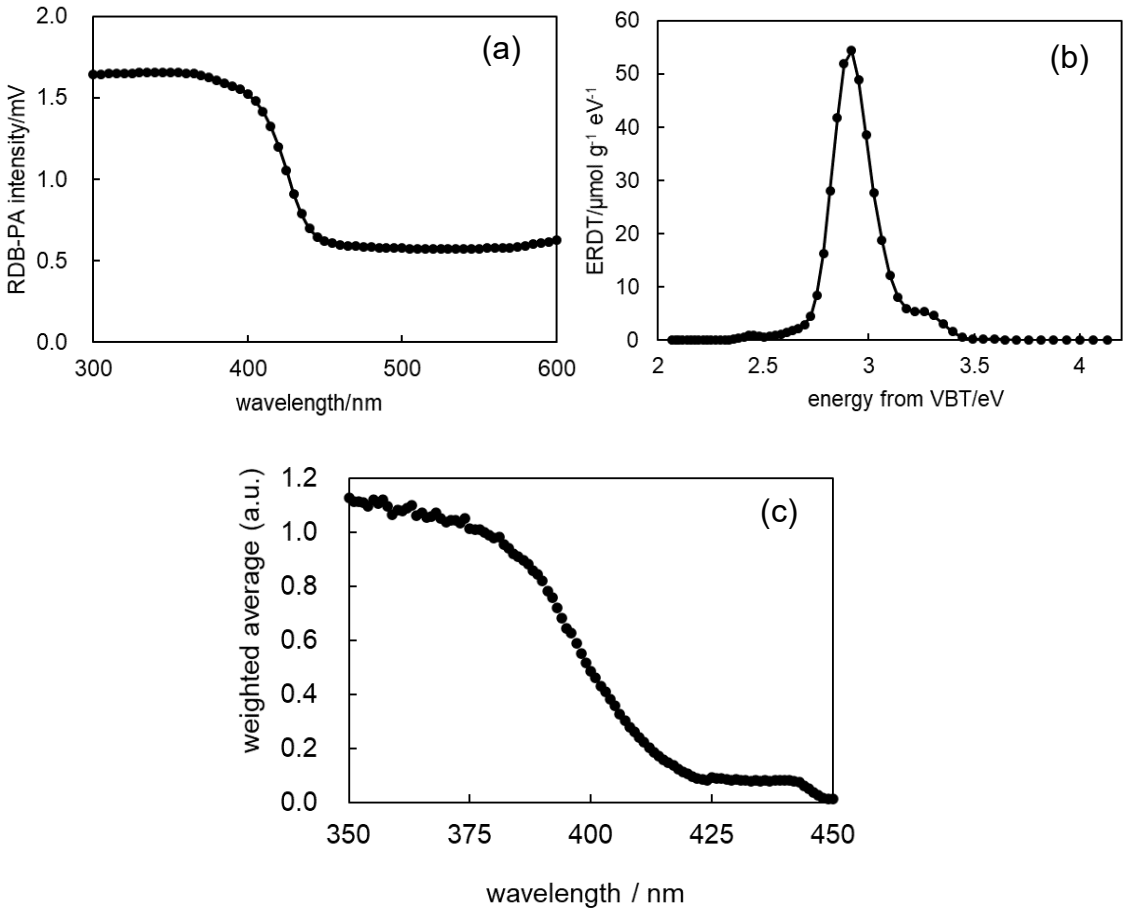

Figure 2-3 Representative (a) raw RDB-PA spectrum, (b) ERDT spectrum and (c) PA spectrum of ST-G1 (rutile titania, b0).

2.6 References

[1] Dutta, H.; Sahu, P.; Pradhan, S. K.; De, M. Microstructure Characterization of Polymorphic Transformed Ball-Milled Anatase TiO_2 by Rietveld Method, *Mater. Chem. Phys.* **2003**, *77* (1), 153–164.

[2] Šepelák, V.; Bégin-Colin, S.; Le Caër, G. Transformations in Oxides Induced by High-Energy Ball-Milling. *Dalton Trans.* **2012**, *41* (39), 11927.

[3] Bhattacharya, P.; Bellon, P.; Averback, R. S.; Hales, S. J., Nanocrystalline TiAl Powders Synthesized by High-energy Ball Milling: Effects of Milling Parameters on Yield and Contamination. *J. Alloys Compd.* **2004**, *368* (1-2), 187−196.

[4] Furlani, E.; Aneggi, E.; Leitenburg, C. D.; Maschio, S., High Energy Ball Milling of Titania and Titania–ceria Powder Mixtures. *Powder Technol.* **2014**, *254*, 591−596.

[5] Kibasomba, P. M.; Dhlamini, S.; Maaza, M.; Liu, C.-P.; Rashad, M. M.; Rayan, D. A.; Mwakikunga, B. W. Strain and Grain Size of TiO2 Nanoparticles from TEM, Raman Spectroscopy and XRD: The Revisiting of the Williamson-Hall Plot Method. *Results Phys.* **2018**, *9*, 628–635.

[6] Z. Wei, E. Kowalska, B. Ohtani, B. *Molecules*. **2014**, *19*, 19573–19587.

Chapter 3

Changes in Surface/Bulk Structure and Photocatalytic Activity by Braying and Post-calcination of Rutile-Based Titania Samples

In this chapter, a rutile sample, ST-G1 titania, was used as a starting material for braying and post-calcination treatments.

3.1 Photocatalytic Activity of Brayed and Post-calcined Rutile Samples

Figure 3-1 shows photocatalytic activities of original (b0), brayed (bX) and post-calcined (bXc) samples. For all the systems, braying and post calcination significantly changed the photocatalytic activities of the rutile titania sample under UV irradiation. The rate of product liberation, that is photocatalytic activity, was decreased less than half by only one-day braying, especially for H_2 system, it was one eighth. The extent of deactivation of the photocatalytic activity was much higher in H_2 system compared to CO_2 system and/or O_2 system; negligible H_2 activity was detected for the samples brayed for > 3 d. In the H_2 system (and O_2 system), platinum (and silver) was in-situ deposited as catalysts and those depositions could be also influenced by braying, but it might be true that intrinsic activity of titania was decreased. Thus, it is obvious that braying changed the structure of surface and/or bulk to result in the deactivations of the rutile samples.

Another feature is the partial recovery of activity by post calcination especially in the case of CO_2 system as bXc plots are higher than bX plots in almost all the cases. Another important feature is the presence of outliers. For example, two-day and nine-day brayed samples seemed to be deviated results. This shows the heterogeneity of braying partly because those brayed samples were prepared independently, but not successive processes. Thus, it should be noted that the structures might not be changed smoothly. Judging from the low reproducibility of activity results, two and nine day-brayed samples might be outliers.

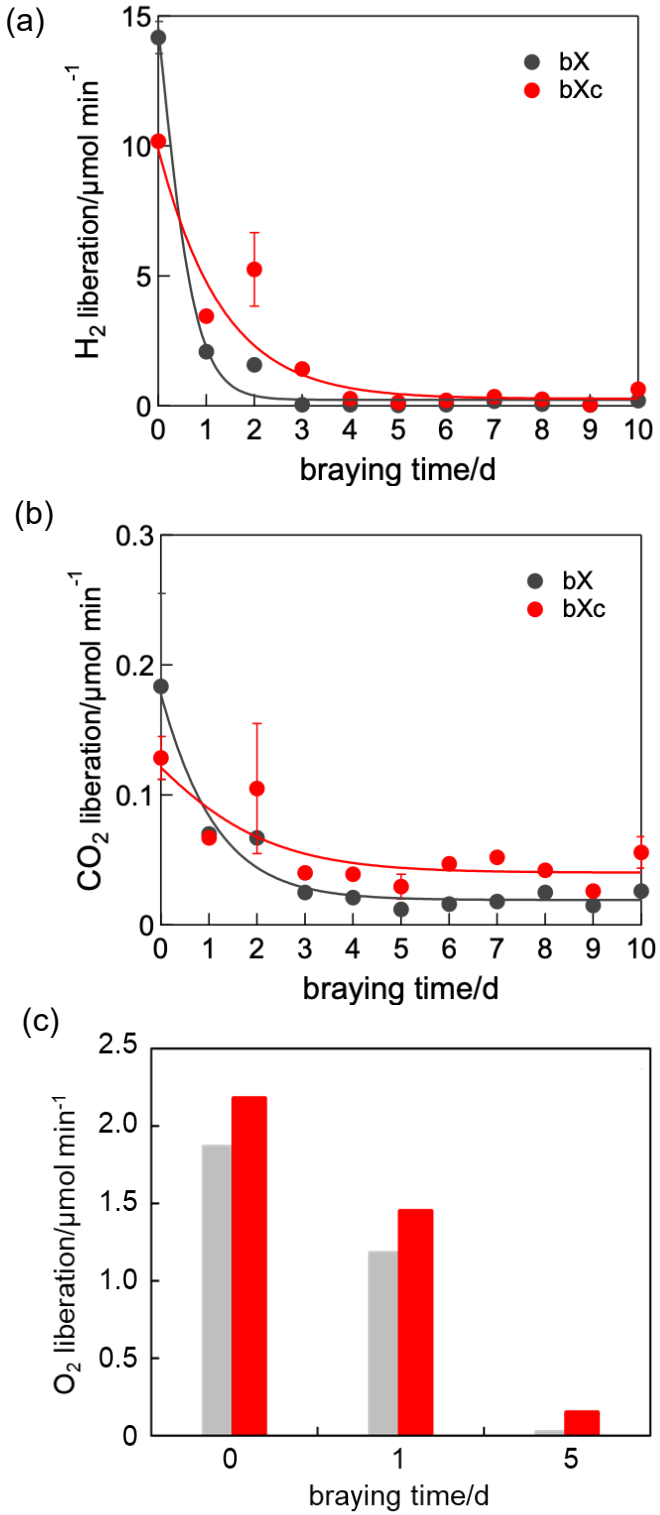

Figure 3-1 Photocatalytic activities of (black) original rutile, brayed and (red) post-calcined samples in (a) H_2 system (b) CO_2 system and (c) O_2 system.

3.2 Conventional Analyses of Brayed and Post-calcined Rutile Samples

3.2.1 Sample Colors and Diffuse Reflectance Spectra of Samples

Braying of the sample in an agate mortar caused changes in color of the samples, i.e., the original white color was changed to slightly yellowish light gray, then slight yellow color remained after 773-K calcination as shown in **Figure 3-2**.

Figure 3-3 shows DRS of the representative samples. Above mentioned sample color, i.e., slightly yellowish, except for the original (b0) sample was owing to blue-color absorption at ca. 420–520 nm. On the other hand, grayish color of the brayed samples might be caused by absorption shift at the wavelength > 500 nm, probably due to electron-filling of ETs (reduction), which is reported previously, and these electrons were removed by calcination in air (oxidation).

Above mentioned changes in color and absorption suggest some changes in structure/morphology of the surface affecting reflection.

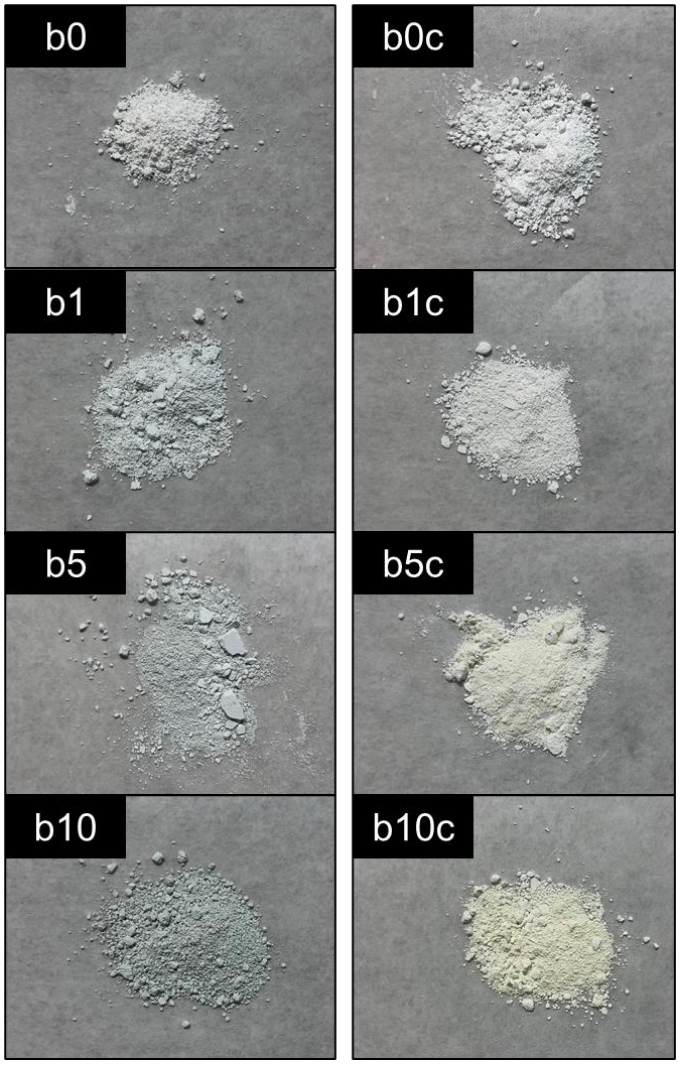

Figure 3-2 Color changes of original (b0), brayed (bX) and post-calcined (bXc) samples.

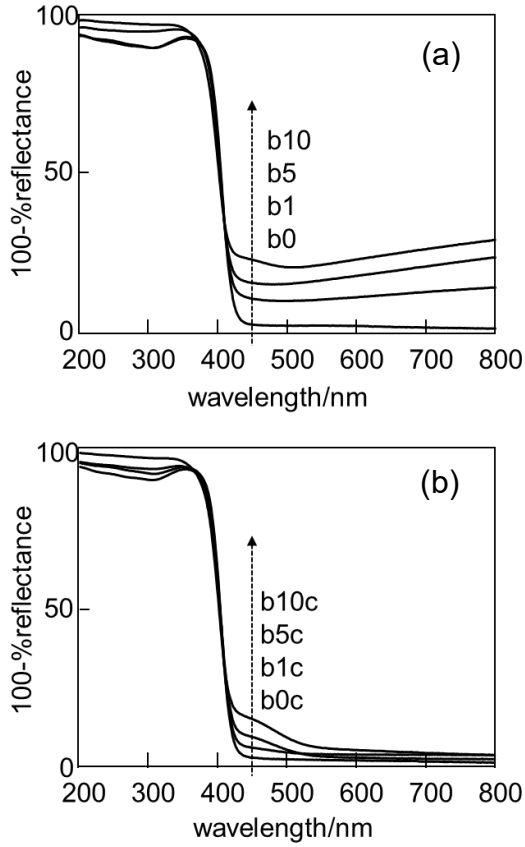

Figure 3-3 Diffuse reflectance spectra of (a) original (b0), brayed (bX) and (b) post-calcined (bXc) samples.

3.2.2 Morphology of Samples

Figure 3-4 shows scanning electron microscopic (SEM) images of the representative samples. It was obvious that there were negligible changes in size (ca. 100–200 nm) and morphology (spherical/oval) of the particles by braying for < 10 d regardless with or without post calcination. On the other hand, braying for 10 d induced appearance of small (< 100 nm) particle, suggesting the decomposition of original rutile particles into several pieces. The ratio of ca. 5 between SSA of the samples brayed for < 9 d and that of samples brayed for 10 d suggested that the particle size was reduced to one fifth on the assumption of constant density of particles. It should be noted that there was a limitation on sampling, taking images and checking the size and morphology, therefore, it was rather challenging to say the above-mentioned change (or no change) occurred comprehensively in the samples.

Figure 3-5 shows SSA of original (b0), brayed (bX) and post-calcined (bXc) samples. The SSA were almost constant (ca. 10–12 $m^2 g^{-1}$) for the samples brayed < 10d, while it increased drastically from 12 to 55 $m^2 g^{-1}$ for the 10-d brayed sample. The results suggested negligible changes in particle outer size and porosity of the samples brayed up to 9 d regardless with or without post calcination, and some changes appeared for the samples brayed for 10 d. However, I could not determine what kind of changes there appeared only from the results of the SSA, although we can imagine the sample particles

were broken into some pieces by combining results of the SEM images.

Anyway, above mentioned results suggest that post-calcination did not give any changes in particle outer size and morphology up to 9-d braying, and longer braying induced particle decomposition.

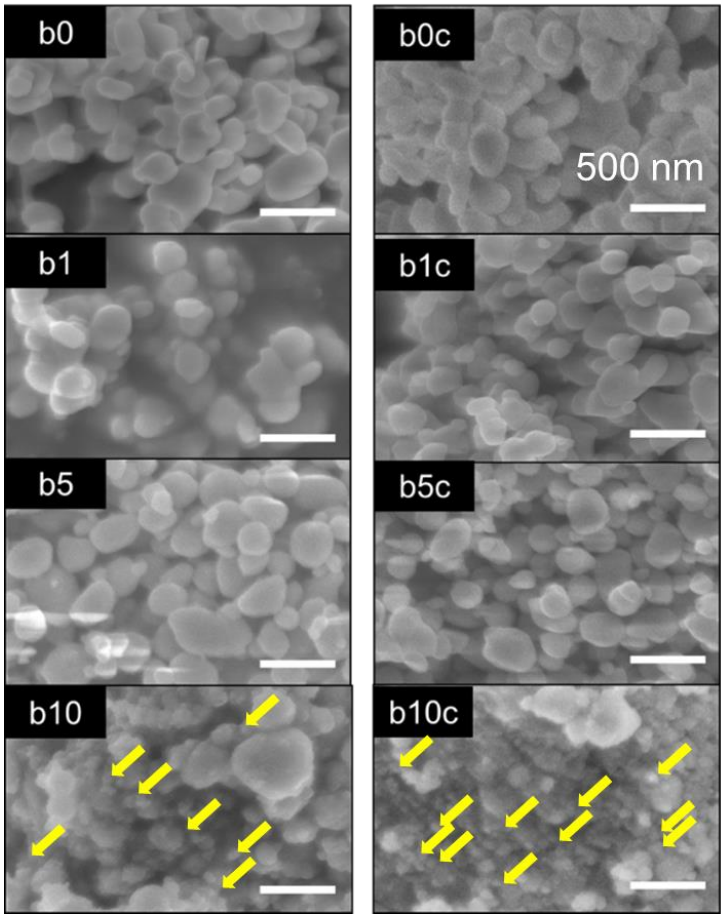

Figure 3-4 SEM images of original (b0), brayed (bX) and post-calcined (bXc) samples.

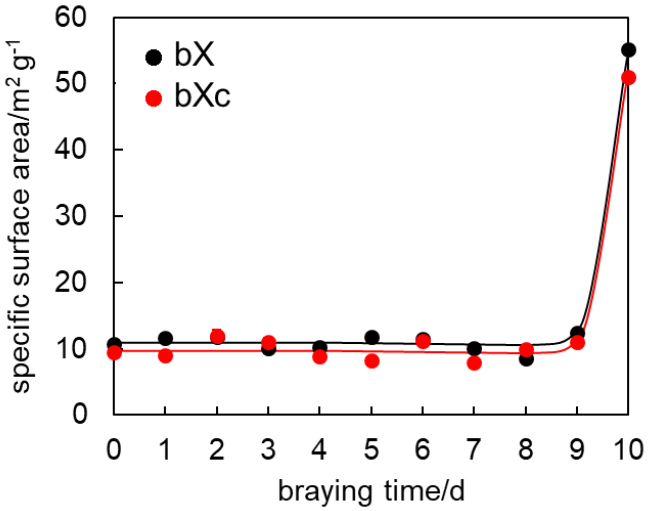

Figure 3-5 Specific surface area of (black) original rutile, brayed and (red) post-calcined samples as a function of braying time.

3.2.3 X-Ray Diffraction Patterns of Samples

XRD patterns of the representative samples are shown in **Figure 3-6**. The shapes of the diffraction peaks were almost no change by 1-d braying, but they were gradually smaller and the peak width became broader by braying for >1 d regardless with and without post-calcination, suggesting crystallite sized was decreased. No new crystalline peaks appeared by braying and post calcination. Then, crystalline content, size and lattice strain of each sample were quantitatively analyzed.

Rietveld analyses of the XRD patterns of the samples mixed with nickel(II) oxide as an internal standard revealed the change in their composition by braying and post-calcination as shown in **Figure 3-7**. Non-crystalline (NC) component for b0 sample calculated as the rest of crystalline (rutile) component was ca. 14% and this NC content was not changed by 773-K calcination (b0c). This suggested that the NC component included in b0 sample was originate from not amorphous titania, which could be crystallized to rutile by calcination. One of possible NC components is impurity such as water. It has been reported that the surface of titania is covered with multilayers of water adsorbed from air. [1] In addition, another possible component is amorphous titania sandwiched between rutile crystallites, i.e., grain boundary, which cannot be crystallized even by calcination 773 K. Braying lead to decrease and increase in the composition of rutile and NC, respectively, and the post calcination could recover this braying-induced composition change almost completely for the samples brayed for < 5 d. This braying-induced NC component might be amorphous titania transformed from rutile and was recovered by post calcination.

Figure 3-8 shows rutile crystallite size and lattice strain of the samples estimated via Halder-Wagner equation. Rutile crystallite size for b0 sample was ca. 60 nm (b0), and it was not changed by calcination(b0c). The crystallite size was decreased by braying and recovered more than 90% by post calcination for the samples brayed for < 5 d. The point is that the rutile composition was recovered (or slightly increased) by post calcination as described above (**Figure 3-7**), however, the rutile crystallite size was not completely recovered. This suggested that parts of the rutile crystallites (Most probable parts should be the surface of the sample particle because braying force was applied to the particle surface.) were amorphized by braying and this braying-induced amorphous titania was recovered partially by post calcination if the braying time was shorter than 5 d, but not completely recovered to the original single-crystallites. The longer braying might give unrecoverable damage to rutile crystalline lattice, e.g., thicker amorphous layer on the surface of the particle, and ten-day braying decomposed the particles into small pieces. Since the distances between titanium and oxygen for rutile crystalline and amorphous titania must be different (that of rutile is the shortest for all the titania polymorphs), there must be lattice mismatch at the interface between rutile core crystalline and amorphous surface layer when amorphous titania was created on the surface of rutile crystalline. Since recrystallization must proceed from the outermost parts of the amorphous layer as the calcination was applied from the outer side of the particle, part of the amorphized surface layer could not be recrystallized conformably with the core rutile due to the lattice

mismatch to result in independent small crystallites and amorphous layers at the interface, i.e., grain boundary, might remain between crystallites when the amorphous layer was thick enough. Lattice strain estimated by considering the broadening of the XRD peaks was also shown in **Figure 3-8**. The lattice strain was small, which may contain large error, and slightly increased with braying time. This supported the above-mentioned hypothesis that calcination of brayed sample may produce grain boundary (or lattice mismatch parts) and amorphous parts connecting to rutile crystallites produced lattice strain in these connecting rutile crystallites.

Since it has been reported that amorphous titania is totally inactive for photocatalytic activity [2], amorphous layer formed by braying and grain boundaries formed by post calcination may reduce the photocatalytic activity. An intrinsic problem is that both amorphous phases and grain boundaries could not be measured directly by the above-mentioned conventional analytical techniques, so the above-mentioned hypothesis should be remained as a speculation.

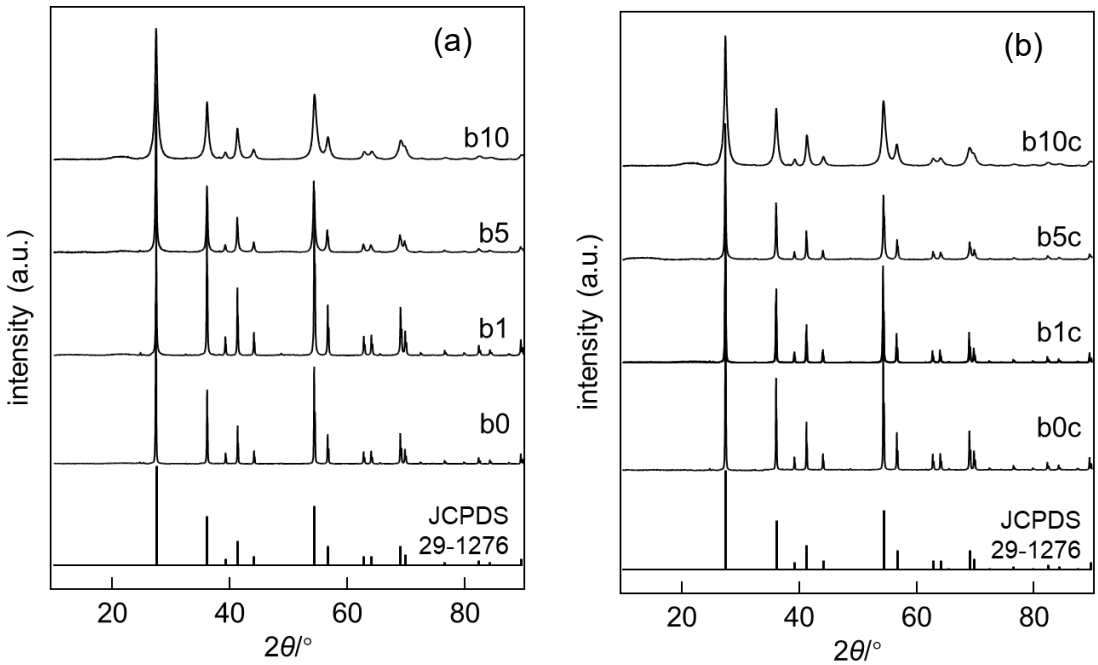

Figure 3-6 X-ray diffraction patterns of (a) original rutile, brayed and (b) post-calcined samples and that of pure rutile (JCPDS No. 29-1276).

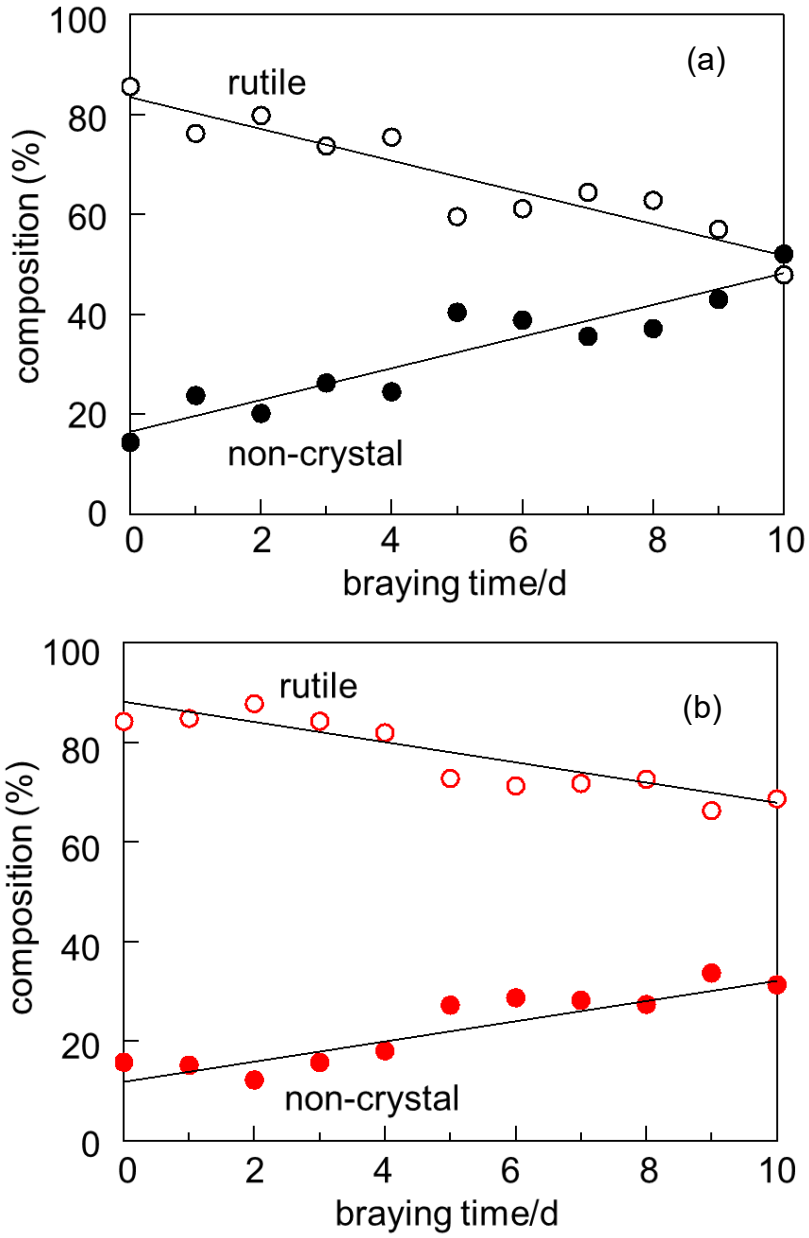

Figure 3-7 Crystalline (rutile; open circles) and non-crystalline (closed circles) composition of (a) brayed and (b) post-calcined samples as a function of braying time.

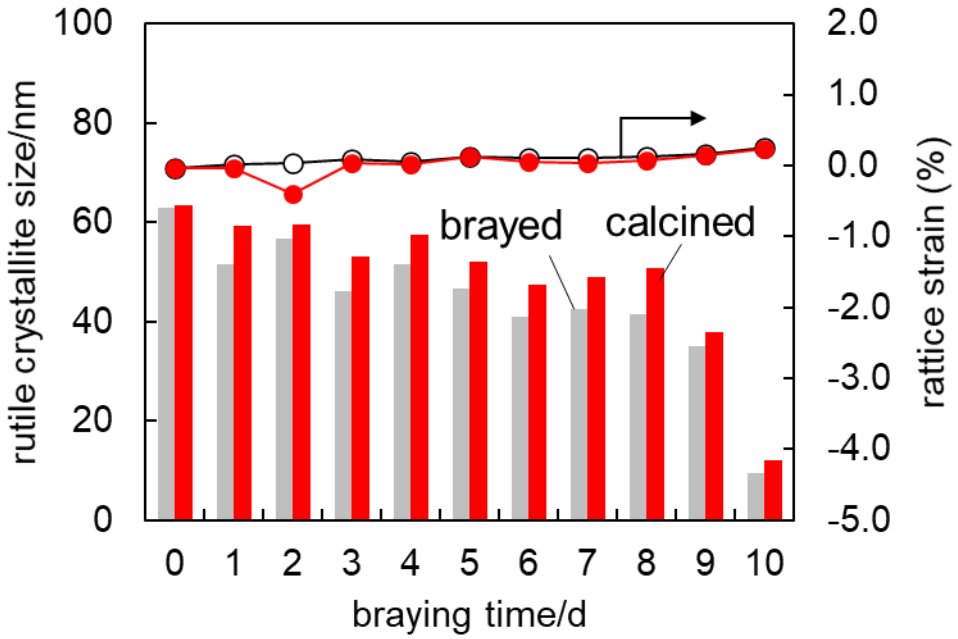

Figure 3-8 Rutile crystallite size (bars for left axis) and lattice strain (closed circles for right axis) of (gray) brayed and (red) post-calcined samples as a function of braying time.

3.3 ERDT/CBB Analyses of Samples

3.3.1 ERDT/CBB Patterns of Samples

Figure 3-9 shows ERDT/CBB patterns of original (b0), brayed (bX) and post-calcined (bXc) samples. As mentioned before, ERDT pattern shape, CBB and D_{ET} predominantly reflect surface structure, bulk structure and bulk/surface size, respectively. The energy of ETs is described in reference to VBT for convenience, because no other reference energy is available in RDB-PAS measurement, while actual photoexcitation might occur from relatively high density of states in VB (h-DOS VB), not from VBT, since DOS at VBT is negligible. At present, the energy difference from VBT and h-DOS VB cannot be determined experimentally, and this is one of the possible reasons why parts of ETs have been observed at the energy higher than CBB as shown in **Figure 3-9**.

CBB positions were almost same for all the samples indicating no change in bulk crystalline structure of the sample by braying and post calcination as CBB position corresponds to bandgap of the sample, similar results were obtained from the XRD results (section 3.2.3).

For the values of D_{ET}, brayed samples as well as shorter time (< 3 d) brayed-calcined samples showed almost constant, suggesting no significant change in their particle size except for b10. On the other hand, if brayed for >3 d, the total density was increased by post calcination, suggesting that the creation of new peaks other than the original rutile peak and the density of those new components were increased by post calcination, considered from the results of SSA as shown in **Figure 3-5**, that is, SSA of the samples

brayed for <10 d were almost no change regardless with and without post calcination. Moreover, obvious increase in D_{ET} was observed when longer time (> 2 d) brayed samples were calcined, which is discussed later. Thus, bulk crystalline structure and particle size (not crystallite size) were less changed by braying and post-calcination.

For the ERDT patterns shapes, the peak positions of ERDT patterns for the brayed and post-calcined samples were obviously different from those of b0 and b0c. The similar tendency was also observed in the results of photocatalytic activity as shown in **Figure 3-1**. This may indicate that the surface structure of brayed and calcined samples accounts for the markedly reduced photocatalytic activities. The ERDT peaks of b0 and b0c located at ca. 2.8 eV might correspond to rutile crystalline, since similar ERDT peaks have been observed for commercial rutile samples. Braying caused peak shift of the rutile peak to higher energy side with a tailing located at ca. 3.2–3.4 eV. It seemed that the longer the braying was performed, the larger the peak-shift became. In addition, as clearly shown in **Figure 3-10**(a), higher-energy peaks located > ca. 3.4 eV, in the position similar to the commercial amorphous sample, appeared for the samples brayed for > 2 d and was decreased (or even disappeared) by post calcination, suggesting the surface amorphization by braying and recrystallization by post calcination. Moreover, the main peaks appearing at approximately 3.0 eV was slightly upward shifted compared with b0 and b0c. To clarify these changes, subtraction of ERDT patterns of bX from bXc was performed as shown in **Figure 3-10**(b). First of all, newly appeared higher-energy peaks located > ca. 3.4 eV were decreased by calcination as negative patterns were observed at that energy range, representing amorphization by braying and recrystallization by post calcination. It should be noted that these amorphous peaks did not appear in short-time brayed samples. For b0c, b1c and b10 samples, a slightly higher energy peak located at ca.3.0–3.4 eV was decreased and a peak slightly higher than that of rutile, position of which was located at 2.8 eV (dotted line in **Figure 3-10**(b)), was increased, suggesting something was recrystallized into rutile upon calcination. So, by post calcination, new peaks located at 2.6–3.2 eV, which is not attributable to rutile, appeared. Those features could be explained by assuming two-kinds of amorphous components as discussed in the following section.

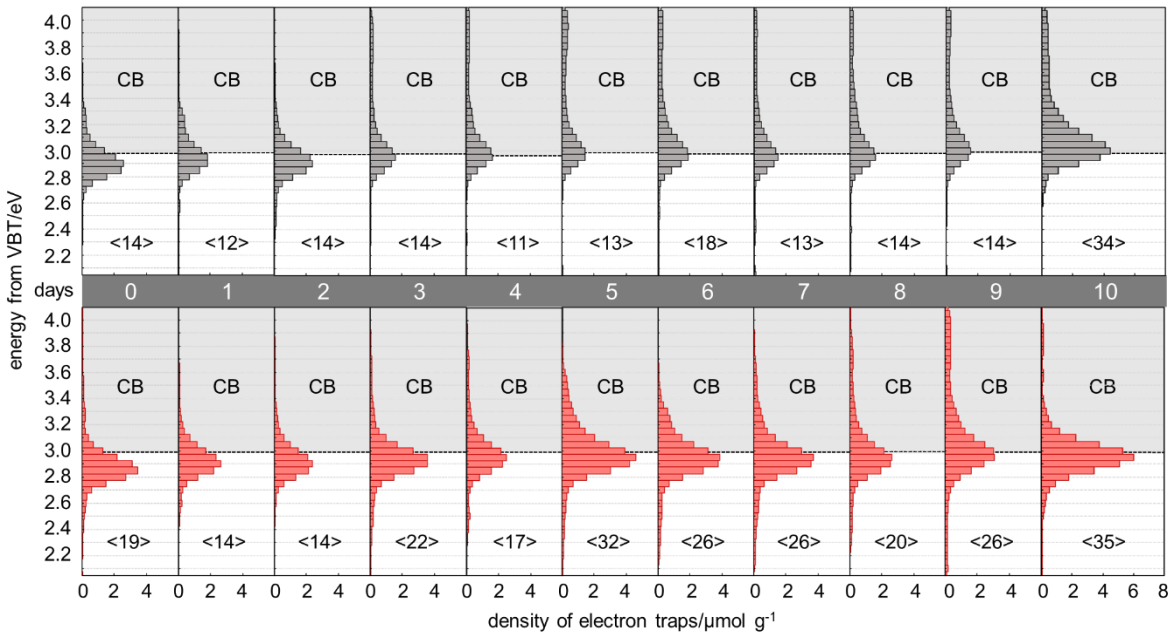

Figure 3-9 ERDT/CBB patterns of (upper) original, brayed and (lower) post-calcined samples. Doted lines indicate conduction band-bottom position and figures in < > denote total density of electron traps.

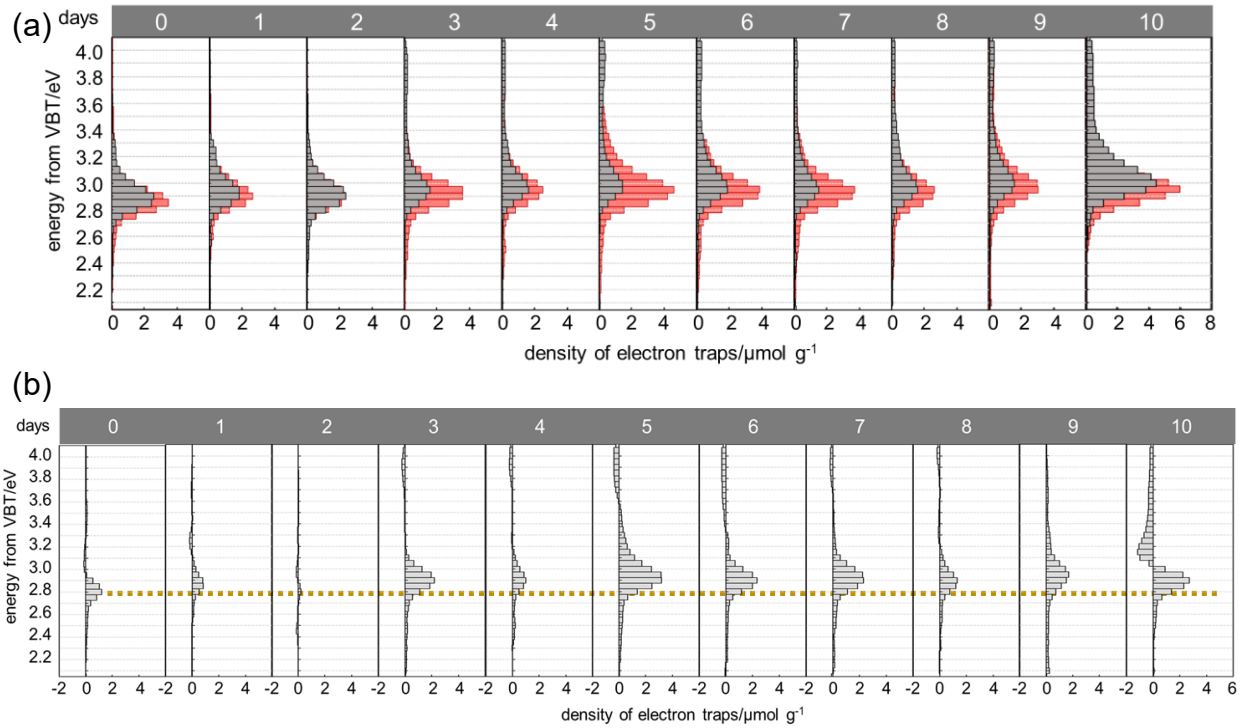

Figure 3-10 (a) Overlapping ERDT patterns of (black) original, brayed and (red) post-calcined samples and (b) subtracted ERDT patterns of post-calcined samples from original and brayed samples. Peaks of electron traps in negative and positive value indicate decrease and increase by post calcination, respectively. Dotted line indicates the peak position of b0 sample.

3.3.2 *Simulation of ERDT Patterns and Interparticle Charge-Transfer Excitation between Rutile and Amorphous Titania*

ERDT patterns of rutile (b0), commercial amorphous titania (AMO) and their 50/50 weight ratio mixture sample, which was prepared by braying manually in an agate mortar for 10 min, are shown in **Figure 3-11**. AMO has a broad (ca. 2.9–4.0 eV) ERDT pattern with a peak at ca. 3.4 eV, which is higher than those of other crystalline titania, especially, ca. 0.5 eV higher than that of rutile included in b0 sample. An ERDT pattern of a 50/50 mixture of the AMO with b0 showed a peak ca. 0.05-eV upward shifted from the ERDT peak of b0 with higher energy-side tailing. Although the energy of ERDT patterns is shown in reference to VBT for convenience, actual photoexcitation might occur from h-DOS VB, as described above. If the energy of h-DOS VB of b0 and AMO are the same, the ERDT pattern of the 50/50 mixture of these two samples should be reproduced by a simple summation of two ERDT patterns as shown in SIM 0.00. However, the real pattern of 50/50 mixture was completely different from SIM 0.00 giving 0.15 of ζ_S and the real peak position was at ca. 2.9 eV, which was slightly higher than that of b0 and ca. 0.5 eV downward shifted compared with the peak position of SIM0.00. Therefore, it can be said that those energy of h-DOS VB positions are different. It should be noted that the peak position and the peak shape of the 50/50 mixture were quite similar to those of brayed and post-calcined samples as shown in **Figure 3-9**. In addition, the value of D_{ET} for 50/50 mixture sample was approximately an average of rutile b0 and AMO, indicating all the ETs in two components were detected.

In order to try to reproduce ERDT pattern of a 50/50 mixture, simulation was performed (SIM). **Figure 3-12** shows the procedure of the simulation in the case of 50/50 mixture of rutile b0 and AMO with 0.20-eV energy shift, which was coded as "SIM0.20". The simulated ERDT patterns was obtained by summation of 50% ERDT pattern of b0 with that of AMO, which was shifted toward a lower energy with 0.20 eV. Thus, obtained simulated ERDT patterns with different shift energy (0.00–0.55 eV) for 50/50 mixture are shown in **Figure 3-13**(a). The peak positions of the simulated patterns were shifted downward by increasing with shift energy and the shapes of the ERDT patterns were also changed by shift energy. The value of ζ_S was increased with shift energy and showed highest when shift energy was 0.47 eV as shown in **Figure 3-13**(b). Checking the peak position of the simulated patterns and that of 50/50 mixture, a simulated pattern obtained with 0.47-eV energy shift showed the same peak position. This suggests that h-DOS VB of AMO is located ca. 0.47 eV lower than that of rutile b0. However, the value of ζ_S was 0.58, which is slightly low. One possible reason for the lower ζ_S is lower heterogeneous contact degree, i.e., not all the particles of b0 and AMO contact sufficiently each other, as reported previously. [3] If this is true, smaller proportion of AMO would give higher ζ_S since SSA of AMO is larger than b0, i.e., particle size of AMO is smaller than that of b0. However, the result was opposite; ζ_S became slightly higher (0.63) in the case of 30/70 mixture (30% for b0 and 70% for AMO) as shown in **Figure 3-13**(c). This fact suggests that the reason of lower ζ_S might be originated from other aspect; broadness of ERDT

pattern for 50/50 mixture was narrower compared with simulated ERDT patterns.

Above mentioned a shift of amorphous-peak position and difference in the ERDT pattern broadness (width) of the mixture sample and simulated sample can be reasonably interpreted by assuming interparticle charge-transfer excitation, ICTE, for a mixture of a higher h-DOS-VB sample (H-sample) and a lower h-DOS-VB sample (L-sample). For rutile and amorphous mixtures, ICTE can be explained by schematic images shown in **Figure 3-14**. It is assumed that h-DOS of rutile b0 is located 0.47-eV higher than that of amorphous titania according to the results of simulation as shown in **Figure 3-13**, and photoexcitation occurred from these h-DOS VB. If those particles are placed separately in the PAS cell or those ERDT patterns are measured independently, the energy in ERDT patterns are shown in reference to each h-DOS energy, of course, as shown in **Figure 3-14**(a). If these two kinds of titania particles are contacted electronically (**Figure 3-14**(b)), on the other hand, it is expected that ETs in both particles are electron-filled by excitation from h-DOS of rutile, because wavelength of excitation light is scanned from longer wavelength, i.e., lower energy. ETs in amorphous titania have been already filled by ICTE when the excitation-light wavelength becomes corresponding to VB-ET excitation energy for amorphous titania. As a result, the peak position of amorphous titania in ERDT pattern of the mixture is 0.47 eV-downward shifted if ICTE happens, while that of rutile is not changed. It should be noted that the energy distribution of VB may give influence on ERDT pattern width, i.e., energy distribution of VB in amorphous titania might be broader compared with that of rutile resulting in broader ERDT pattern of amorphous titania, since the simulated patterns showed broader peaks while ERDT pattern of mixture showed narrower ERDT pattern. When ICTE happens, the ERDT pattern of amorphous titania obtained by photoexcitation from h-DOS VB of rutile, energy distribution of VB in which might be steeper, might be narrower (yellow ERDT pattern in **Figure 3-14**(b)) and this ERDT pattern obtained by steeper h-DOS VB may show real ERDT pattern of amorphous titania.

Assuming the same surface structure (giving ETs) of the commercial amorphous titania and amorphous titania possibly included in the brayed samples, the similarity of ERDT shape between ERDT patterns of the brayed/post-calcined samples and that of 50/50 b0-amorphous mixture indicates that ICTE was happened in those brayed/post-calcined samples and the brayed/post-calcined samples brayed for < 3 d (Those ERDT patterns does not include higher-energy peaks located > ca. 3.4 eV.) are composed of thoroughly adjoined rutile and amorphous phases. On the other hand, those samples brayed for > 2 d are composed of partly adjoined rutile and amorphous phases. In other word, those samples are covered by amorphous phase being electronically contacted with core rutile crystallites in the case of shorter braying, but if braying time becomes longer and the thickness of amorphous layer become thick enough, parts of amorphous (most probably outermost amorphous) cannot contact core rutile.

Since simulation could not reproduce the ERDT pattern of mixture samples, deconvolution of ERDT pattern with Gaussian-curve fitting was performed in the next section.

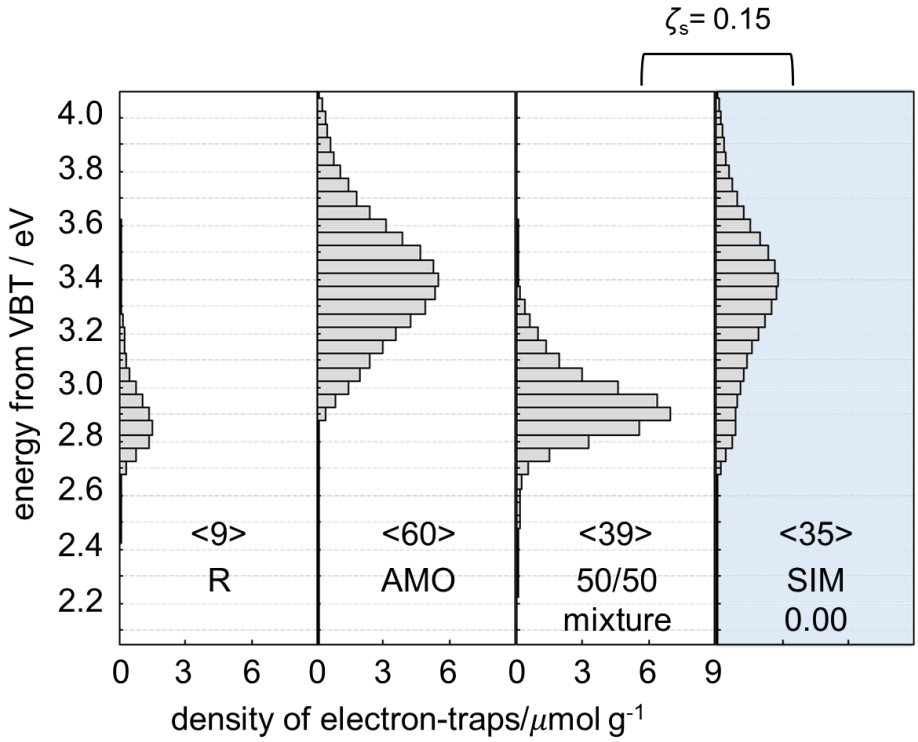

Figure 3-11 ERDT patterns of b0 (R), amorphous titania (AMO) and their 50/50 mixture. Also shown in blue background is summed ERDT patten with halved ERDT patterns of b0 and amorphous pattern without shift.

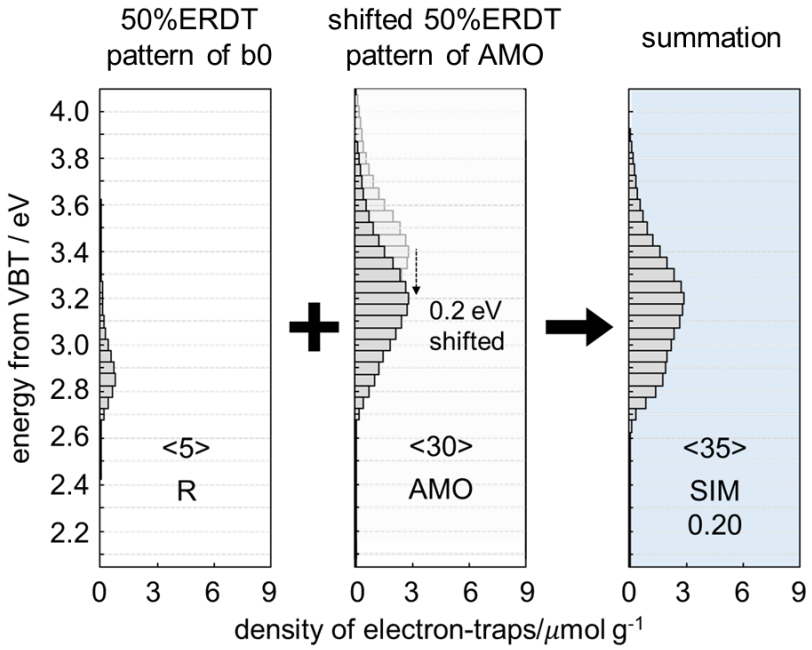

Figure 3-12 Procedure of simulation with 0.20-eV energy shift in the case of 50/50 mixture of rutile and amorphous titania.

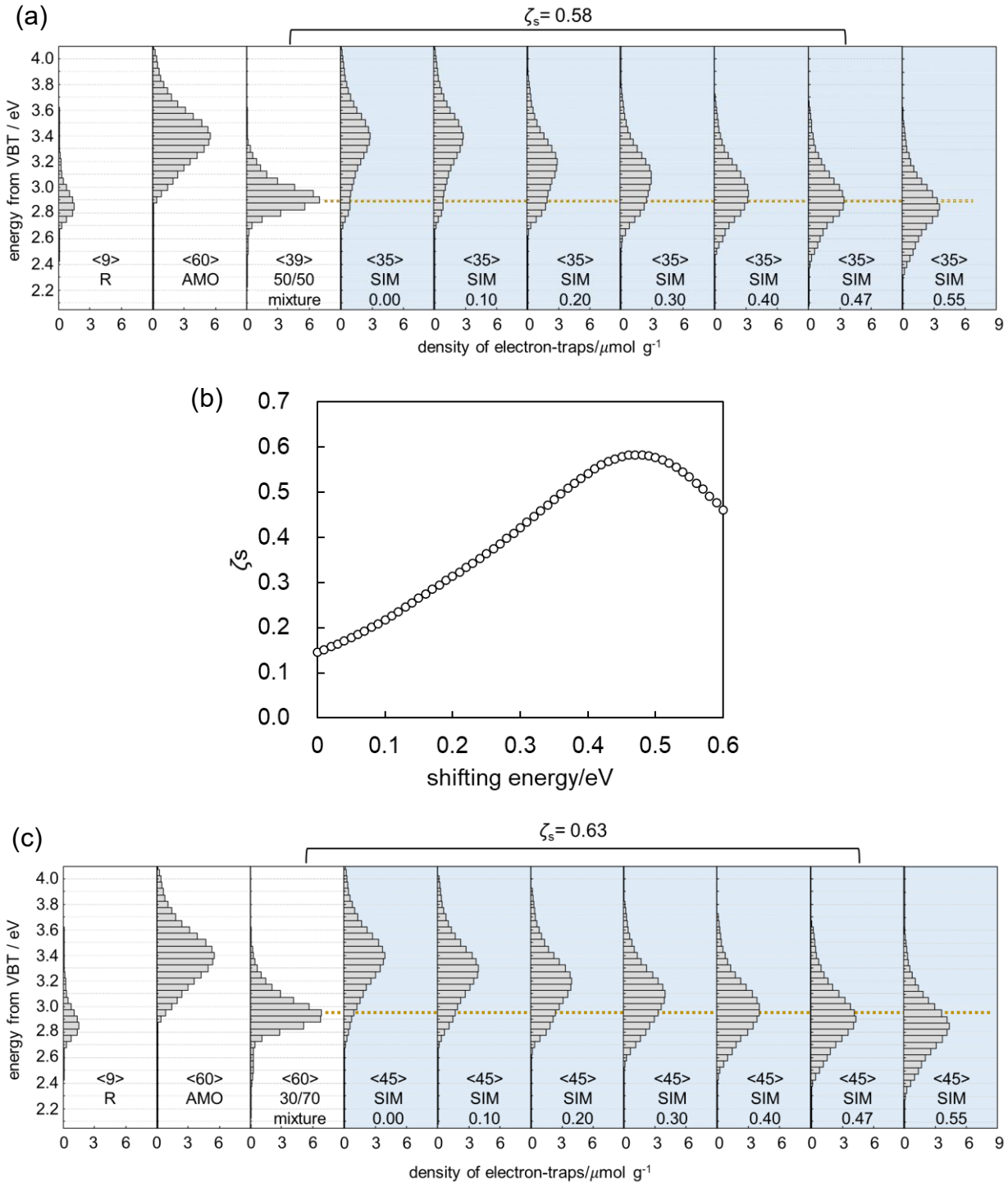

Figure 3-13 ERDT patterns of b0, amorphous titania and their 50/50 and 30/70 mixtures. Also shown in blue background are representative simulated ERDT patterns by summing up a pattern of 50% (30% in (c)) b0 with lower-energy shifted pattern of 50% (70% in (c)) amorphous. For example, code "SIM 0.20" shows summation of 50% (30% in (c)) b0 pattern and 0.20 eV downward shifted of 50% (70% in (c)) amorphous pattern. Dotted lines indicate the energy of the peak position in mixture samples. Also, (b) changes in similarity of ERDT shape (ζ_S) as a function of amount of energy shift in the case of 50/50 mixture.

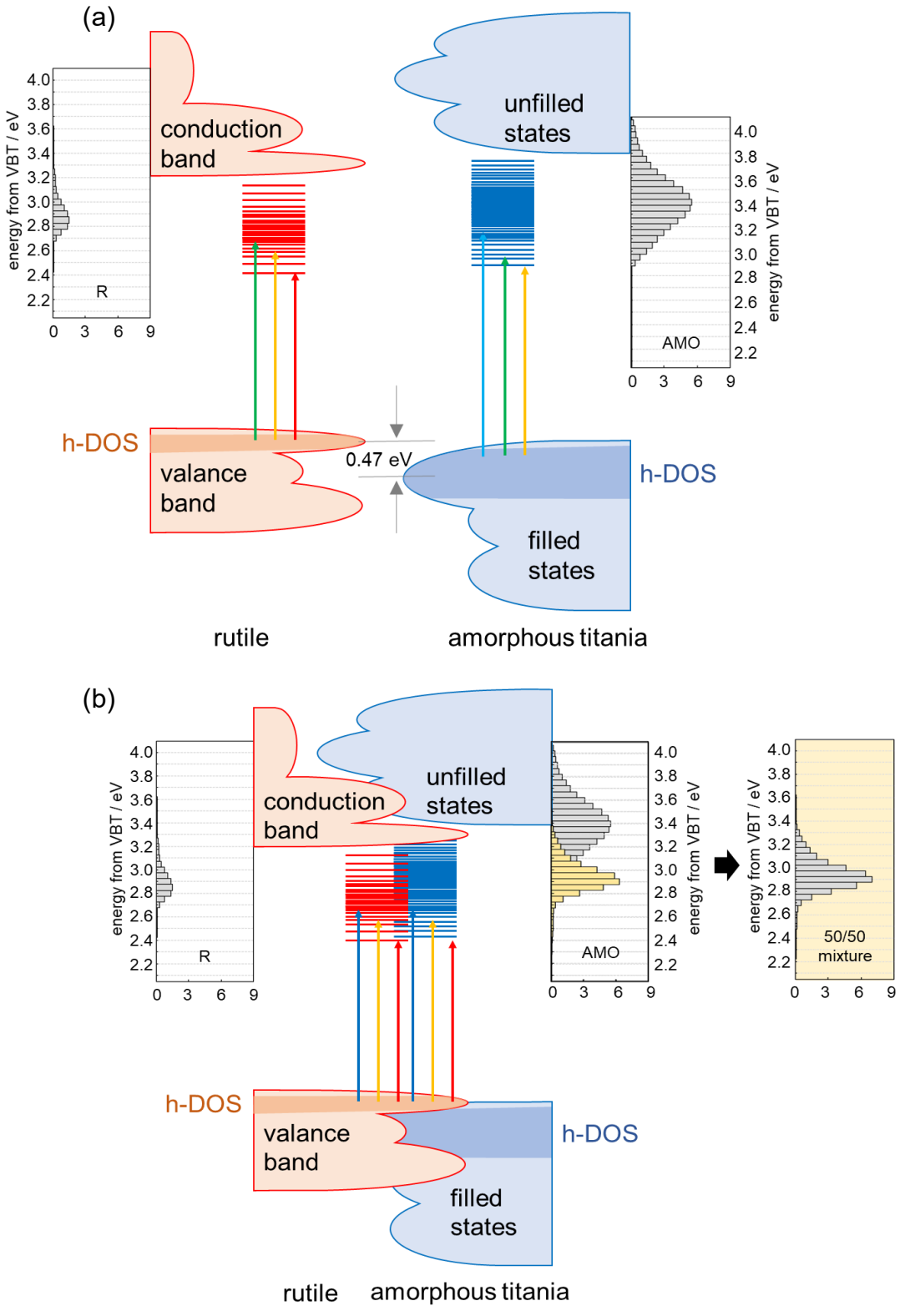

Figure 3-14 Interparticle charge-transfer excitation of rutile and amorphous titania. mixtures with (a) isolated and (b) contacted samples.

3.3.3 Deconvolution of ERDT Patterns with Gaussian-curve Fitting

As control experiments, deconvolution with Gaussian-curve fitting for the mixture samples with rutile b0 and AMO were performed. As shown in **Figure 3-15**, fitting curve (gray dashed line) are well matched with original ERDT pattern (thin black line, almost negligible due to well matching with fitting curve) of 50/50 and 30/70 mixture samples with Gaussian distribution. The actual ERDT pattern of b0 and AMO mixture in the ratio of 50/50 are reproduced by two peaks, the position of which are 2.92 eV and 3.0 eV. As similar peak has been observed in the case of only rutile b0 sample, the peak at 2.92 eV is ascribed to rutile crystalline (R). Another peak at 3.0 eV might be attributable to amorphous in contact with rutile (am-R) by assuming ICTE, the peak of which is downward shifted ca. 0.4 eV with respect to commercial amorphous titania (AMO). In the case of 30/70 ratio, the energy for those peak components were obtained as almost similar, i.e., 2.94 eV of R and 3.05 eV of am-R. Therefore, it can be said that two kinds of amorphous peaks, isolated amorphous (am) and amorphous contacted with rutile (am-R), are located at different energy. For the best fitting, narrowed simulated am-R peak was necessary, suggesting that the h-DOS of amorphous may have wider energy distribution compared with that of rutile.

Figure 3-16 shows representative results of Gaussian-curve fitting for rutile b0, brayed (bX) and post-calcined (bXc) samples and the results of peaks positions and peak width (FWHM) are summarized in **Table 3-1**. First of all, braying reduced the intensity of rutile peaks (R) and am-R peaks seemed increased with braying time, indicating surface of rutile particle was amorphized to give amorphous layer in contact with rutile (am-R). Then, isolated amorphous (am), not contact with rutile, appeared at the middle braying time (> 2 d) as a result of formation of thicker amorphous layer, since outer amorphous layer might not contact with core rutile completely. These "independent" (or detached) amorphous titania (am) seems to be crystallized, i.e., recovered, to rutile by post calcination, as high energy (> 3.5 eV) peaks were almost disappeared. One of the significant points is, amorphous in contact with rutile (am-R) was rather increased by calcination. This amorphous in contact with rutile remaining even after 773-K calcination might be grain boundary (am-R(GB)), one kind of amorphous titania, created by sandwiched with rutile crystallites as mentioned in section 3.2.3. Increase in D_{ET} for the post-calcined samples brayed for long time (> 2 d) is consistently interpreted by assuming larger amount of ET density in those grain boundaries, and the peak is located at the same position with that of amorphous. In this way, it was clarified that part of the peak located slightly higher energy (ca. 2.6–3.2 eV) than rutile, as pointed out in section 3.3.1, could be ascribed to grain boundary from the results of these peak fitting along with assuming ICTE. As a result, by using RDB-PAS analyses, at least three kinds of amorphous components: isolated one (am), in contact with rutile one (am-R) and one remained as grain boundary (am-R(GB)) could be identified.

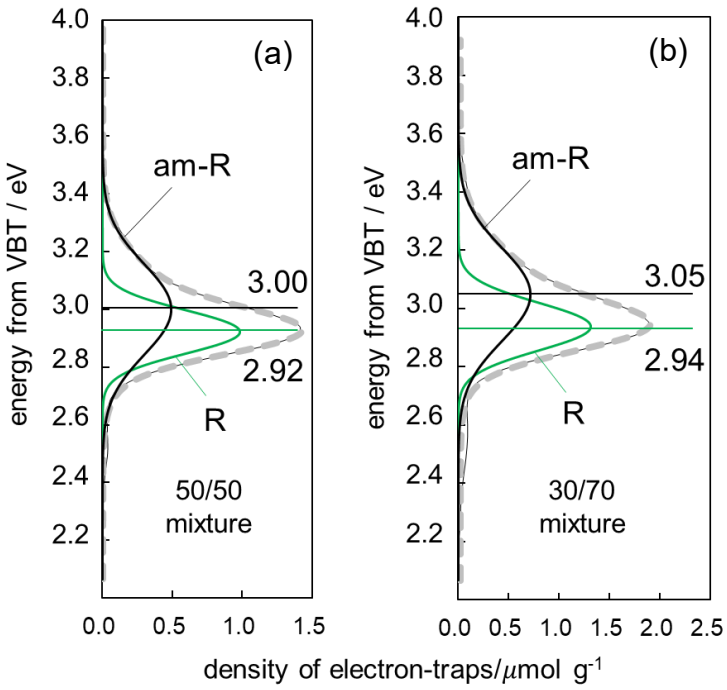

Figure 3-15 Deconvolution of ERDT patterns for mixture of rutile and amorphous titania in the ratio of (a) 50/50 and (b) 30/70 with Gaussian-curve fitting.

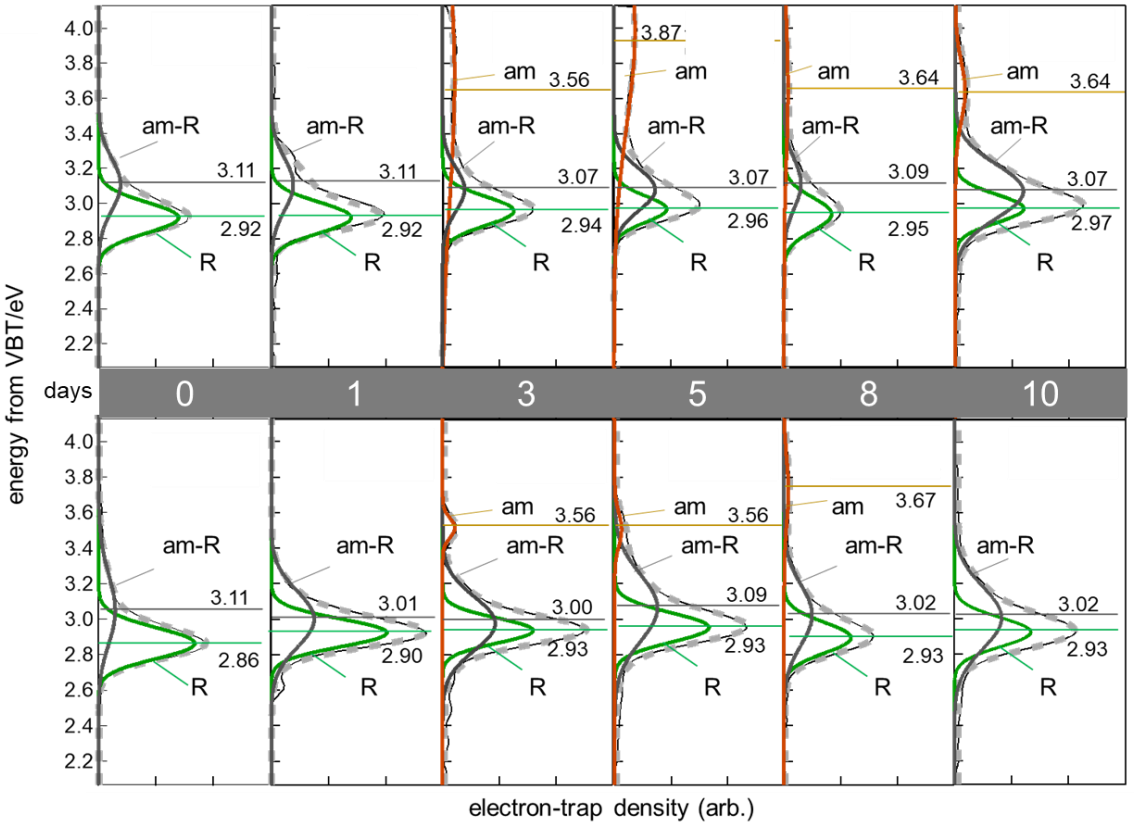

Figure 3-16 Representative deconvolution results of ERDT patterns for (upper) original (b0), brayed (bX) and (lower) post-calcined (bXc) samples.

Table 3-1 Summary of (a) peaks positions and (b) peak width (FWHM) in Gaussian-curve fitting.

(a)

code	peak position/eV		
	R	am-R	am
b0	2.92	3.11	-
b1	2.92	3.11	-
b3	2.94	3.07	3.56
b5	2.96	3.07	3.87
b8	2.95	3.09	3.64
b10	2.97	3.07	3.64

code	peak position/eV		
	R	am-R	am
b0c	2.86	3.11	-
b1c	2.90	3.01	-
b3c	2.93	3.00	3.56
b5c	2.93	3.09	3.56
b8c	2.93	3.07	3.67
b10c	2.93	3.02	-

(b)

code	FWHM/eV		
	R	am-R	am
b0	0.21	0.35	-
b1	0.19	0.31	-
b3	0.19	0.29	1.60
b5	0.18	0.28	1.28
b8	0.19	0.31	1.18
b10	0.19	0.31	1.06

code	FWHM/eV		
	R	am-R	am
b0c	0.20	0.42	-
b1c	0.18	0.37	-
b3c	0.17	0.36	0.13
b5c	0.19	0.44	0.22
b8c	0.20	0.44	0.39
b10c	0.19	0.41	-

3.3.4 *Schematic Image of Changes in Surface/Bulk Structures by Braying and Post-Calcination*

Figure 3-17 shows schematic image of changes in surface and bulk structures. Braying causes the surface amorphization to yield amorphous in contact with R (am-R) and post calcination partially recrystallizes into rutile (R). Longer-time braying thickens the thickness of the surface amorphous layer to result in the formation of isolated amorphous (am). Since post calcination of those samples recrystallizes from the outside of a particle and the position of amorphous component might be fixed in rutile particle, recrystallization must induce lattice mismatch to leave uncrystallized amorphous components, grain boundaries. Further long-time braying produces thicker amorphous layer to result in decomposition of particles into small pieces. Such a change is consistent with the drastic increase in the total density by 10-days braying. It should be noted that this model of structure changes can be elucidated only based on ERDT/CBB patterns, without any conventional analytical data such as SEM or XRD.

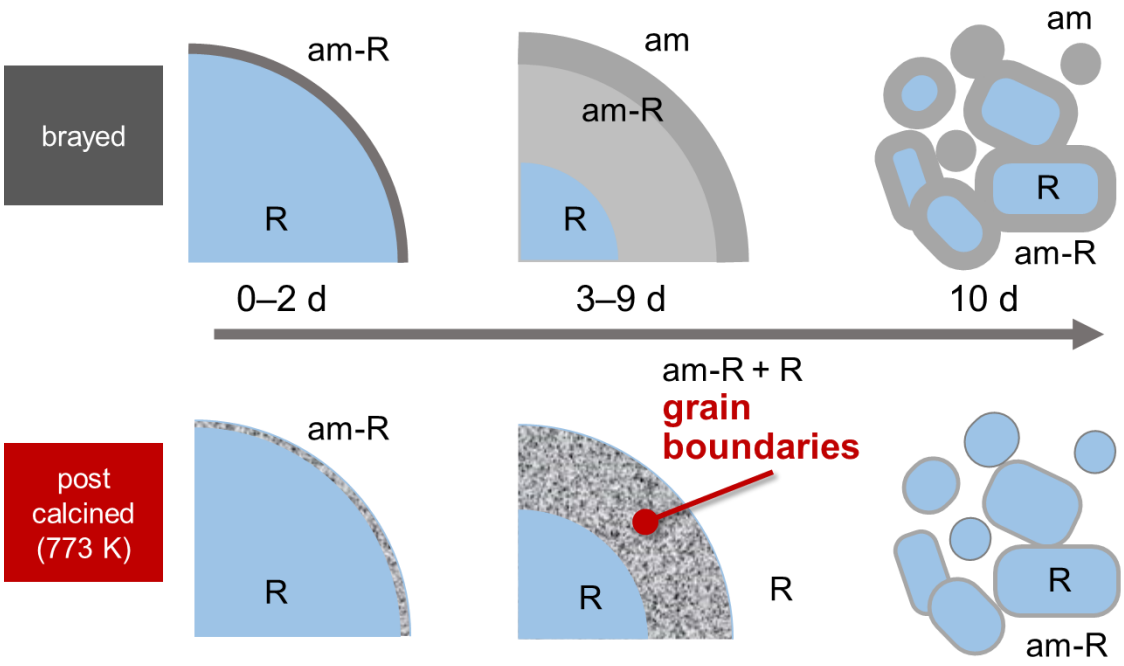

Figure 3-17 Schematic image of changes in surface and bulk structures of rutile sample by braying and post-calcination.

3.3.5 *Relation with Surface/bulk Structure and Photocatalytic Activity*

To describe relation with surface and bulk structures, i.e., three kinds of amorphous titania induced by braying and post-calcination, and photocatalytic activity, I display again **Figure 3-1** and **Figure 3-17** along with each reaction equations below, for convenience.

In both photocatalytic reaction systems, the activities were decreased by braying due to the decrease in active rutile content. As already mentioned before, amorphous titania is inactive, therefore, amorphous titania formed by braying (am/am-R) may act as an inert for those photocatalytic activity. However, this amorphous titania also can absorb light and the absorbing wavelength may be shorter than rutile crystalline due to amorphous. Therefore, this inactive amorphous titania is formed on the surface of rutile particle by braying, the amount of light reaching to rutile core may be reduced, which is so-called shading effect. On the other hand, grain boundaries formed by post calcination may reduce photocatalytic activity; even rutile generates electron-hole pair by absorbing light, the neighboring grain boundaries recombine those charge carriers before used for photocatalytic reaction, as reported many times. Comparing two reaction systems, it is possible to say the CO_2 system seems less sensitive to the grain boundaries to show appreciable activity recovery by calcination. That's because platinum deposits may be key factors for the activity in H_2 system and the deposition of platinum on the photocatalyst surfaces may be influenced by surface structure sensitively.

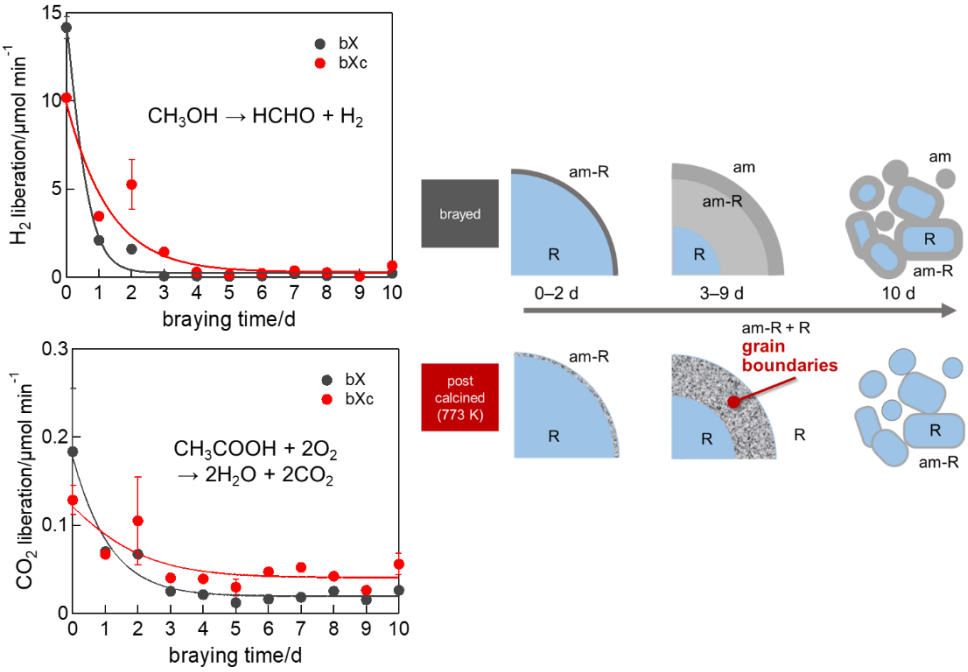

3.4 Conclusions

The structure and bulk changes by braying and post-calcination were examined by conventional analytical technics such as nitrogen adsorption and X-ray diffraction spectroscopy and reserved double-beam photoacoustic spectroscopy (RDB-PAS) developed by Ohtani laboratory. Those influences on three photocatalytic activities; hydrogen liberation from deaerated aqueous 50wt% methanol with chloroplatinic acid and carbon-dioxide liberation from aerobic aqueous 5vol% acetic acid as well as oxygen liberation from deaerated water with 0.05 mol L^{-1} sliver nitrate, were considered. It was found that the surface was amorphized by braying and recrystallized partly by post-calcination, then the rutile particle was decomposed into small pieces. Furthermore, RDB-PAS analyses revealed three kinds of amorphous formed by braying and post-calcination; amorphous in contact with core rutile, isolated amorphous and grain boundary, which gave decisive influence on photocatalytic activity of materials. Although both combined conventional analyses and RDB-PAS analysis provided a similar interpretation of change in the structure of rutile titania particles induced by braying and post calcination, direct evidence of the formation of the three kind of surface amorphous layer could be obtained only by ERDT/CBB patterns taken by RDB-PAS.

3.5 References

[1] A. Y. Nosaka, T. Fujiwara, H. Yagi, H. Akutsu, Y. Nosaka, *J. Phys. Chem. B* **2004**, *108*, 9121.

[2] B. Ohtani, Y. Ogawa, S. Nishimoto, *J. Phys. Chem. B* **1997**, *101*, 3746.

[3] Shen, Y.; Nitta, A.; Takashima, M.; Ohtani, B., Do particles interact electronically? —Proof of Interparticle Charge-Transfer Excitation between Adjoined Anatase and Rutile Particles, *Chem. Lett.*, **2021**, *50*, 80-83.

Chapter 4

Changes in Surface/Bulk Structure and Photocatalytic Activity by Braying and Post-calcination of Anatase-Based Titania Samples

In this chapter, an anatase-based sample, Merck titania, was used as a starting material for braying and post-calcination treatments. It should be noted that this anatase sample contains small amount of rutile originally as shown in **Table 2-1**.

4.1 Photocatalytic Activity of Brayed and Post-calcined Anatase Samples

Figure 4-1 shows photocatalytic activities of original (b0), brayed (bX) and post-calcined (bXc) samples. Braying and post calcination significantly changed the photocatalytic activities under UV irradiation also in the anatase case. The activity was drastically decreased by one fourth and halved of the original anatase sample in H_2 system and CO_2 system, respectively, only by one-day braying. Then, those activities were negligible for the sample brayed for > 2 d. However, the recovery of the activity by post calcination especially in the case of carbon-dioxide liberation was significant as shown in **Figure 4-1** (b). The activity was almost constant for the samples brayed for < 4 d and post calcined. Outliers were also seen in the anatase case; 3, 7- and 8-days brayed samples might be considered as outliers.

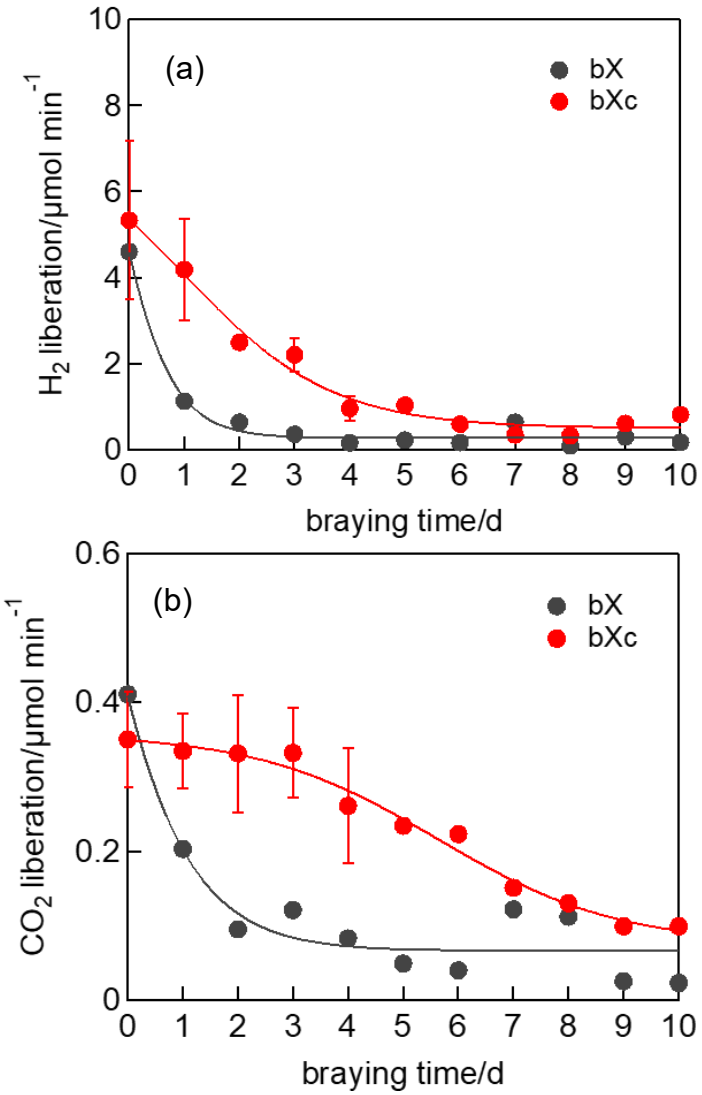

Figure 4-1 Photocatalytic activities of (black) original anatase, brayed and (red) post-calcined samples in (a) H_2 system and (b) CO_2 system.

4.2 Conventional Analyses of Brayed and Post-calcined Anatase Samples

4.2.1 Sample Colors and Diffuse Reflectance Spectra of Samples

Braying of the sample caused changes in color of the samples also in the anatase case, i.e., the white color was changed to slightly yellow-light gray, then slight yellow color remained after 773-K calcination as shown in **Figure 4-2**.

Figure 4-3 shows DRS of the representative samples. The yellowish sample color was owing to blue-color absorption at ca. 420–520 nm, and light gray color of the brayed samples might be caused by absorption shift at the wavelength > 500 nm, probably due to electron-filling of ETs as the same as the case of brayed/post-calcined rutile titania (section 3.2.1). These electrons filled in ETs were removed by calcination in air to result in the decrease of absorption. Above mentioned changes in color and absorption suggest some changes in structure/morphology of the surface affecting reflection. In addition, the absorption spectra were red shifted by braying and post-calcination, which is due to phase transformation from anatase to rutile as discussed later.

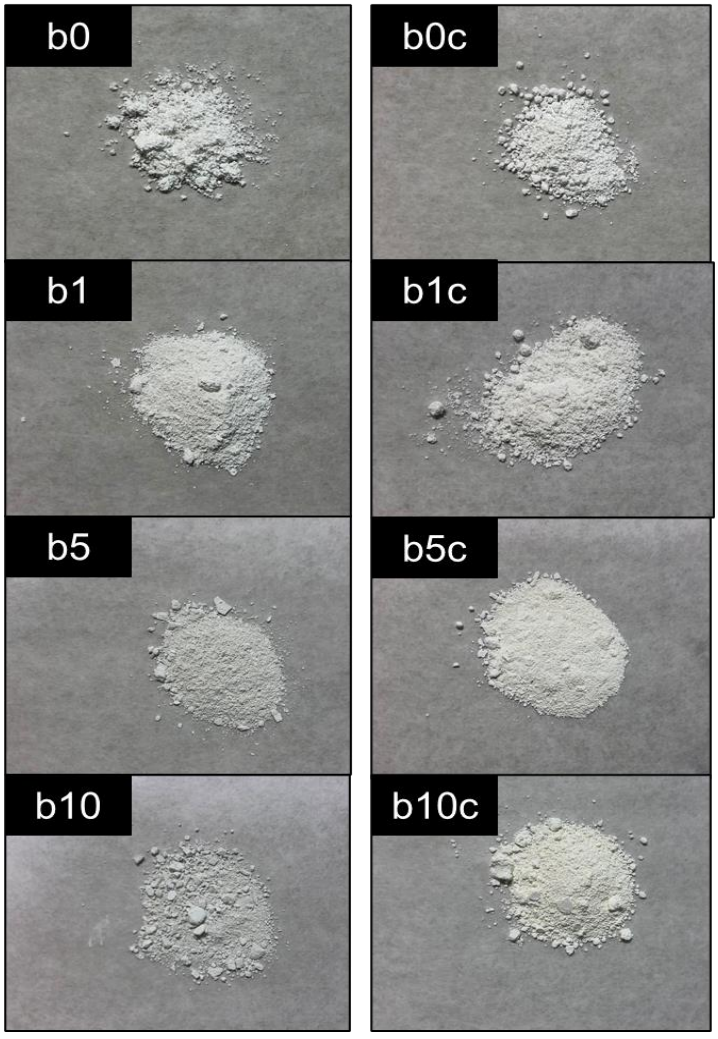

Figure 4-2 Color changes of original (b0), brayed (bX) and post-calcined (bXc) samples.

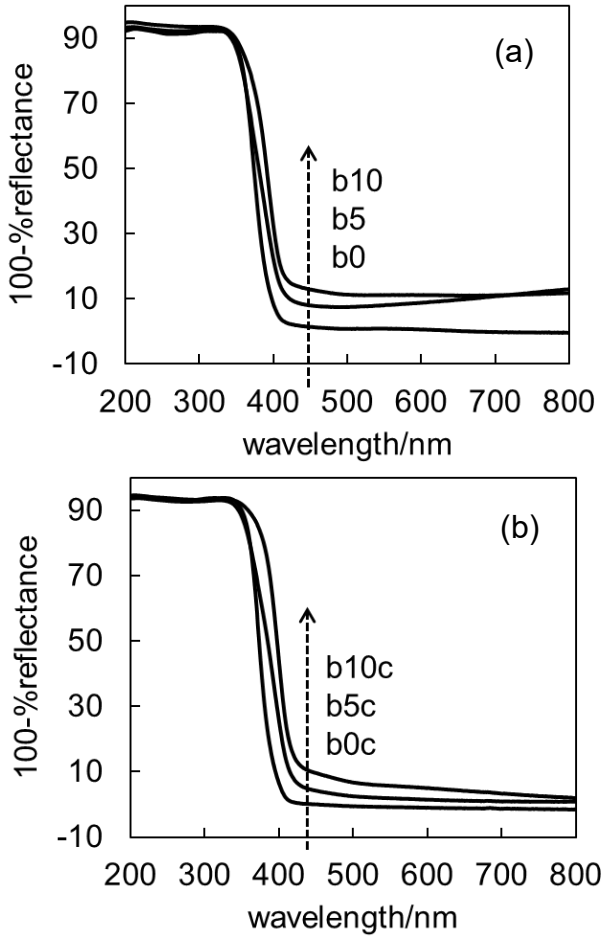

Figure 4-3 Diffuse reflectance spectra of (a) original (b0), brayed (bX) and (b) post-calcined (bXc) samples.

4.2.2 Morphology of Samples

Figure 4-4 shows SEM images of the representative samples. The observed particle size was smaller (ca. 100–150 nm) compared with rutile case, even though SSA of original anatase and rutile are similar as shown in **Table 2-1**. The particle size and morphology were almost no change by braying and post-calcination except for 10-d brayed samples. For 10-d brayed samples, slightly larger particles were observed; small particles were attached to larger particle. However, as mentioned before, there was a limitation on sampling, taking images and checking the size and morphology, therefore, it was rather challenging to say the above-mentioned change (or no change) occurred comprehensively in the samples.

Figure 4-5 shows SSA of original (b0), brayed (bX) and post-calcined (bXc) samples. The SSA was slightly increased by 1-d braying and were almost constant after 1-d braying for the samples brayed < 8 d, while the SSA for the sample brayed >7 d was changed eccentrically. The results suggested negligible changes in particle outer size and porosity of the samples brayed up to 7 d regardless with or without post calcination, and some changes appeared for the samples brayed for > 7 d. (At present, I do not know the reason

of this eccentrical changes in SSA, but aggregation observed in SEM images may give some effects.)

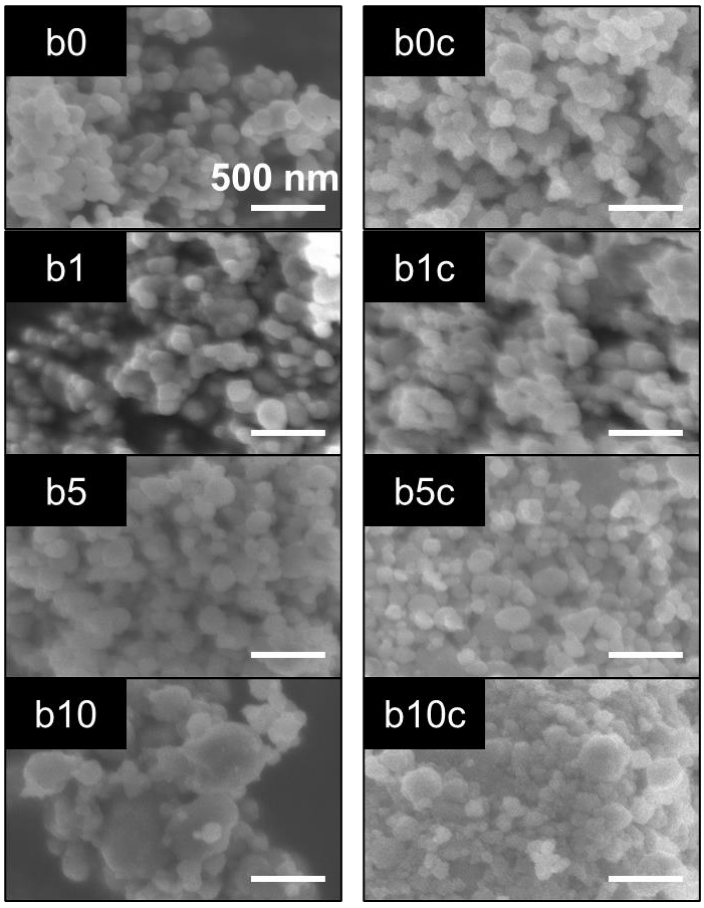

Figure 4-4 SEM images of original (b0), brayed (bX) and (b) post-calcined (bXc) samples.

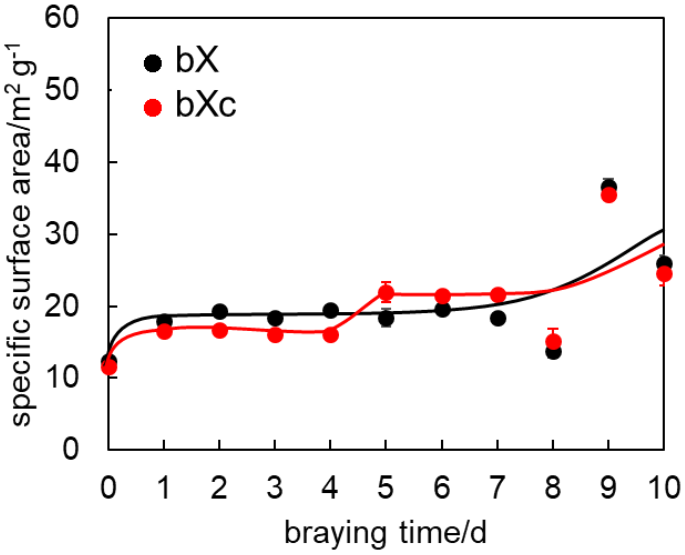

Figure 4-5 Specific surface area of (black) original rutile, brayed and (red) post-calcined samples as a function of braying time.

4.2.3 X-Ray Diffraction Patterns of Samples

XRD patterns of the representative samples are shown in **Figure 4-6**. The peak heights of the diffraction peaks were gradually smaller and the peak width became broader by braying regardless with and without post-calcination, suggesting crystallite sizes were decreased. In addition, new crystalline peaks of rutile and TiO_2-II appeared by braying > 4 d. Since ball milling is reported to cause formation of TiO_2-II from anatase with the orthorhombic structure, braying process has also possibility of inducing TiO_2-II phase as well as rutile phase. On the other hand, post calcination did not cause appreciable change in their diffraction patterns.

Crystalline contents were analyzed by using nickel(II) as an internal standard. It should be noted that contents of TiO_2-II was ignored this time, due to broad and small peak. **Figure 4-7** shows the change in their composition by braying and post-calcination. NC component for b0 sample calculated as the rest of crystalline (92% anatase and 2% rutile) component was ca. 6% and this NC content was not changed by 773-K calcination (b0c). Roughly speaking, braying lead to decrease and increase in the composition of anatase and NC, respectively, and the post calcination could recover this braying-induced composition change partially. This braying induced amorphization of anatase proceeded even rapidly compared with rutile case. In anatase case, heterogeneous braying is obvious to result in eccentrical changes in crystalline composition.

Figure 4-8 shows the crystallite size and lattice strain of each sample. Anatase crystallite size of original sample was 58 nm and it was almost kept by 1-d braying and recovered by post-calcination for the sample brayed for < 5 d. Until 5-d braying, the lattice strain in anatase crystallite was almost negligible. Longer braying induced decrease of anatase crystallite size and increase of lattice strain up to 1%. Those for rutile are shown in **Figure 4-8**(b), but it should be noted that those results might include large error due to obtained from small rutile peaks.

Those results suggested that parts of the anatase crystallites were amorphized by braying and this braying-induced amorphous titania was recovered partially by post calcination if the braying time was shorter than 9 d, but not completely recovered to the original single-crystallites.

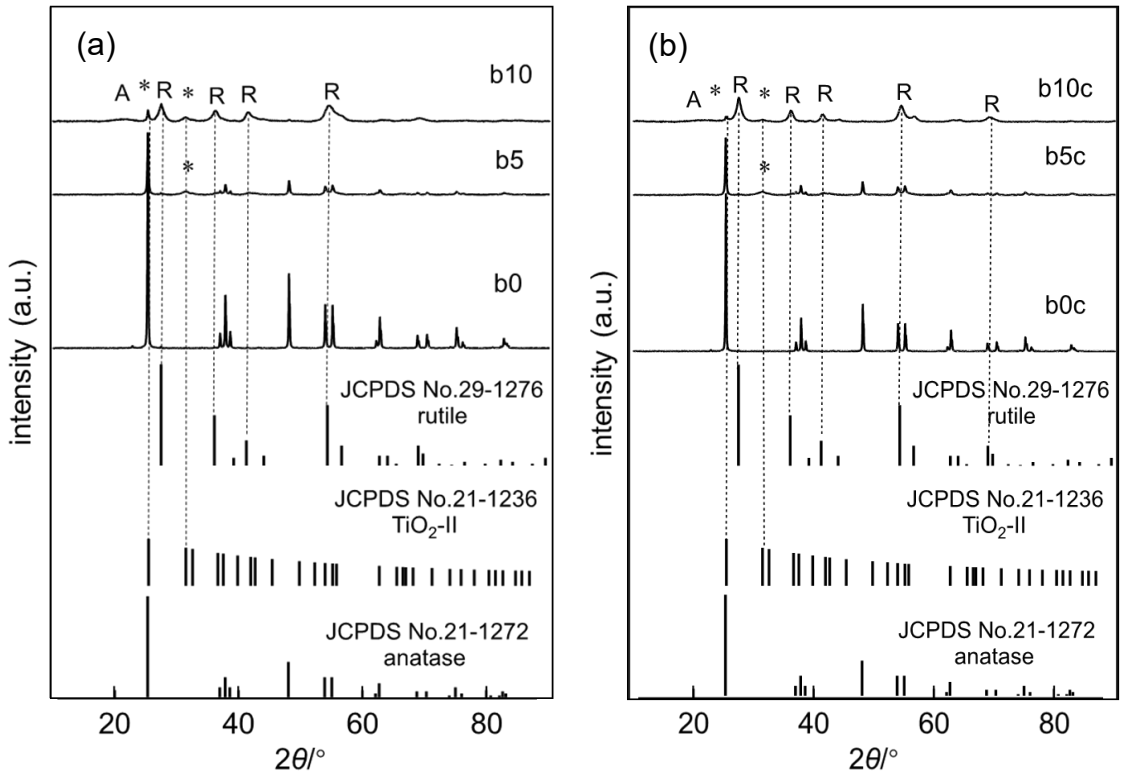

Figure 4-6 X-ray diffraction patterns of (a) original rutile, brayed and (b) post-calcined samples and those of pure rutile, TiO2-II and pure anatase.

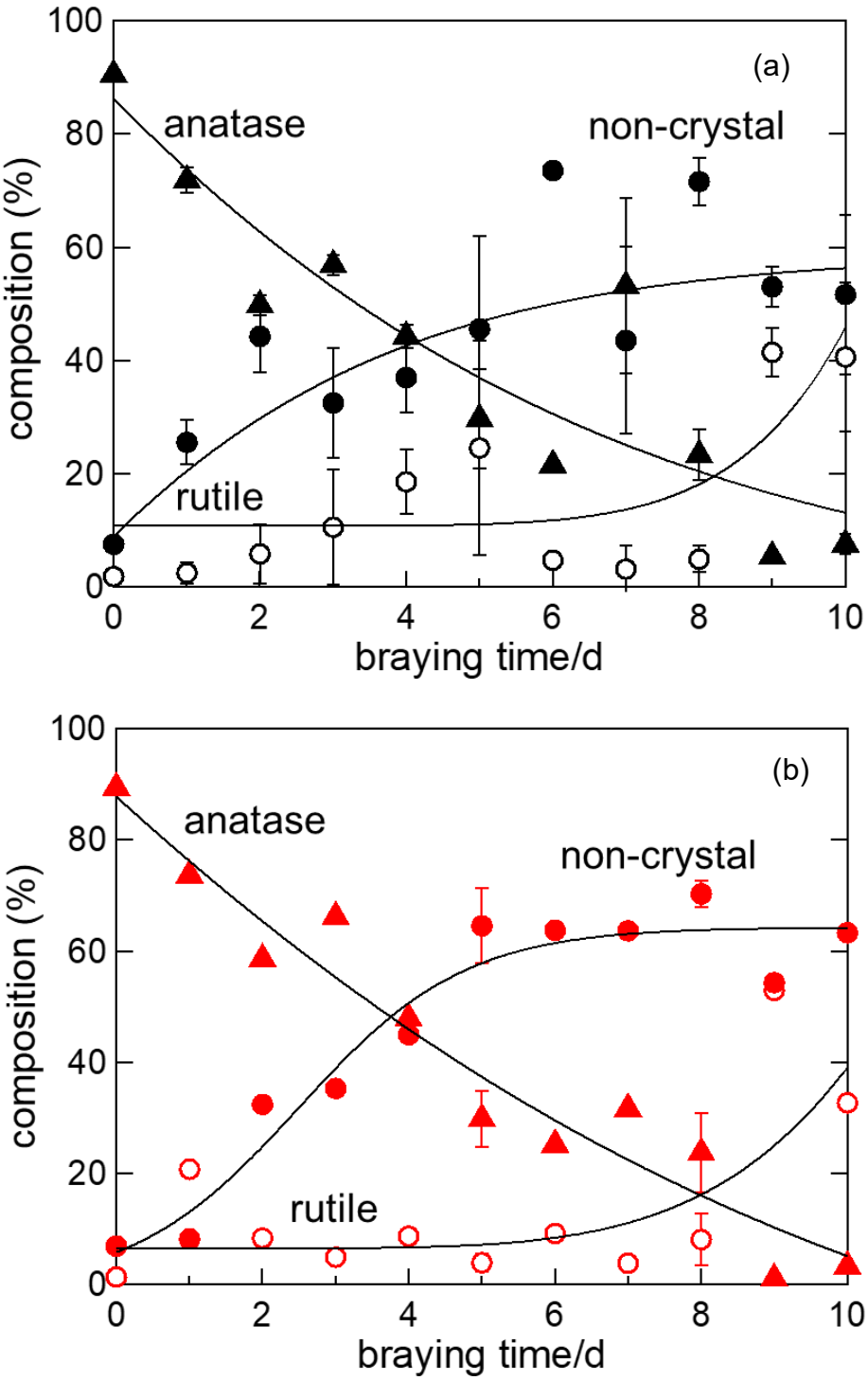

Figure 4-7 Crystalline (anatase; closed triangles, rutile; open circles) and non-crystalline (closed circles) composition of (a) brayed and (b) post-calcined samples as a function of braying time.

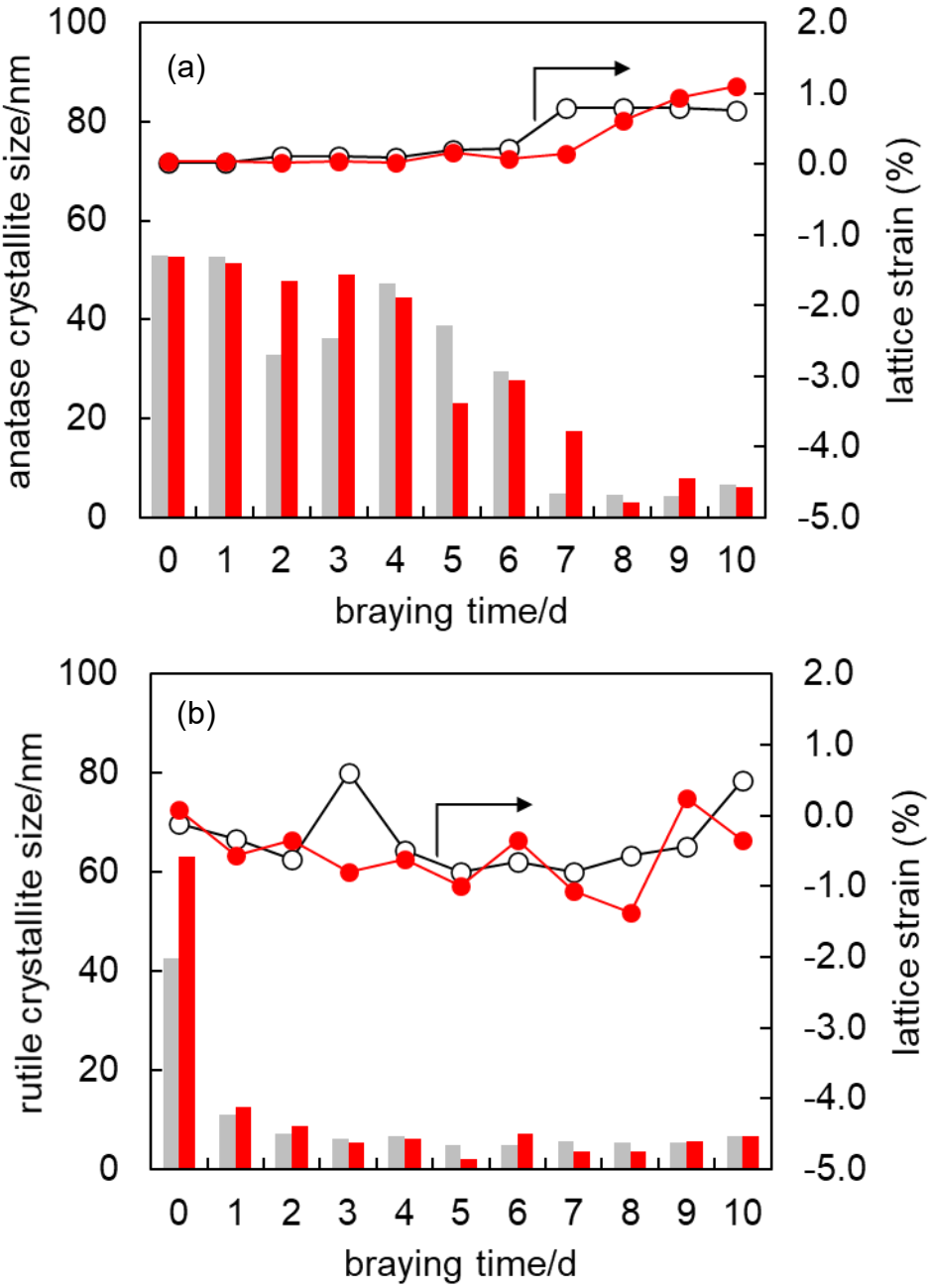

Figure 4-8 Crystallite size (bars for left axis) of (a) anatase and (b) rutile and lattice strain (circles for right axis) of (gray) brayed and (red) post-calcined samples as a function of braying time.

4.3 ERDT/CBB Analyses of Samples

4.3.1 ERDT/CBB Patterns of Samples

Figure 4-9 shows ERDT/CBB patterns of original (b0), brayed (bX) and post-calcined (bXc) samples.

CBB positions were gradually downward shifted by braying and post-calcination indicating the creation of rutile phase, similar results were obtained from the XRD results (section 4.2.3).

For the values of D_{ET}, more than twice enhancement of total ET density was observed by 2-days or longer braying, while post calcination negligibly changed the toral ET density. After that, values of D_{ET} were almost constant except for 10-d braying, where obvious increase in D_{ET} was observed.

For the ERDT patterns shapes, several features were observed. Firstly, broad peaks for b0 and b0c suggest the possible inclusion of rutile in the original anatase sample. By braying, formation of isolated amorphous (am) was obviously observed at >3.4 eV only for b10 sample. In post-calcined samples, intense peaks at ca. 3.0 eV were obtained for the samples brayed for > 1 d as shown in **Figure 4-10**(a), suggesting anatase-rutile contact as discussed later. To clarify these features, subtraction of ERDT pattens of bX from bXc was performed as shown in **Figure 4-10**(b). For the samples brayed for 4–8 d, a slightly higher energy peak located at ca.3.2 eV was decreased and a peak slightly higher than that of rutile, position of which was located at 2.9 eV, was increased, suggesting anatase was recrystallized into rutile and/or formation of grain boundaries upon calcination. Those features could be explained and clarified by assuming ICTE as discussed in the following section.

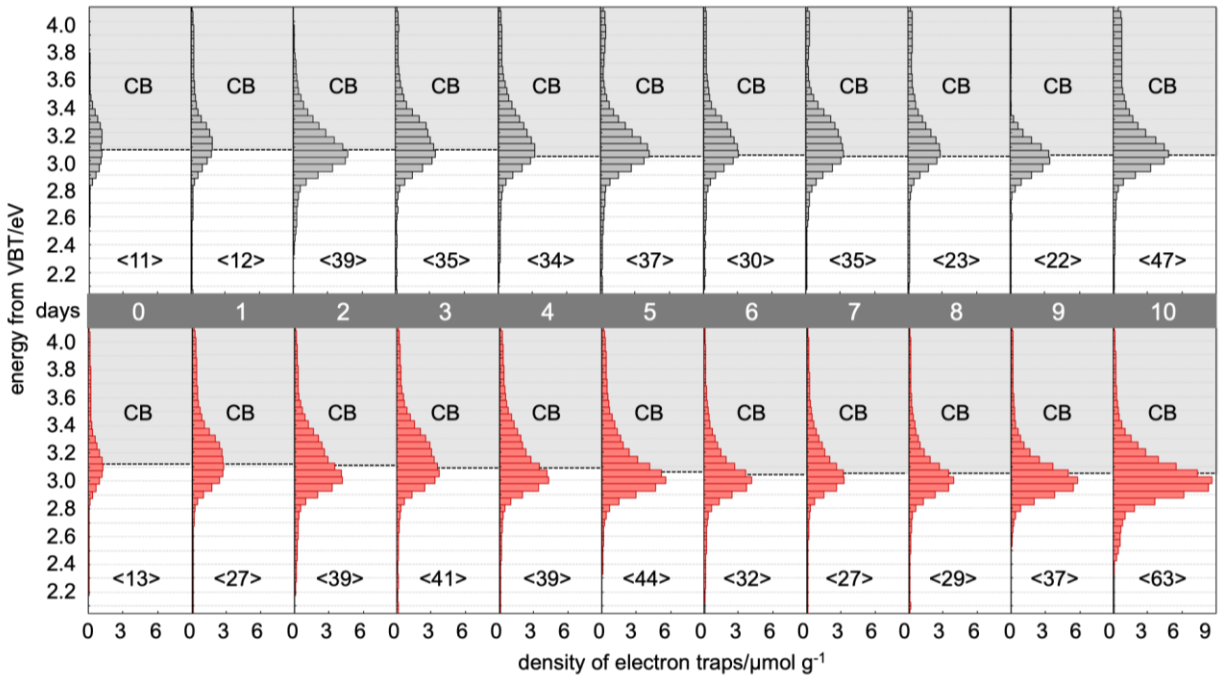

Figure 4-9 ERDT/CBB patterns of (upper) original, brayed and (lower) post-calcined samples. Doted lines indicate conduction band-bottom position and figures in < > denote total density of electron traps.

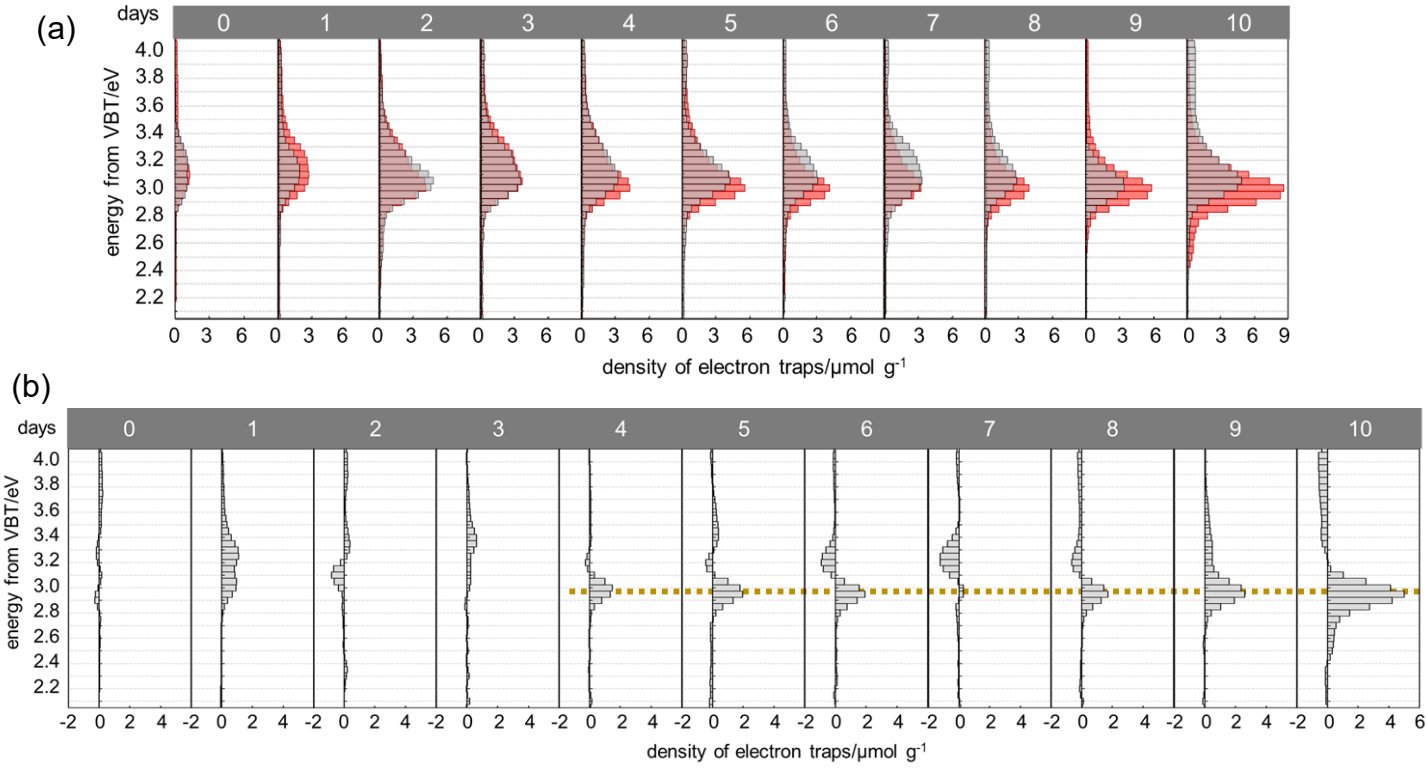

Figure 4-10 (a) Overlapping ERDT patterns of (black) original, brayed and (red) post-calcined samples and (b) subtracted ERDT patterns of post-calcined samples from original and brayed samples. Peaks of electron traps in negative and positive value indicate decrease and increase by post calcination, respectively. Dotted line indicates the peak position of the sample brayed for >3 d.

4.3.2 *Simulation of ERDT Patterns and Interparticle Charge-Transfer Excitation between Anatase, Rutile and Amorphous Titania*

In this anatase-based samples, it should be considered the ICTE among anatase, rutile and amorphous since those components coexist in the samples. For elucidation of peak positions, ERDT patterns of anatase (Showa Denko ST-21 was used as a reference anatase sample instead of Merck, containing small amount of rutile, to avoid confusion.ST-21), rutile, commercial amorphous titania (AMO) and their 50/50 weight ratio mixture sample were measured as shown in **Figure 4-11** . In order to reproduce each ERDT pattern of a 50/50 mixture, simulation was performed (SIM), as the same as section 3.3.2. From the results, it can be said that h-DOS of anatase may be located 0.20 eV lower compared with rutile to result in 0.20 eV downshift giving highest ζ_S value of 0.69. Similar result (0.20 eV downshift) was also reported in the recently published paper from our laboratory. For the case of mixture with anatase and amorphous titania, h-DOS of amorphous titania may be located 0.17 eV lower compared with anatase giving highest ζ_S value of 0.79. Compared with rutile case, ζ_S value shows slightly higher, which indicating the h-DOS distribution of anatase is slightly similar to that of amorphous titania.

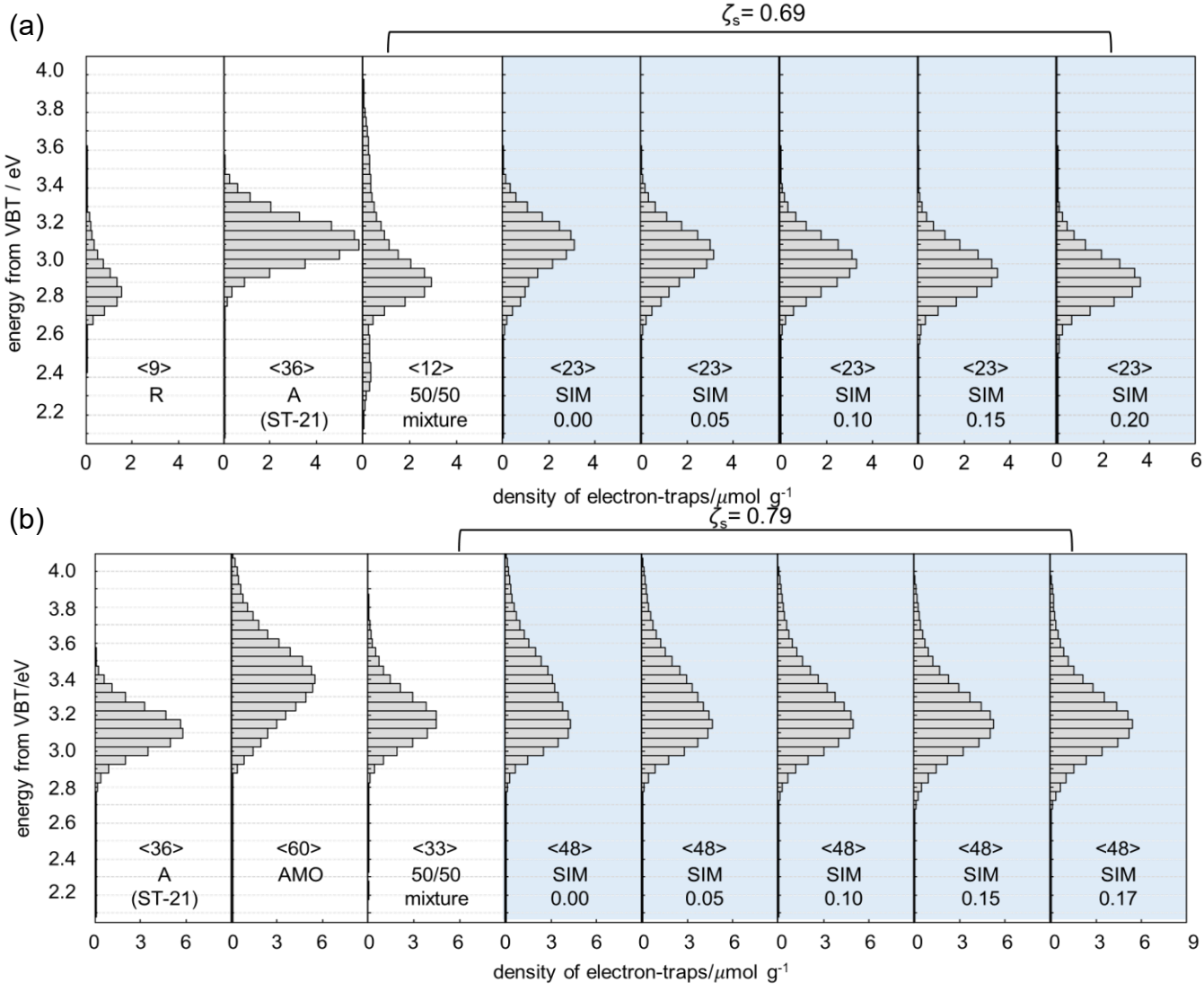

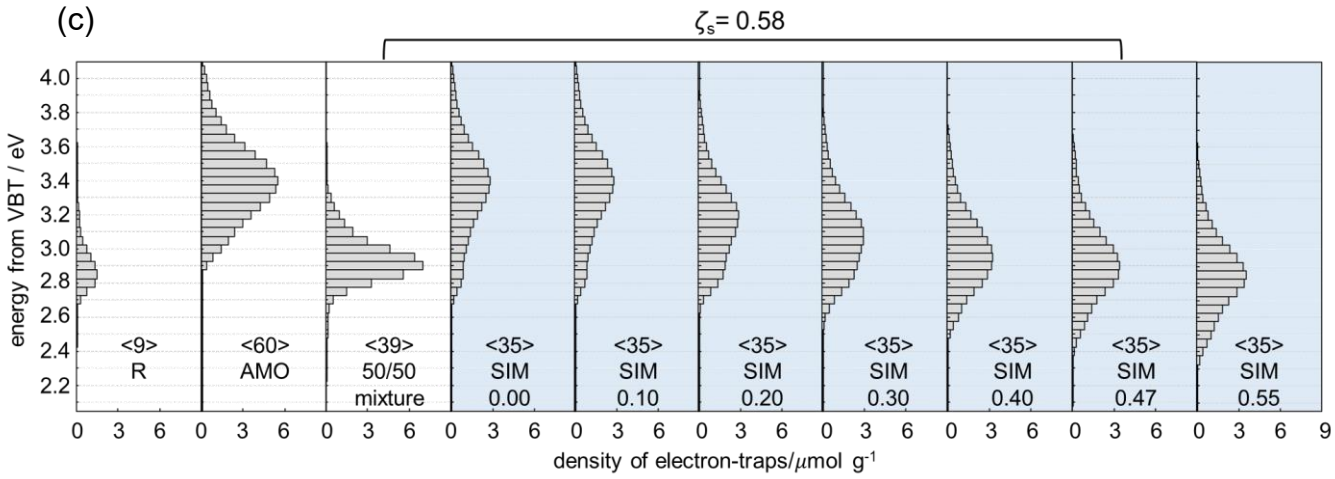

Figure 4-11 ERDT patterns of mixture of anatase (ST-21), rutile and amorphous titania and their 50/50 mixtures. Also shown in blue background are representative simulated ERDT patterns by summing up a pattern of (a) 50% rutile with lower-energy shifted pattern of 50% anatase and (b) 50% anatase with lower-energy shifted pattern of 50% amorphous titania. ((c) is the same as **Figure 3-13**(a).)

4.3.3 Deconvolution of ERDT Patterns with Gaussian-curve Fitting

ERDT patterns of anatase (ST-21) and their mixtures with rutile and commercial amorphous titania (AMO) were deconvoluted as shown in **Figure 4-12**. ERDT patterns of anatase (ST-21) was deconvoluted to two peaks, the positions of which are at 3.1 and 3.3 eV. Those peaks were ascribed to anatase (A) and amorphous on anatase (am-A), amorphous in contact with anatase, respectively. The XRD result of anatase ST-21 also revealed 13% of non-crystalline inclusion. ERDT patterns of the mixture of anatase ST-21 and rutile suggested the position of anatase (A) on rutile (A-R), anatase in contact with rutile is located at approximately 3.0 eV and rutile 2.9 eV. ERDT patterns of mixture with anatase and AMO suggested the anatase (A) and amorphous on anatase (am-A), amorphous in contact with anatase, appear at 3.1 to 3.2 eV and 3.3 eV, respectively, which is consistent with the result of **Figure 4-12**(a). It has been already known that isolated amorphous (am) and amorphous on rutile (am-R) appear at 3.4 eV and 3.0 eV respectively as mentioned in section 3.3.3.

Figure 4-13 shows representative deconvolution results of ERDT patterns for original (b0), brayed (bX) and post-calcined (bXc) samples and the results of peaks positions and peak width (FWHM) are summarized in **Table 4-1**. The FWHM of am-A/R peak for b8 sample is slightly large, similar with that of am, but I ascribed it as am-A/R, judging from the peak position. The original b0 might have small rutile deposits and amorphous layer on the surface and calcination induced crystallization of amorphous to A-R. For curve fitting of these ERDT patterns, the best results were obtained by assuming very broad am-A/R peak, a combination of two broad am-A and am-R peaks. The shorter-time braying induced the formation of am-A/R. After calcination, A and A-R were recovered and am-A/R was decreased, but appreciable am-A/R peaks remained due to grain boundary, while

the shape of patterns seemed almost the same as that of the original b0c. The am-A/R peaks disappeared by the further braying to create am-R. One of the possible explanations is that the surface of anatase was amorphized to give am-A/R, and further braying induced the crystallization of amorphous into rutile to give am-R. This amorphous, contact with only rutile, seemed to be crystallized into rutile upon calcination. At the same time, crystallization left grain boundaries at am-R by calcination.

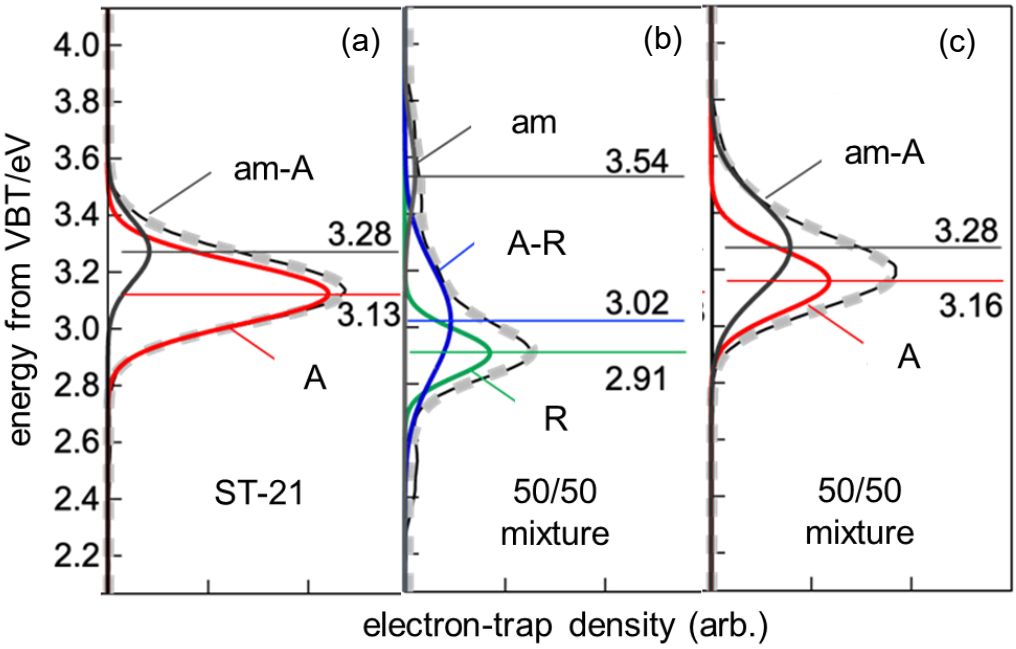

Figure 4-12 Deconvolution of ERDT patterns for (a) anatase (ST-21), (b) mixture of rutile and anatase (ST-21) in the ratio of 50/50 (c) mixture of anatase (ST-21) and amorphous titania in the ratio of 50/50 with Gaussian-curve fitting.

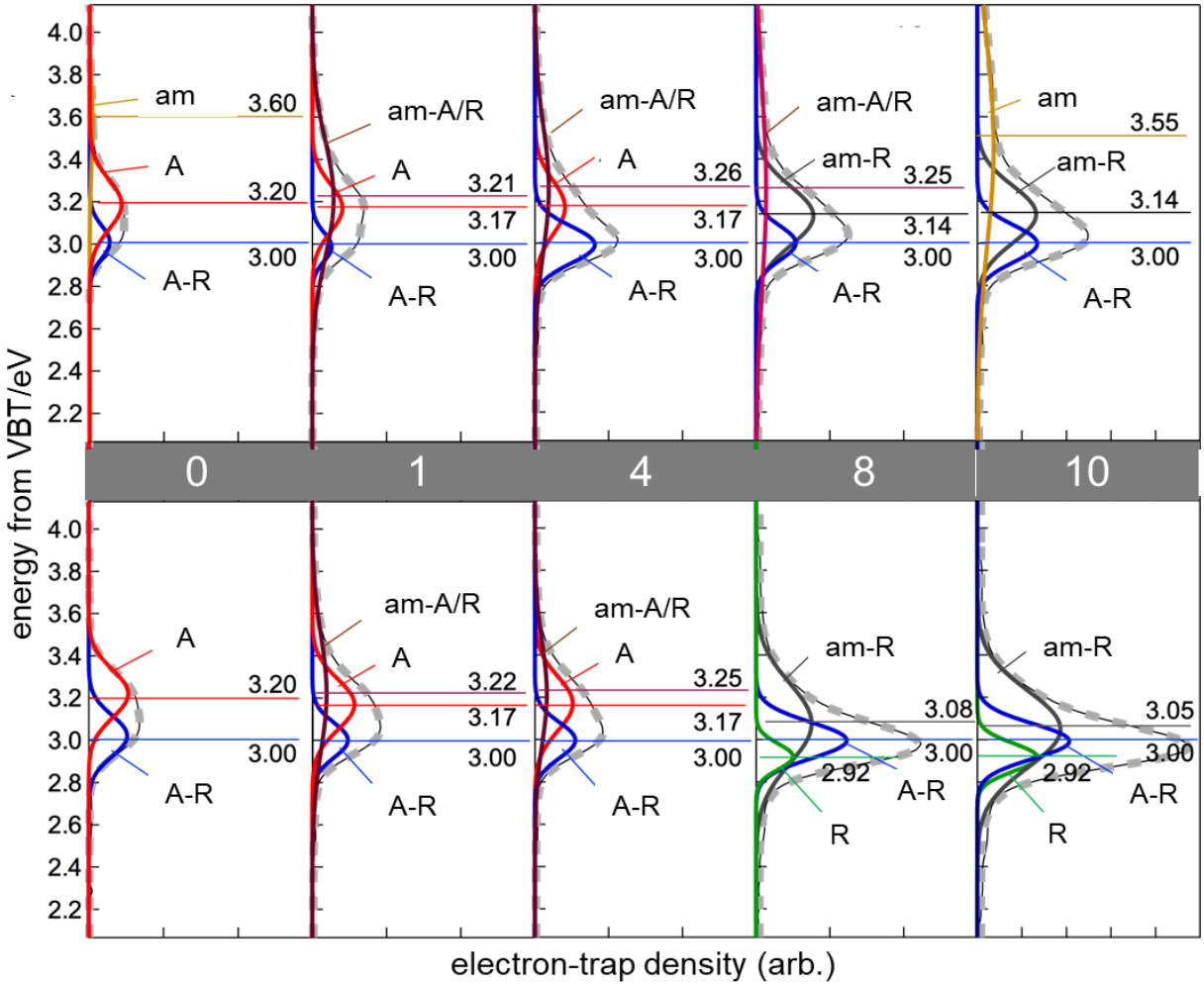

Figure 4-13 Representative deconvolution results of ERDT patterns for (upper) original (b0), brayed (bX) and (lower) post-calcined (bXc) samples.

Table 4-1 Summary of (a) peaks positions and (b) peak width (FWHM) in Gaussian-curve fitting.

(a)

code	peak position/eV					
	R	A-R	am-R	A	am-A/R	am
b0	-	3.00	-	3.20	-	3.60
b1	-	3.00	-	3.17	3.21	-
b4	-	3.00	-	3.17	3.26	-
b8	-	3.00	3.14	-	3.25	-
b10	-	3.00	3.14	-	-	3.55

code	peak position/eV					
	R	A-R	am-R	A	am-A/R	am
b0c	-	3.00	-	3.20	-	-
b1c	-	3.00	-	3.17	3.22	-
b4c	-	3.00	-	3.17	3.25	-
b8c	2.92	3.00	3.08	-	-	-
b10c	2.92	3.00	3.05	-	-	-

(b)

code	FWHM/eV					
	R	A-R	am-R	A	am-A/R	am
b0	-	0.18	-	0.28	-	0.46
b1	-	0.16	-	0.27	0.65	-
b4	-	0.21	-	0.29	0.69	-
b8	-	0.19	0.33	-	1.08	-
b10	-	0.21	0.32	-	-	1.11

code	FWHM/eV					
	R	A-R	am-R	A	am-A/R	am
b0c	-	0.23	-	0.27	-	-
b1c	-	0.20	-	0.28	0.64	-
b4c	-	0.20	-	0.30	0.56	-
b8c	0.14	0.20	0.44	-	-	-
b10c	0.15	0.19	0.43	-	-	-

4.3.4 *Schematic Image of Changes in Surface/Bulk Structures by Braying and Post-Calcination*

Figure 4-14 shows schematic image of structural change of anatase-based samples. Original anatase sample are composed of anatase and small amounts of amorphous titania and rutile, which contact with core anatase to result in shifted ERDT pattern of anatase to lower energy side. Similar to the case of rutile samples, braying induces the surface amorphization and recrystallization upon calcination to yield amorphous in contact with anatase and rutile (am-A/R), but the formation of grain-boundaries is limited to the long-time brayed samples. Thereby the structure of short-time brayed-post calcined samples seem similar to original samples except for the presence of small amount of grain boundaries. At present, I do not know the reason why post-calcination of brayed anatase sample left small amount of grain boundaries, but it might be due to anatase nature. Longer-time braying makes surface amorphous layer thicker while the core anatase smaller and induces the crystallization of this amorphous titania into rutile. Decomposition of particles into small pieces, which was observed in rutile case, was not observed in anatase case. This model of structure changes can be elucidated only based on ERDT/CBB patterns.

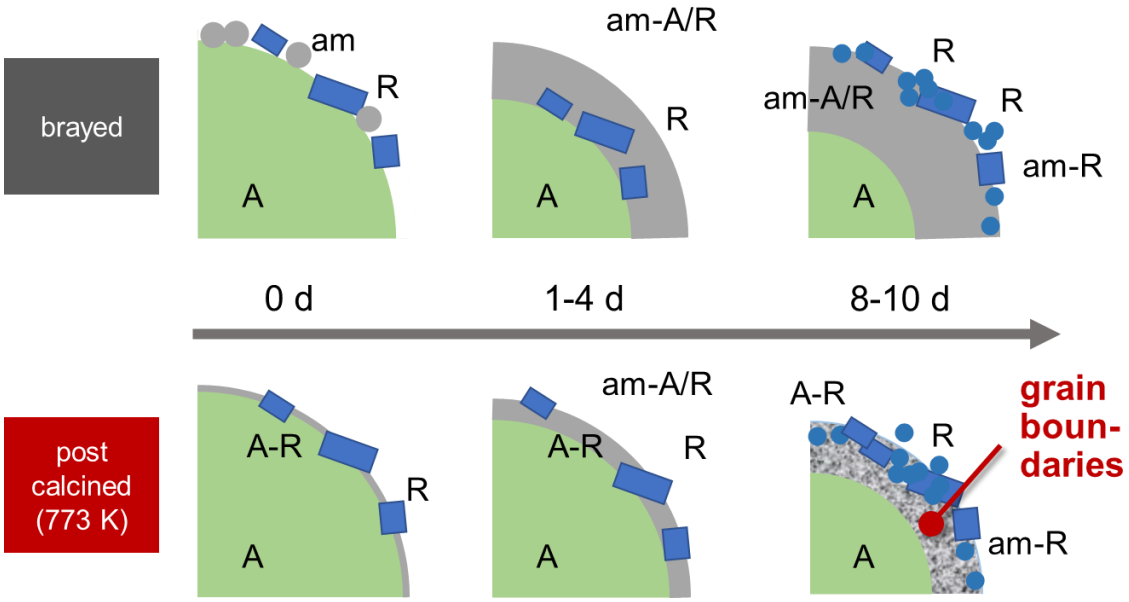

Figure 4-14 Schematic image of changes in surface and bulk structures of anatase sample by braying and post-calcination.

4.3.5 *Relation with Surface Structure and Photocatalytic Activity*

To describe relation with surface and bulk structures and photocatalytic activity, I display again **Figure 4-1** and **Figure 4-14** along with each reaction equations below, for convenience. Similar change in the structure of anatase-based samples is proposed. In both photocatalytic reaction systems, the activities were decreased by braying due to the decrease in active anatase content. Similar with rutile case, amorphous titania formed by braying (am/am-A/R) may act as an inert for those photocatalytic activity since amorphous titania is inactive for both systems, and there might be also shading effect. For the grain boundaries, different from the rutile-based samples, low density or amount of grain boundaries were formed for short-time brayed-post calcined samples. Therefore, the activities were almost recovered by calcination especially for the CO_2 system, which is less sensitive to the grain boundaries.

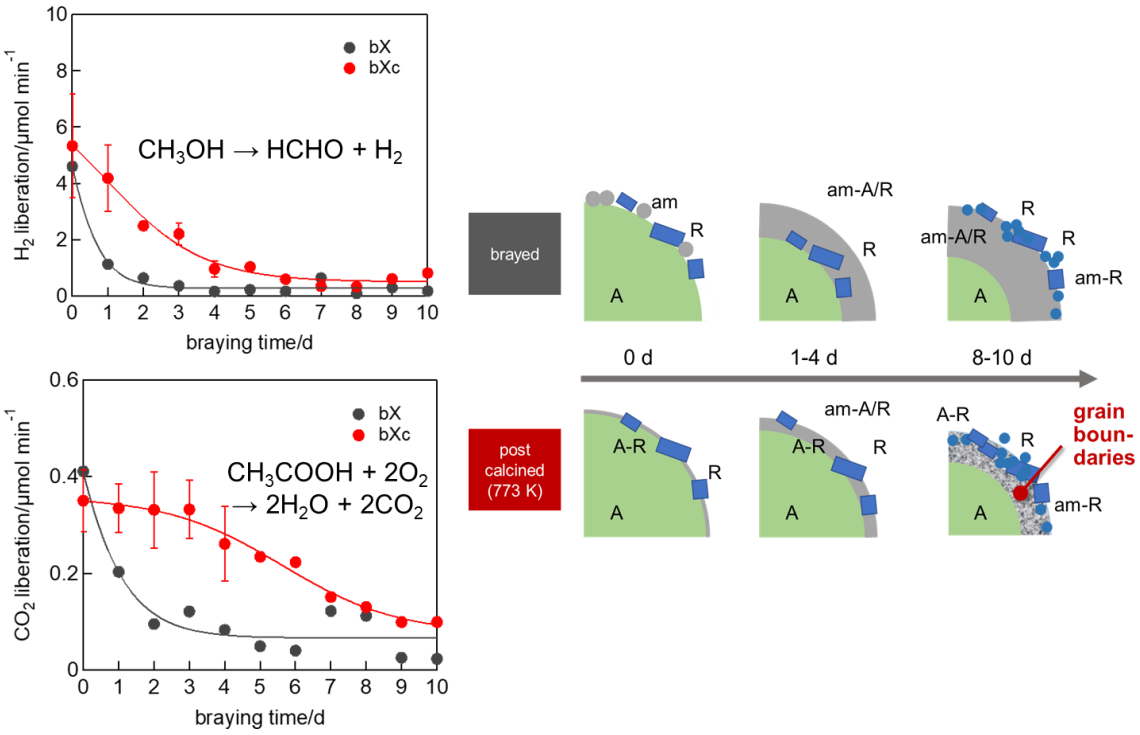

4.4 *Conclusions*

The structure and bulk changes of anatase-based sample by braying and post-calcination were examined by conventional analytical technics and RDB-PAS. Those influences on two photocatalytic activities; hydrogen liberation from deaerated aqueous 50wt% methanol with chloroplatinic acid and carbon-dioxide liberation from aerobic aqueous 5vol% acetic acid, were considered. Similar changes in their structure were observed in anatase case; the formation of three kinds of amorphous titania (amorphous in contact with core anatase and/or surface rutile, isolated amorphous and grain boundary) by braying and partial recrystallization by post-calcination, while braying and post-calcination induced crystal transformation into rutile also occurred. In anatase case, less amount of grain boundaries was formed to result in recovery of photocatalytic activities by post-calcination especially for the CO_2 system.

Chapter 5

Changes in Surface/Bulk Structure and Photocatalytic Activity by Braying and Post-calcination of Brookite-Based Titania Samples

In this chapter, a brookite sample, HPC titania, was used as a starting material for braying and post-calcination treatments. It should be noted that another name of the brookite titania is named as "plate titania" in mineral, so it is easily to assume that the structure of brookite is formed from layered titania. In addition, the brookite sample contains small amount of anatase originally as shown in **Table 2-1**.

5.1 Photocatalytic Activity of Brayed and Post-calcined Rutile Samples

Figure 5-1 shows photocatalytic activities of original (b0), brayed (bX) and post-calcined (bXc) samples. Braying and post calcination changed the photocatalytic activities of the brookite sample, however, the deactivation was not evident especially for CO_2 system compared with the cases of rutile and anatase. The partial recovery of the activity by post calcination was not significant in both systems. Outliers are also observed, but it seems even more obvious than rutile and anatase case.

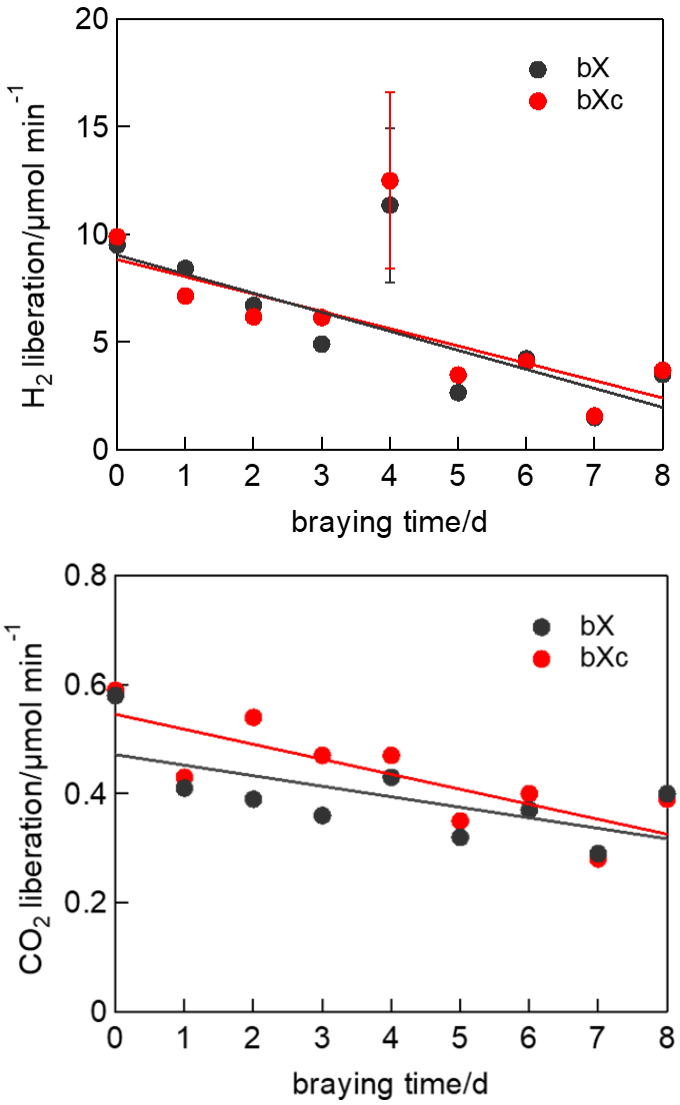

Figure 5-1 Photocatalytic activities of (black) original anatase, brayed and (red) post-calcined samples in (a) H_2 system and (b) CO_2 system.

5.2 Conventional Analyses of Brayed and Post-calcined Brookite Samples

5.2.1 Sample Colors and Diffuse Reflectance Spectra of Samples

Figure 5-2 shows color changes by braying and post-calcination. As similar with rutile and anatase case, the color was changed to slightly yellowish light gray, then slight yellow color remained after post-calcination.

Figure 5-3 shows DRS of the representative samples. Similar with rutile and anatase case, the yellowish sample color was owing to blue-color absorption at ca. 420–520 nm, and light gray color of the brayed samples might be caused by absorption shift at the wavelength > 500 nm, probably due to electron-filling of ETs (reduction). These electrons filled in ETs were removed by calcination in air to result in the decrease of absorption.

Above mentioned changes in color and absorption suggest some changes in structure/morphology of the surface affecting reflection. In addition, the absorption edges were slightly red shifted by braying and post-calcination, which might be due to phase transformation from brookite to something as discussed later.

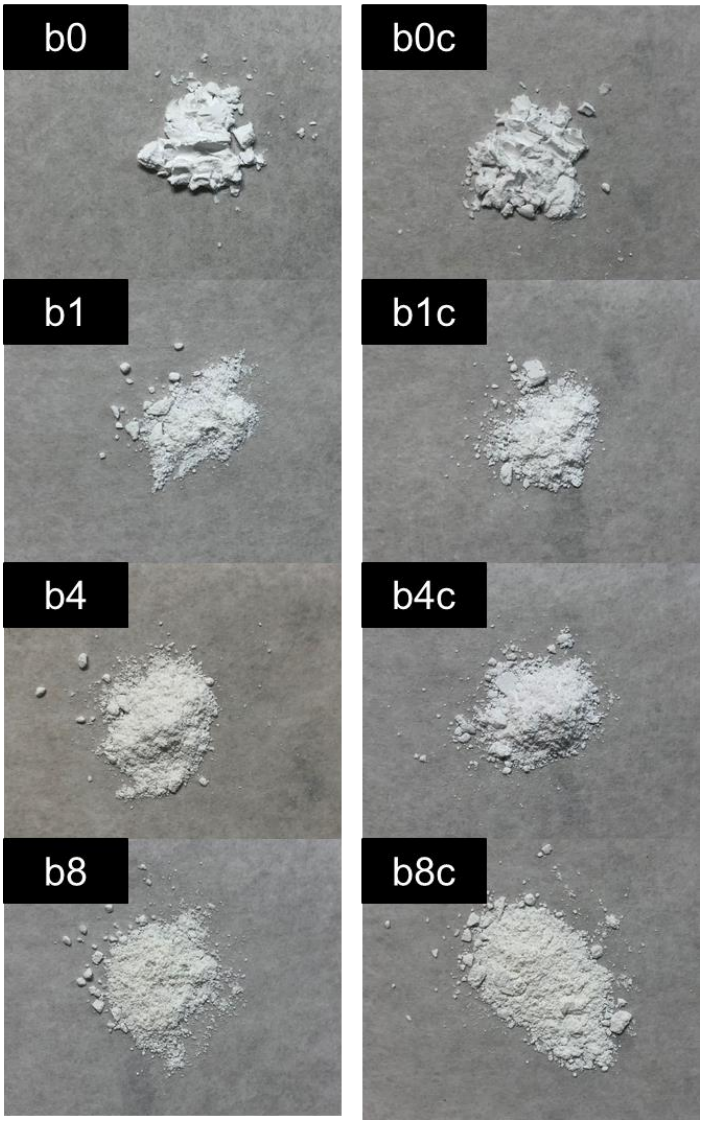

Figure 5-2 Color changes of original (b0), brayed (bX) and post-calcined (bXc) samples.

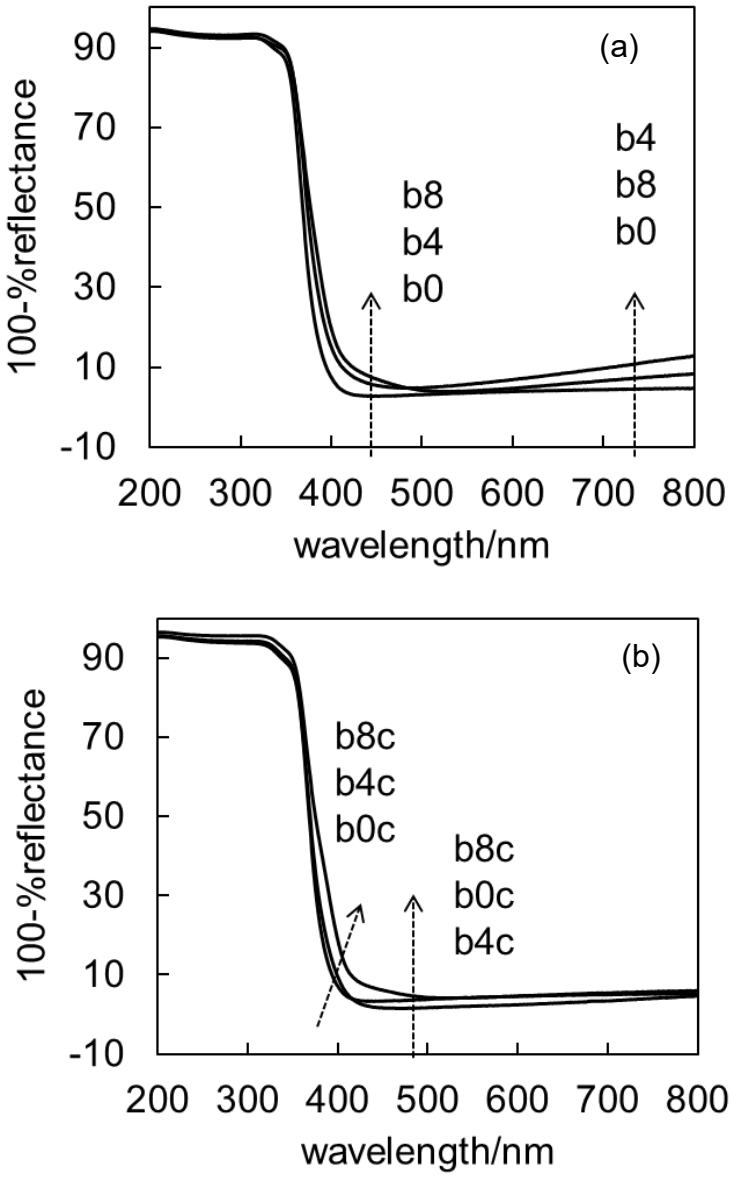

Figure 5-3 Diffuse reflectance spectra of (a) original (b0), brayed (bX) and (b) post-calcined (bXc) samples.

5.2.2 Morphology of Samples

Figure 5-4 shows SEM images of the representative samples. The particle shape of the original brookite was different from rutile nor anatase; it was formed by aggregation of rectangular-like particle (ca. 2 μm), which was formed by aggregation of smaller (few-ten nm) spherical particles, to give rougher surface compared with rutile and anatase (SSA of brookite is slightly larger than those of original rutile and anatase as shown in **Table 2-1**.) as shown in lower panel of **Figure 5-4**. After 1-d braying, these original larger secondary particles were not observed any more, and only smaller spherical particles were observed. The particle size and morphology seemed almost no change by braying and post-calcination up to 10 d.

Figure 5-4 shows SSA of original (b0), brayed (bX) and post-calcined (bXc) samples. The changes in SSA also showed different behavior with rutile and anatase; gradually decreased by braying and recovered by longer-braying, but overall, those changes were eccentrical. At present, I do not know the reason of this eccentrical changes in SSA, but aggregation of small particles observed in SEM images may give some effects. By post-calcination, their SSA decreased furtherly.

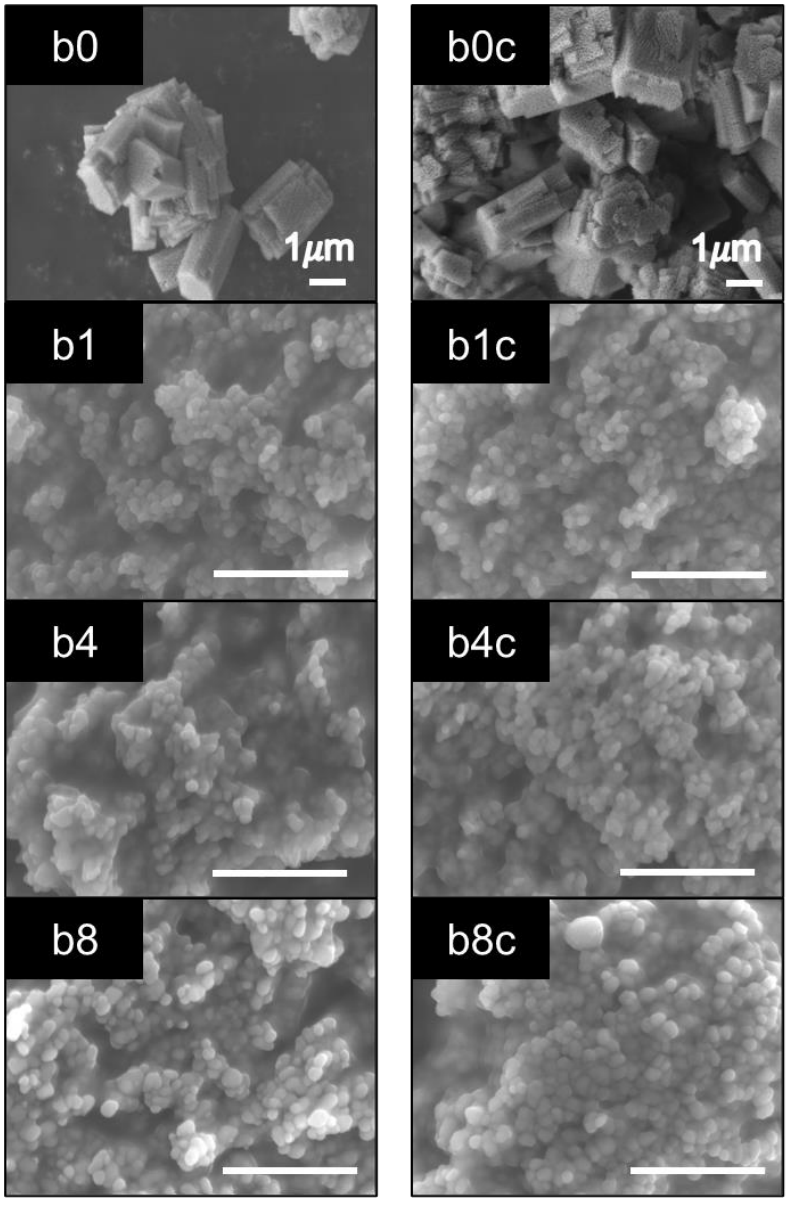

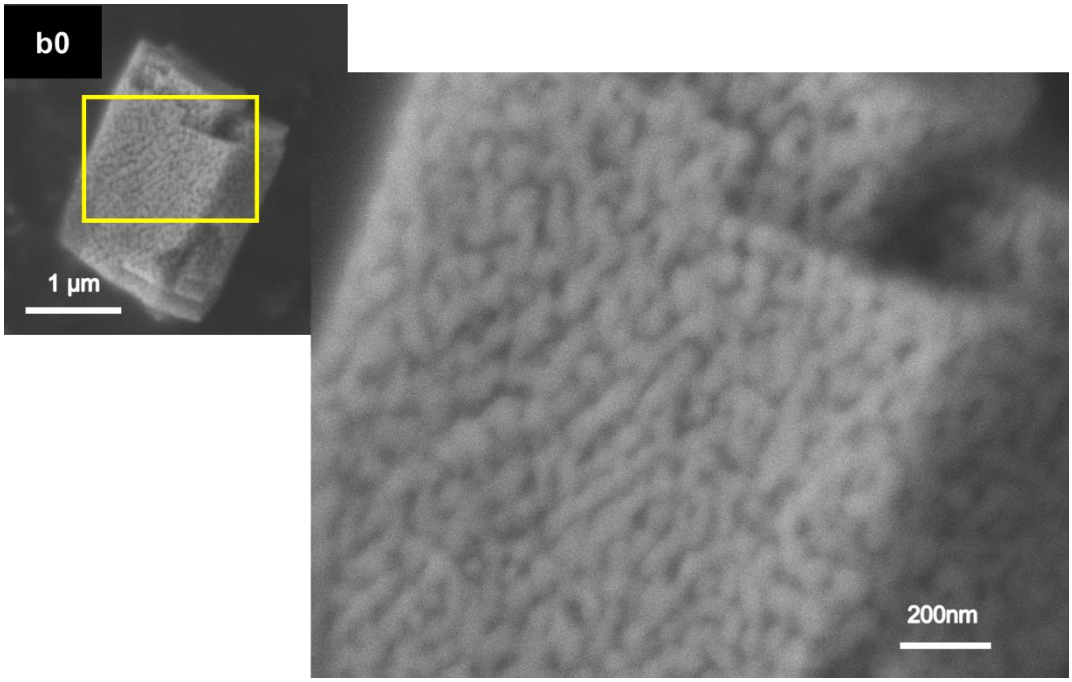

Figure 5-4 SEM images of original (b0), brayed (bX) and post-calcined (bXc) samples. White bars indicate 500 nm except for b0 and b0c samples. Lower panel shows magnification of SEM image for b0 sample.

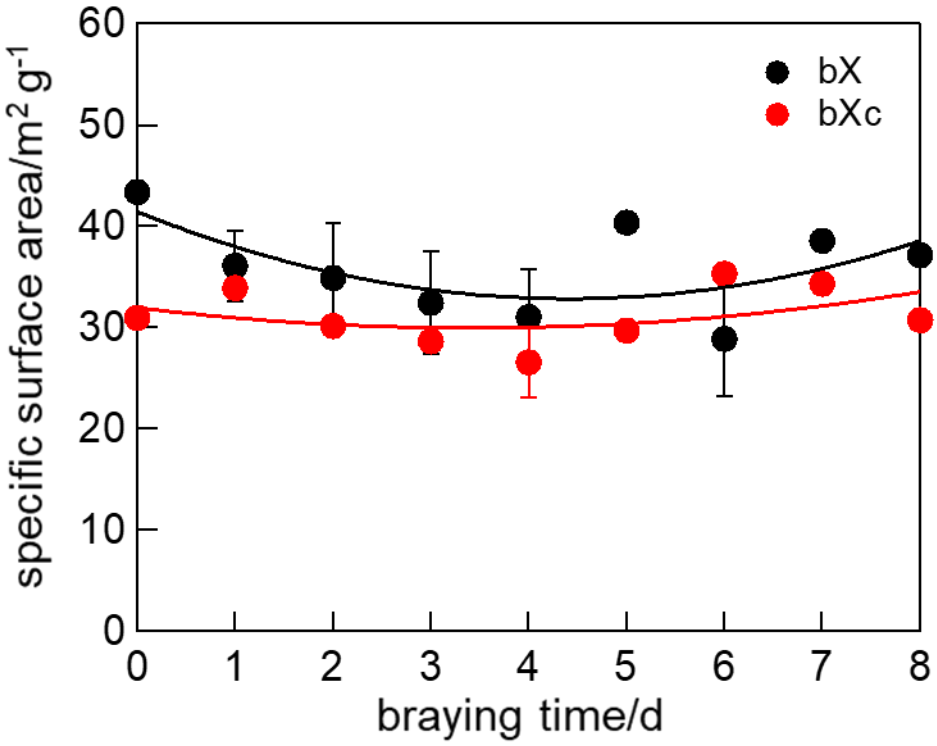

Figure 5-5 Specific surface area of (black) original rutile, brayed and (red) post-calcined samples as a function of braying time.

5.2.3 X-Ray Diffraction Patterns of Samples

XRD patterns of the representative samples are shown in **Figure 5-6**. Most of the diffraction peaks of original brookite correspond well with those of brookite. The appearance of peaks at 2θ = 25.3°, 38.3° and 48.3° indicates the existence of anatase in original brookite. Compared with rutile and anatase cases, the changes in peak height and peak shape by braying were not obvious, suggesting no changes in crystallites.

Crystalline contents were analyzed by using nickel(II) as an internal standard and **Figure 5-7** shows the change in their composition by braying and post-calcination. NC component for b0 sample calculated as the rest of crystalline (77% brookite and 5% anatase) component was ca. 18% and this NC content was slightly increased by 773-K calcination (b0c). Honestly speaking, the changes of those components by braying and post-calcination were eccentrical; brookite contents were almost no change by braying while they were decreased by post-calcination. Changes in NC contents by braying were also eccentrical and those changes by post-calcination were unexpected, i.e., NC contents were increased by post-calcination. The changes of anatase contents seemed constant by braying and increase by post-calcination. In brookite case, aggregation of small particles may affect more eccentrical changes in crystalline composition than heterogeneous braying. **Figure 5-8** shows the crystallite size and lattice strain of each sample. The crystallite size of original brookite was 22 nm and it was almost kept up to 10-d braying and slightly increased by post-calcination. The lattice strains in brookite crystallite were slightly changed up and down by braying but they were decreased by post-calcination to be negligible.

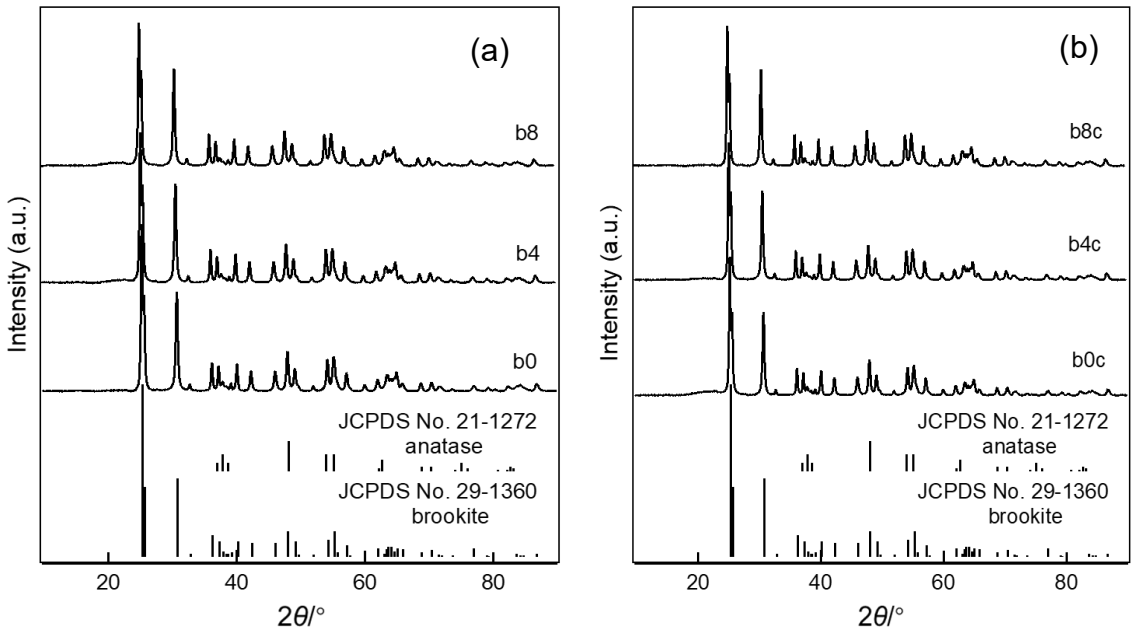

Figure 5-6 X-ray diffraction patterns of (a) original rutile, brayed and (b) post-calcined samples and those of pure brookite and pure anatase.

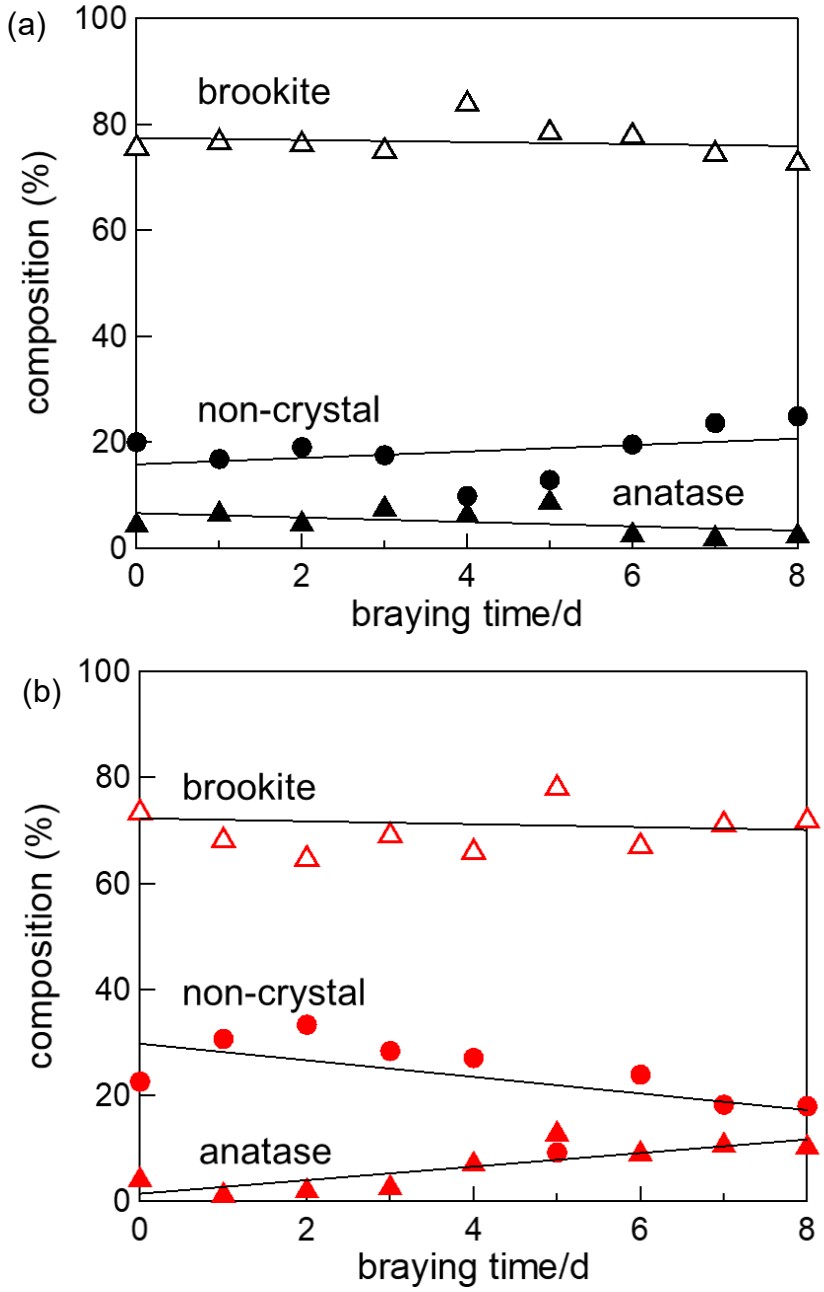

Figure 5-7 Crystalline (brookite; open triangles, anatase; closed triangles) and non-crystalline (closed circles) composition of (a) brayed and (b) post-calcined samples as a function of braying time.

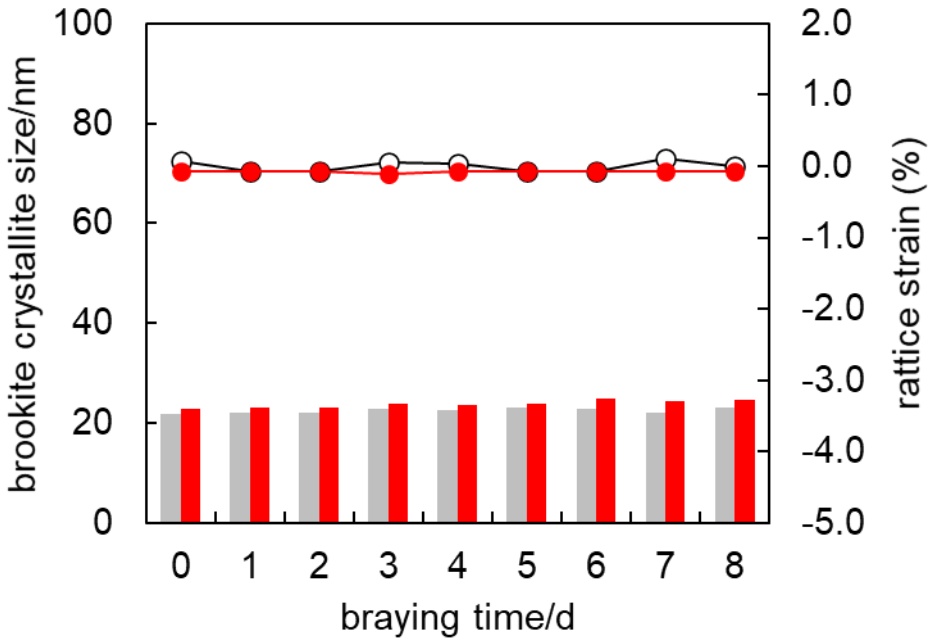

Figure 5-8 Crystallite size (bars for left axis) of brookite and lattice strain (circles for right axis) of (gray) brayed and (red) post-calcined samples as a function of braying time.

5.3 ERDT/CBB Brookite of Samples

5.3.1 ERDT/CBB Patterns of Samples

Figure 5-9 shows ERDT/CBB patterns of original (b0), brayed (bX) and post-calcined (bXc) samples.

CBB positions were gradually downward shifted by braying and post-calcination indicating the creation of different phase (which might be anatase phase, but the bandgap of brookite and anatase are reported 3.0 and 3.2 eV, respectively. So, if anatase was formed, the CBB must be upward shifted. At present, I do not know otherwise.); similar results were obtained from the XRD results (section 5.2.3).

For the values of D_{ET}, it was decrease by 1-d braying and "almost" constant up to 8-d braying (These behaviors are similar with the results of SSA by braying, which support that ETs are mainly located on the surface and RDB-PAS observed that surface-located ETs.), while post calcination slightly decreased the total ET density, which is also unexpected because D_{ET} is generally increased by post-calcination in air (oxidation). One possible reason I could consider at present is that the ET densities of brookite and amorphous titania, which is included in brookite, are different and that of brookite is smaller than that of amorphous titania.

For the ERDT patterns shapes, the ERDT peak of b0 sample is located at 3.25 eV and post calcination did not change ETs peak position. By braying/post-calcination, two features were observed. Firstly, broad and higher-energy peaks for b0 and b0c suggest the possible inclusion of amorphous titania, while that of b0c was slightly narrowed. By

braying, new peaks (shoulder) was observed at ca. 3.0 eV, suggesting something was newly created, and these peaks were disappeared by post-calcination as shown in **Figure 5-10**(a).

To clarify these features, subtraction of ERDT patterns of bX from bXc was performed as shown in **Figure 5-10**(b). Roughly speaking, it can be said that new peak was not appeared and peak located at ca.3.05 eV was decreased by post-calcination, suggesting no grain boundaries were formed and something was recrystallized upon calcination. Those features could be explained detail by assuming ICTE as discussed in the following section.

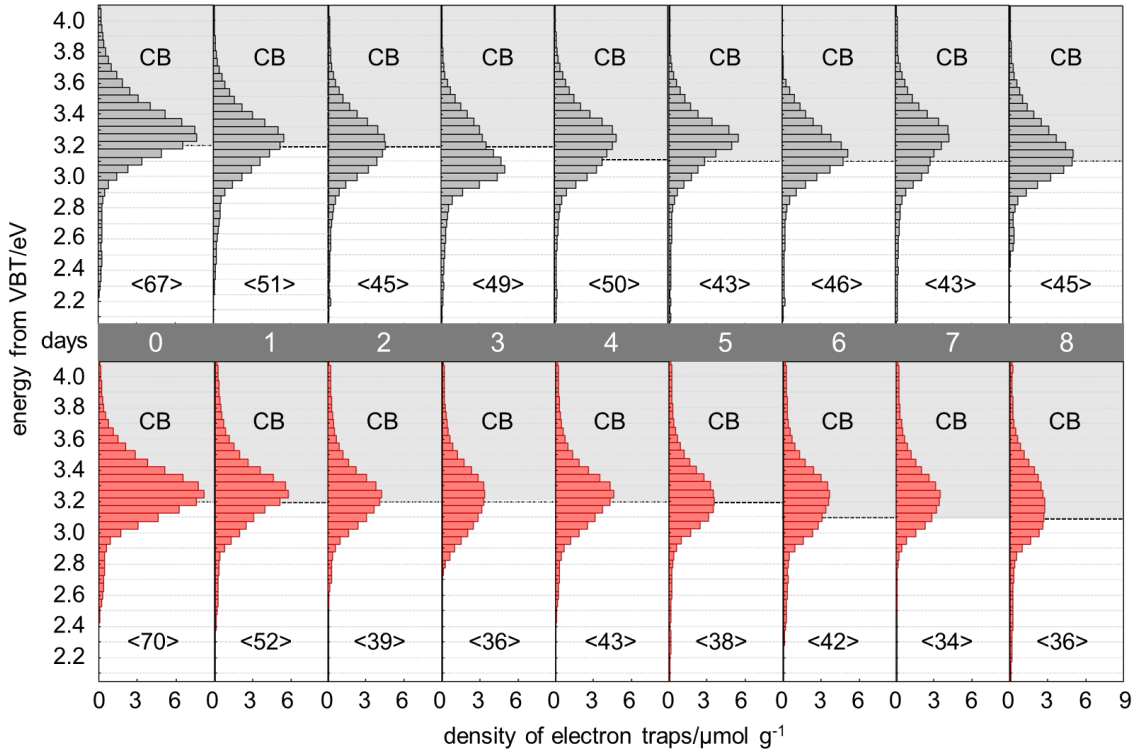

Figure 5-9 ERDT/CBB patterns of (upper) original, brayed and (lower) post-calcined samples. Doted lines indicate conduction band-bottom position and figures in < > denote total density of electron traps.

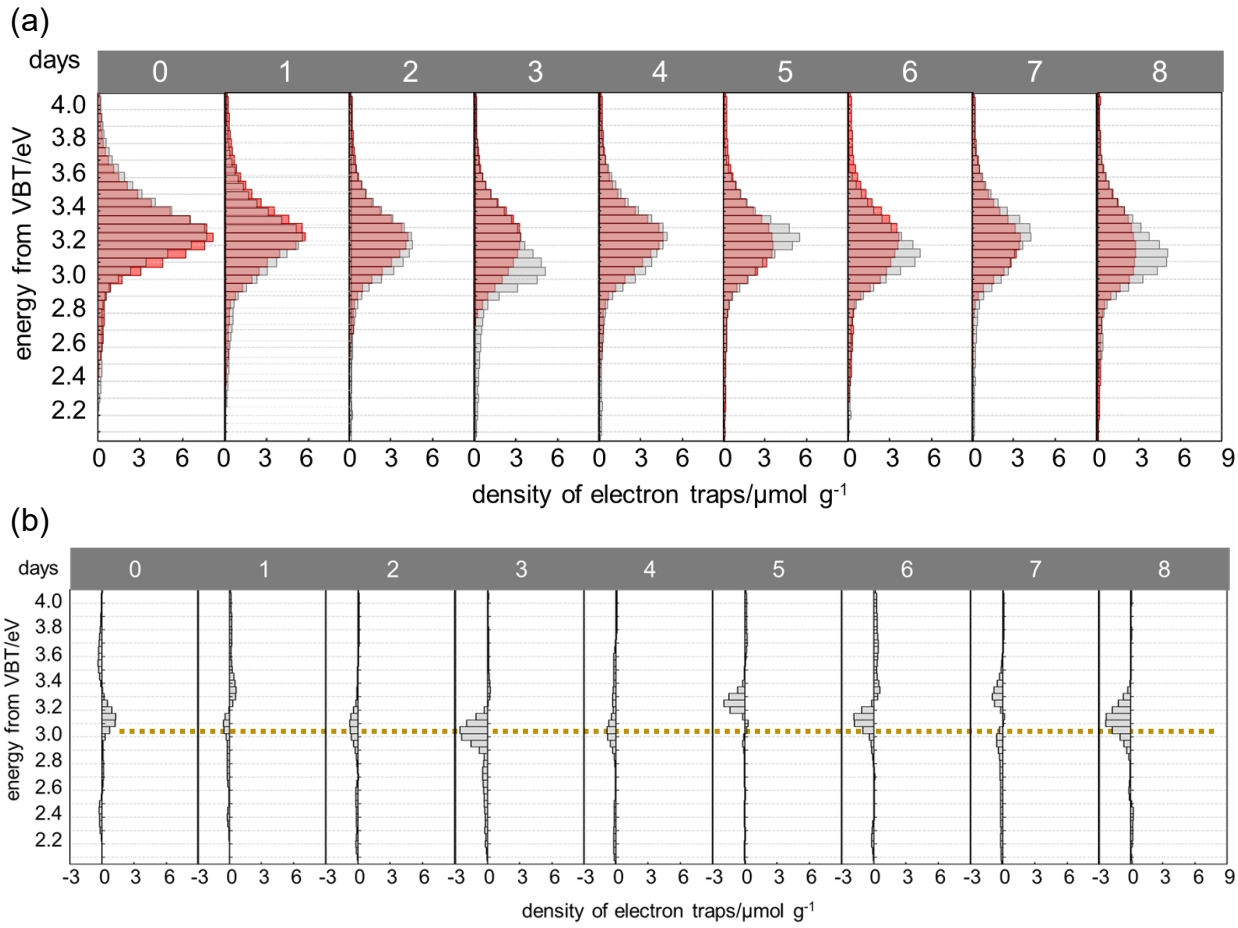

Figure 5-10 (a) Overlapping ERDT patterns of (black) original, brayed and (red) post-calcined samples and (b) subtracted ERDT patterns of post-calcined samples from original and brayed samples. Peaks of electron traps in negative and positive value indicate decrease and increase by post calcination, respectively. Dotted line indicates the position of disappeared peak (ca. 3.05 eV).

5.3.2 *Simulation of ERDT Patterns and Interparticle Charge-Transfer Excitation between Brookite, Anatase and Amorphous Titania*

In this brookite-based samples, it should be considered the ICTE among brookite, anatase and amorphous since those components coexist in the samples. For elucidation of peak positions, ERDT patterns of brookite, ST-21 anatase and commercial amorphous titania (AMO) and their 50/50 weight ratio mixture sample were measured as shown in **Figure 5-11**. In order to reproduce each ERDT pattern of a 50/50 mixture, simulation was performed (SIM), as the same as section 3.3.2 and 4.3.2. From the results, it can be said that h-DOS of brookite may be located similar with anatase (only 0.05 eV lower) and the distribution of h-DOS for brookite is similar to that of anatase, giving highest ζ_S value of 0.89. For the case of mixture with brookite and amorphous titania, h-DOS of amorphous

titania may be located 0.20 eV lower compared with brookite giving higher ζ_S value of 0.65. (The highest ζ_S value was obtained with 0.18-eV downward shift, but the same peak position was obtained when 0.20-eV downward shift was used. Therefore, I used 0.20-eV energy difference for further discussion.)

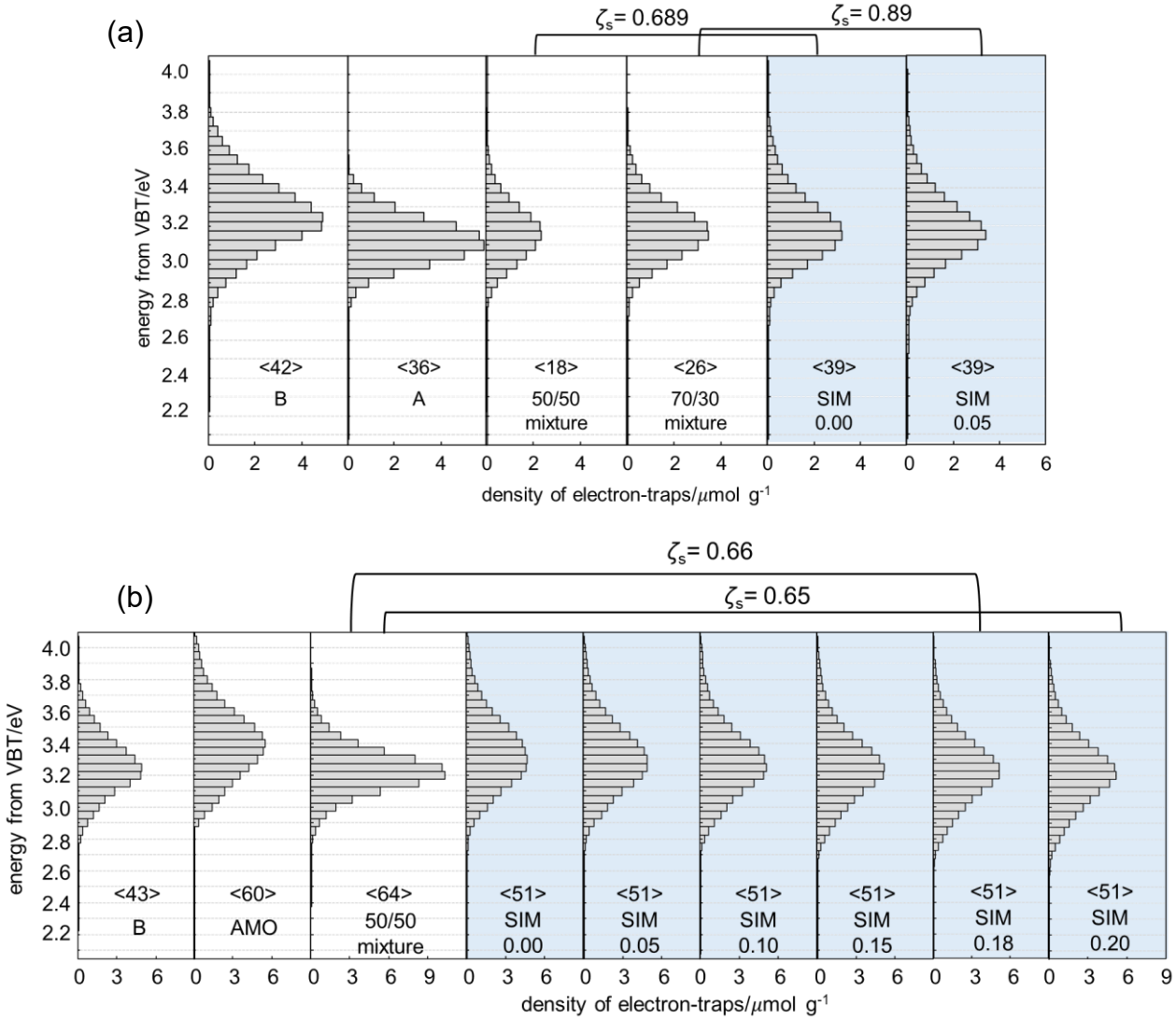

Figure 5-11 ERDT patterns of brookite, anatase (ST-21), amorphous titania and their 50/50 mixtures. Also shown in blue background are representative simulated ERDT patterns by summing up a pattern of (a) 50% anatase with lower-energy shifted pattern of 50% brookite and (b) 50% brookite with lower-energy shifted pattern of 50% amorphous titania.

5.3.3 Deconvolution of ERDT Patterns with Gaussian-curve Fitting

ERDT patterns of brookite and their mixtures with anatase (ST-21) and commercial amorphous titania (AMO) were deconvoluted as shown in **Figure 5-12**. ERDT patterns of brookite was deconvoluted to two peaks, the positions of which are at 3.3 and 3.4 eV. Those peaks were ascribed to brookite (B) and amorphous titania, respectively, by assuming the similar ERDT pattern of commercial amorphous titania was included in them. Interestingly, the peak position of this amorphous suggested that the amorphous component in HPC is not in contact with brookite appearing, but isolated amorphous. In the other words, in HPC, brookite and amorphous exist separately presumably in the form of large secondary particles, that is agglomerates. By mixing with AMO, HPC resulted in appearance of new peak "am-B" at ca. 3.3 eV, slightly lower than amorphous titania included in original brookite. This suggested that the amorphous components included in HPC and commercial amorphous titania are not the same one. On the other hand, mixing HPC with anatase (ST-21) gave further low-energy shifted amorphous peak, amorphous component in contact with anatase and/or brookite (am-A) appeared with a peak assigned to anatase-brookite mixture. One of the possible models is that HPC is composed of large agglomerates of brookite and amorphous and they are not decomposed in an ordinary process. Another peak appeared at 3.2 eV, which is ascribed as mixture of brookite and anatase (B+A), since the peak positions of brookite and anatase and h-DOS position of brookite and anatase are similar, therefore, it is difficult to distinguish them clearly.

Figure 5-13 shows representative deconvolution results of ERDT patterns for original (b0), brayed (bX) and post-calcined (bXc) samples and the results of peaks positions and peak width (FWHM) are summarized in **Table 5-1**. One of the interesting features of ERDT patterns of brookite is that the original HPC samples contained only isolated amorphous, but not am-B, amorphous in contact with brookite. Braying induced the appearance of am-B (The peak position was not the same as the one obtained at control experiments. However, judging from the simulation results that h-DOS position of amorphous commercial titania is located 0.20 eV lower than that of brookite and there was no other candidate, therefore, I ascribed it as am-B). These results suggest both brookite and amorphous in HPC are composed of large secondary particles and almost no chance to be contacted with each other. Roughly speaking, braying induced the formation of am-B by surface amorphization of brookite as well as decomposition of amorphous secondary particles to be in contact with brookite (am-B). Post calcination induced the disappearance of am-B probably re-crystallization.

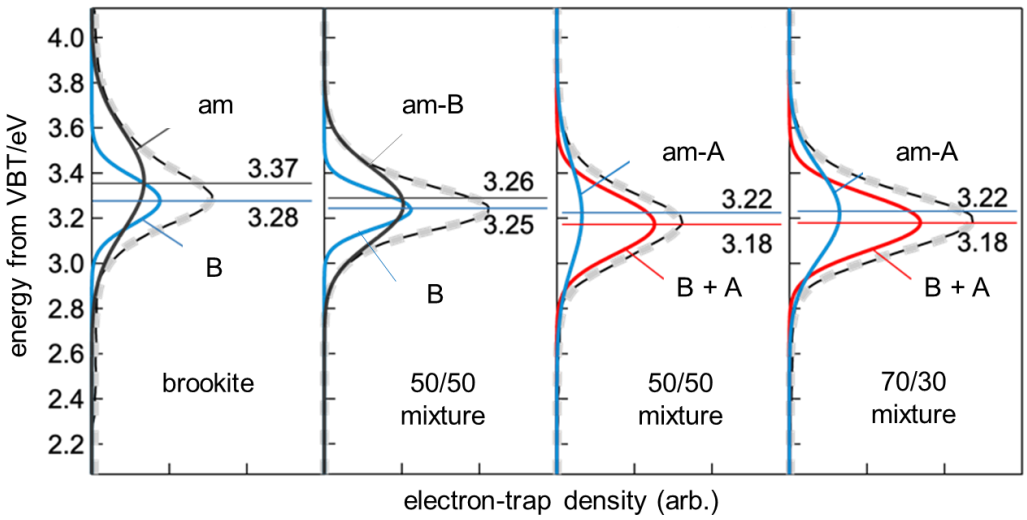

Figure 5-12 Deconvolution of ERDT patterns for (a) brookite, (b) mixture of brookite and amorphous titania in the ratio of 50/50, (c)–(d) mixture of brookite and anatase (ST-21) in the ratio of 50/50 and 70/30 with Gaussian-curve fitting.

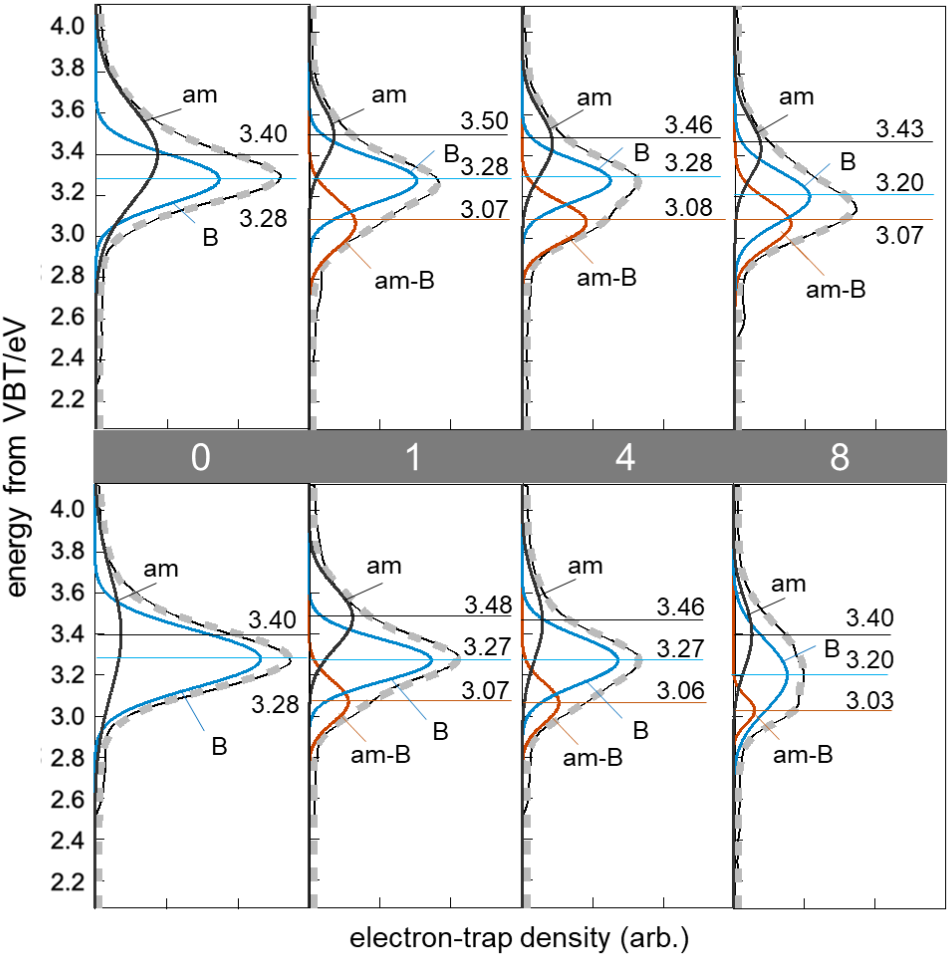

Figure 5-13 Representative deconvolution results of ERDT patterns for (upper) original (b0), brayed (bX) and (lower) post-calcined (bXc) samples.

Table 5-1 Summary of (a) peaks positions and (b) peak width (FWHM) in Gaussian-curve fitting.

(a)

code	peak position/eV		
	am-B	B	am
b0	-	3.28	3.40
b1	3.07	3.28	3.50
b4	3.08	3.28	3.46
b8	3.07	3.20	3.43

code	peak position/eV		
	am-B	B	am
b0c	-	3.28	3.40
b1c	3.07	3.27	3.48
b4c	3.06	3.27	3.46
b8c	3.03	3.20	3.40

(b)

code	FWHM/eV		
	am-B	B	am
b0	-	0.28	0.54
b1	0.28	0.26	0.32
b4	0.23	0.23	0.35
b8	0.26	0.29	0.32

code	FWHM/eV		
	am-B	B	am
b0c	-	0.33	0.68
b1c	0.24	0.24	0.34
b4c	0.23	0.24	0.44
b8c	0.16	0.40	0.40

5.3.4 *Schematic Image of Changes in Surface/Bulk Structures by Braying and Post-Calcination and Relation with Surface Structure and Photocatalytic Activity*

For brookite-base samples, their ERDT/CBB-pattern analyses suggested that the original sample was a mixture of large secondary particles of brookite and amorphous titania. Therefore, braying might decompose those secondary particles gradually forming surface amorphous layers and post calcination induced the partial re-crystallization without giving appreciable grain boundaries.

Such changes in structures were the reason of relatively slow decay of photocatalytic activity by braying in both reaction systems.

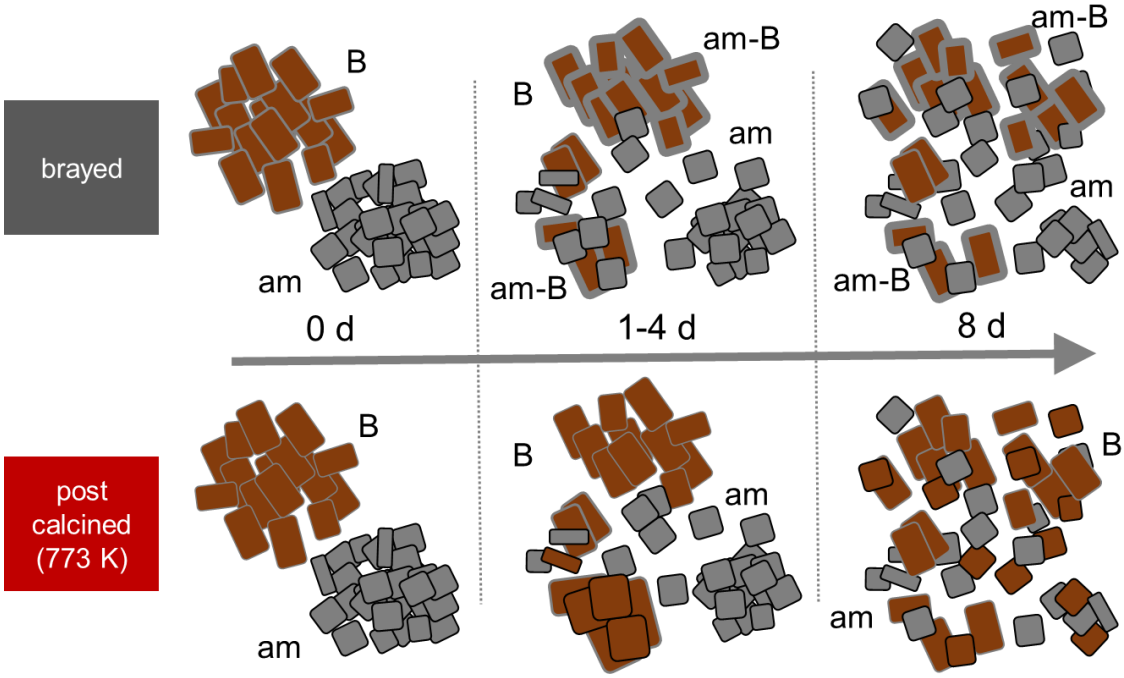

Figure 5-14 Schematic image of changes in surface and bulk structures of brookite sample by braying and post-calcination.

5.4 *Conclusions*

The structure and bulk changes of brookite-based sample by braying and post-calcination were examined by conventional analytical technics and RDB-PAS. Those influences on two photocatalytic activities; hydrogen liberation from deaerated aqueous 50wt% methanol with chloroplatinic acid and carbon-dioxide liberation from aerobic aqueous 5vol% acetic acid, were considered. The original sample was a mixture of large secondary particles of brookite and amorphous titania, and braying might decompose those secondary particles gradually forming surface amorphous layers and post calcination induced the partial re-crystallization without giving appreciable grain boundaries, resulting in relatively slow decay of photocatalytic activity by braying in both reaction systems.

Chapter 6

General Conclusions

6.1 Conclusions

By using ERDT/CBB patterns obtained by RDB-PAS, the changes in bulk/surface structure induced by braying and post calcination, at least three kinds of amorphous components in those samples, am, am-X and am-X(GB) (X: rutile, anatase or brookite) giving a little different influence on the activity of samples, were directly observed and the behavior of amorphization-recrystallization of titania samples could be characterized on the assumption of existence of different kinds of amorphous components. Thus, it can be claimed that ERDT/CBB analysis provided the information of amorphous components in titania samples. In other words, amorphous structure has now become describable. Change of structure of titania particles including amorphous has been clarified for the first time to interpret the change of photocatalytic activity.

6.2 Future Aspects

In the field of material science, we have ignored amorphous phase in the samples. The present results must open up new era of material design and characterization of not limited to titania samples, but also amorphous materials which have not been analyzed precisely. Furthermore, materials which have been recognized not to have amorphous components based on the conventional analytical techniques could be clarified to be amorphous in the near future.

6.3 Original Papers Covering This Thesis

1) Guangyi, C.; Takashima, M.; Ohtani, B., Direct amorphous-structure analysis: How are surface/bulk structure and activity of titania photocatalyst particles changed by milling?, *Chem. Lett.*, **2021**, *50*, 644–648. DOI: 10.1246/cl.200825.

Acknowledgement

This study has been done from October 2017 to March 2021 in Ohtani Laboratory, Division of Environmental Materials Science, Graduate School of Environmental Science, Hokkaido University.

First and foremost, I have to thank my respected supervisor, Professor Bunsho Ohtani in Institute for Catalysis, Hokkaido University. Without his assistance and dedicated involvement throughout my study process, this research would have never been accomplished. I would like to thank you very much for your support and understanding over this past almost four years. You always emphasize how crucial is the originality of research and the skill of communication as an eligible researcher. I will keep in my mind your words and let them guide me in future research work.

I would also like to show gratitude to two peer reviewers, Prof. Yuichi Kamiya and Associated Prof. Masaru Kato from the Graduate School of Environmental Science, Hokkaido University. I accepted a lot of inspired questions from them, which made me considered my research more deeply. Both of sensei spent much time helping me to improve my thesis.

Meanwhile, I would like to express my sincere gratitude to Associated Prof. Ewa Kowalska. She always encouraged me and showed me a positive way when I felt frustrated and self-doubt.

I also would like to express my gratitude to Assistant Prof. Mai Takashima for giving me so many bits of advice and guidance in my study. She patiently guides me and explains the points where I cannot understand.

I would like to thank the staffs of Miki Sasaki san and Murayama Kyoko san who help me familiar with the measurement procedure of RDB-PAS.

This research has been financially supported by a Chinese government scholarship from 2017. I express my sincere gratitude for my motherland and the Communist Party of China here.

I express my gratitude also to all the seniors, peers, and juniors in the Ohtani lab. We have shared so many wonderful and memorable recollections together where we spent the time hiking, traveling, and even enjoying nice food together. Those sweet and unforgettable memories are so precious that they will be occupied one corner of my heart forever.

Finally, I appreciate my parents' supporting and accompany. Whenever I felt sad or frustrated they comforted and told me to keep calm down and moving on with a grateful mind. I felt I could be healed by their words then I gradually realized that I was so deeply relying on them and missing family bonding time.